



# Standard Phantoms for EM Device testing

Soroush Abedi

## ► To cite this version:

Soroush Abedi. Standard Phantoms for EM Device testing. Electromagnetism. Sorbonne Université, 2022. English. NNT : 2022SORUS004 . tel-03885472

**HAL Id: tel-03885472**

**<https://theses.hal.science/tel-03885472>**

Submitted on 5 Dec 2022

**HAL** is a multi-disciplinary open access archive for the deposit and dissemination of scientific research documents, whether they are published or not. The documents may come from teaching and research institutions in France or abroad, or from public or private research centers.

L'archive ouverte pluridisciplinaire **HAL**, est destinée au dépôt et à la diffusion de documents scientifiques de niveau recherche, publiés ou non, émanant des établissements d'enseignement et de recherche français ou étrangers, des laboratoires publics ou privés.

École doctorale n° 391 : Sciences mécaniques, acoustique, électronique et  
robotique de Paris

# Rapport de Thèse

pour obtenir le grade de docteur délivré par

**Sorbonne Université**

**Spécialité doctorale ‘Électronique’**

*présentée et soutenue publiquement par*

**Soroush ABEDI**

*le 14 Janvier 2022*

## **STANDARD PHANTOMS FOR EM DEVICE TESTING**

Directeur de thèse : Hélène Roussel

Co-encadrante de thèse : Nadine Joachimowicz

### Jury

Mme Eirini Karanasiou	Professeur, Hellenic Military Academy	Rapporteur
Mme Claire Migliaccio	Professeur, Université Côte d'Azur	Rapporteur
M. Stéphane Holé	Professeur, Sorbonne Université	Examineur
M. Patrick Plaisance	Professeur, Université de Paris	Examineur
Mme Nadine Joachimowicz	Maître de Conférences, Université de Paris	superviseur
Mme Hélène Roussel	Professeur, Sorbonne Université	superviseur

Laboratoire Génie électrique et électronique de Paris (GeePs)  
UMR CNRS 8507



# TABLE OF CONTENTS

<b>1</b>	<b>INTRODUCTION .....</b>	<b>1</b>
1.1	<i>Medical imaging.....</i>	<i>1</i>
1.2	<i>Electromagnetic imaging for a novel generation of medical devices-EMERALD.....</i>	<i>5</i>
1.3	<i>Aim of the thesis.....</i>	<i>9</i>
1.4	<i>Thesis structure .....</i>	<i>11</i>
<b>2</b>	<b>Anthropomorphic phantom.....</b>	<b>14</b>
2.1	<i>Introduction.....</i>	<i>14</i>
2.1.1	Phantoms for MWI in the literature .....	15
2.1.2	Motivation of using 3D printed liquid phantoms .....	17
2.2	<i>Tissue Mimicking Materials' (TMMs) fabrication.....</i>	<i>19</i>
2.2.1	Relaxation models .....	19
2.2.2	Mixture production protocols .....	22
2.2.3	Dielectric characterization with an open-ended coaxial system .....	24
2.2.4	Selection of a fluid mixture law .....	27
2.2.5	Optimization code .....	32
2.2.6	Experimental validation .....	35
2.2.6.1	Production and characterization of the 10 mixtures .....	35
2.2.6.2	Reproducibility of the results–NUIG/CNRS .....	36
2.2.6.3	Flowchart to produce the mixture .....	37
2.3	<i>Development of anthropomorphic printable cavities.....</i>	<i>38</i>
2.3.1	3D printing for medical application .....	38
2.3.2	Modeling and printing 3D cavities.....	39
2.3.2.1	STL format files.....	40
2.3.2.2	Segmentation with 3D Slicer .....	41
2.3.2.3	Design and realization with Blender .....	43
2.3.2.4	Application to the realization of a brain cavity .....	45
2.4	<i>GeePs anthropomorphic phantoms.....</i>	<i>46</i>
2.4.1	Head phantoms designed for POLITO system .....	46
2.4.1.1	POLITO system .....	47
2.4.1.2	Head cavities .....	47
2.4.1.3	TMM recipes and dielectric properties for head phantom.....	49
2.4.1.4	Alternative material for 3D printing cavities.....	50
2.4.2	Axillary Phantom designed for FCUL microwave imaging system .....	52
2.4.2.1	FCUL system .....	53
2.4.2.2	Thorax cavities .....	54
2.4.2.3	TMM recipes for axillary phantom.....	55
2.4.3	Liver Phantom designed for CNR-IREA system .....	56
2.4.3.1	CNR-IREA system.....	57
2.4.3.2	Liver cavities.....	57
2.4.3.3	TMM recipes and dielectric properties for liver phantom.....	59
2.5	<i>Conclusion .....</i>	<i>60</i>

<b>3</b>	<b>E-Field simulation of 3D anthropomorphic phantoms .....</b>	<b>62</b>
3.1	<i>Introduction.....</i>	62
3.1.1	The Finite Integration Technique (FIT) and Method of Moment (MOM) .....	62
3.1.2	Accuracy of FIT and MOM .....	64
3.1.3	Rectangular plate.....	64
3.2	<i>Importing STL files into an EM solver .....</i>	67
3.3	<i>Numerical simulations on head phantoms.....</i>	68
3.3.1	Effect of coupling medium.....	70
3.3.2	Effect of Phantom Complexity .....	71
3.3.2.1	Number of cavities .....	72
3.3.2.2	Vessels around a randomly shaped stroke .....	73
3.3.3	Effect of the Plastic .....	74
3.4	<i>Simplification of head phantom .....</i>	75
3.4.1	Validation of simplified phantom .....	77
3.4.2	Validation of simulations .....	78
3.4.2.1	Qualitative comparisons .....	79
3.4.2.2	Quantitative comparisons: Root Mean Square Error (RMSE) calculation.....	83
3.5	<i>Numerical simulations on axillary phantom.....</i>	85
3.5.1	Detection of different types of nodes.....	86
3.5.2	Effect of the plastic .....	87
3.6	<i>Conclusion .....</i>	88
<b>4</b>	<b>A priori information in inverse algorithms.....</b>	<b>91</b>
4.1	<i>Introduction.....</i>	91
4.2	<i>The microwave imaging problem.....</i>	92
4.3	<i>Introduction of the contour as a priori information in TSVD method.....</i>	94
4.3.1	TSVD method and Born approximation .....	94
4.3.2	Numerical analysis on a 2D case .....	97
4.3.2.1	Cross-validation of the electromagnetic field computation .....	97
4.3.2.2	Toward a suitable configuration .....	98
4.3.3	Numerical analysis on a 3D anthropomorphic breast phantom.....	103
4.4	<i>Conclusion .....</i>	113
<b>5</b>	<b>Conclusion and future work .....</b>	<b>114</b>
	<b>List of Publications .....</b>	<b>119</b>
	<b>REFERENCES.....</b>	<b>121</b>

# 1 INTRODUCTION

This dissertation presents research on the development of standardized phantoms that will provide unified benchmarks that allow comparing the results achieved by EM imaging on biological tissues at microwave frequencies for diagnostic biomedical imaging. Microwave imaging (MWI) is a non-invasive diagnostic asset for the detection of abnormal tissues in the human body [Henriksson *et al.*, 2010; Scapaticci *et al.*, 2012; Smith *et al.*, 2021]. This thesis focuses on the design and realization of standardized phantoms for testing EM devices at microwave frequencies. This is essential to evaluate electromagnetic systems under controlled and repeatable conditions.

## 1.1 Medical imaging

Since nowadays MRI and X-ray technologies are the most common and trusted ones by the medical community, in the following a brief review of MRI and CT scan is presented.

The first ever X-ray was taken by Nobel Prize winner – Wilhelm Roentgen in 1895 [Pamboukian, 2001]. They are single images in black and white and all grey in between, which provides a snapshot of the inside of body. This is achieved by passing electromagnetic radiation through the region of interest. An X-ray detector captures the shadow of the object within our body after the wave is illuminated to it. In 1970, almost 75 years later, Godfrey Hounsfield and Allan MacLeod Cormack introduced us to Computed Tomography (CT) Scans [Tan and Poole, 2020]. CTs are imaging the inside of body from multiple cross-sectional angles with fixed distances. The smaller the distance between each image, the more images can be captured. These images are called slices, and since the number of images is much more across so many levels of the body, they contain much more information than Single X-Rays. As can be expected from the name of

modality, these are processed on a computer and can be transferred to films later. These computer-based images are called DICOM images for Digital Imaging and Communications in Medicine.

The absorbance rate of biological tissues at a specific range of frequency differs from one to the other due to the density and water. Calcium in bones absorbs x-rays the most, so that bones appear more contrasted in white. X rays pass through soft tissues easily, hence are seen in shades of grey. Air does not absorb any rays, so it appears black. Although a ‘Contrast Agent’ can be injected into the patient’s bloodstream [Mazloumi *et al.*, 2021] which flows through the blood vessels and allows for absorption of the X-rays. The use of contrast agents is essential in medical imaging to opacify lesions and tissues.

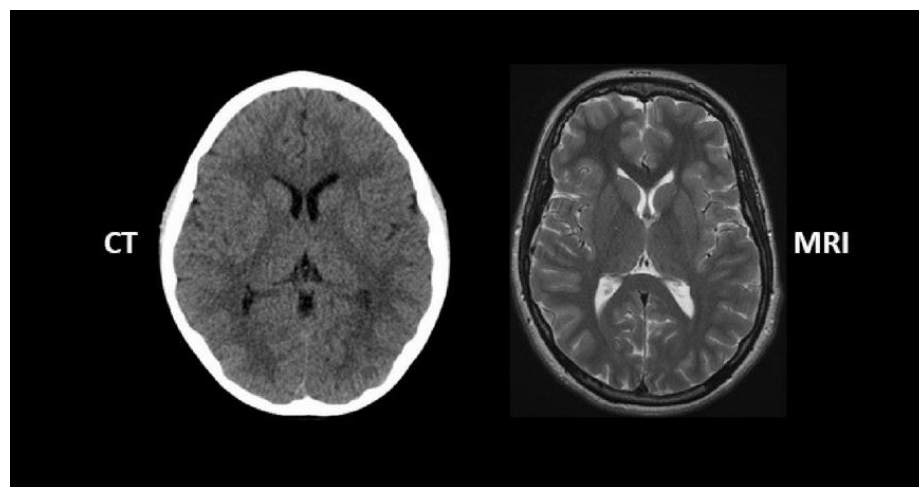


Figure 1.1: MRI and CT scan of the brain [CT scan vs MRI, online].

It is noteworthy that based on the time when the image is captured, the contrast flow will allow for highlights of different regions. This is called a 4D CT, where the fourth Dimension is Time, which helps immensely to capture dynamic moving organs like the heart and understand its functioning. This method is also limited in helping to understand the soft tissues in more details as well. CT scan offer in detail images of bones and blood vessels for diagnosing and health tracking of patients.

Unlike CT, MRI or magnetic resonance imaging does not require radiation. MRI utilizes a combination of a magnetic field, radiofrequencies and a computer system to take high-resolution pictures. When it comes to visualization of joints, soft tissues and bones, MRI is proved to be a high efficient technique of reconstruction of the image of the tissue. The initial studies of MRI development can be traced to 1938 where Isidor Isaac Rabi passed a beam of molecules through a magnetic field, which emitted radio waves at specific frequencies [*Rigden et al.*, 1999]. The first full body scanner was invented in the 1970s by John Mallard and team [*Tabakov*, 2021]. The patient must lie on a platform inside a tube shaped machine where magnetic field is created around the patient. Then radio waves in the form of pulses are directed onto the region of interest, the atoms in that region of the body get excited and generate signals. These signals are detected by a computer and translated into image with high resolution. The tissues having high water content e.g., fat and muscle give out high intensity signals and appear bright. Bone tissue having low water content give out weaker signals and appear dark. Therefore, the gradation of contrast of tissues observed in MR scan is exactly the opposite of that observed in CT.

Both CT and MRI have their own drawbacks. For instance, CT can harm unborn babies, cause radiation exposure and it has limited sensitivity when it comes to detect size and location of early ischemia. On the other hand, possible reactions to metals due to magnets, loud noise that can cause hearing problem, potentially longer acquisition time are some downsides of MRI technique [*Kidwell and Hsia*, 2006]. Since these two techniques are frequently used over years, there are millions of images from different parts of human body in different conditions available. We are going to use MRI and CT scan images to design head and axillary phantoms for testing MWI systems.



To do so we need software that can read these images and gives us the chance to segment the image and extract the part we want. In the end, the software has to be able to make 3D model out of the extracted organ [Abedi *et al.*, 2021; Joachimowicz *et al.*, 2018]. This is covered in chapter two with an introduction of open source and free software. While our phantoms are designed based on MRI and CT scans of the human body, they will be used to test MWI systems.

Microwave imaging technique is based on illumination of electromagnetic wave to a test object, as it is done in X-ray modality. This method is used in the microwave range of frequency (300 MHz to 300 GHz). In traditional radiology, the sensor is a film as explained earlier in this section, while in Microwave imaging there is a set of antennas as transmitter and receiver all around objects under test. The position, size, shape, or dielectric properties of the target can be exploited by microwave imaging. These information open up new avenues for applications range from breast imaging [Henriksson *et al.*, 2010; Li *et al.*, 2001], brain imaging [Rodriguez-Duarte *et al.*, 2021; Ljungqvist *et al.*, 2017; Semenov *et al.*, 2008], liver ablation imaging [Wang *et al.*, 2021] and lymph node imaging [Savazzi *et al.*, 2020] to other fields like civil engineering [Mikhnev and Vainikainen, 2002] and food industry [Vasquez *et al.*, 2020; Zidane *et al.*, 2020].

One of the first researches on feasibility of microwave imaging goes back to 1970s to obtain an image of canine kidney [Larsen and Jacobi, 1979]. From then until now several systems have been designed and implemented [Rodriguez-Duarte *et al.*, 2021; Karadima *et al.*, 2020; Candefford *et al.*, 2017; Personn *et al.*, 2014; Meaney *et al.*, 2000; Joisel *et al.*, 1999; Semenov *et al.*, 1996]. Even though there are several clinical trials have been conducted, still microwave imaging has not been used widely by clinical practitioners. This can be because of either limited penetration depth of wave in biological tissues at microwave frequency range and low resolution of images compared

with other modalities. Moreover, the inverse scattering problem faces non-linearity and ill posedness of Maxwell's equation [Noghanian *et al.*, 2014, chapter two].

Microwave imaging can retrieve either the shape and size (qualitative imaging) or the dielectric properties and spatial distribution (quantitative imaging) of the object to be imaged (target). In qualitative imaging, reconstruction gives information on the shape, size and location of the target. This technique cannot offer any information about the dielectric properties. On the other hand, the efficiency in computation and fast reconstruction of qualitative imaging makes it a decent technique to track the size and location of abnormal tissue for instance the tumor in brain or breast. Quantitative MWI reconstructs maps of dielectric properties of the area of interest. Since there can be a big difference between dielectric properties of different tissues in body, this technique has high potential to be the next generation of cancer and tumor detection and health monitoring systems in near future [Tobon Vasquez *et al.*, 2020; Henriksson *et al.*, 2010; Meaney *et al.*, 2007]. However, quantitative imaging is in need of proper computation power and in many cases, they are dependent of a priori information [Pastorino, 2010].

## **1.2 Electromagnetic imaging for a novel generation of medical devices-EMERALD**

EMERALD is the coherent action of leading European engineering groups involved in electromagnetic (EM) technology for medical imaging to form a cohort of highly skilled researchers capable of accelerating the translation of this technology “from research bench to patient bedside”.

Nowadays, medical imaging technologies play a key role to face the ever-growing number of challenges due to aging populations, as they are the essential clinical tool to deliver accurate initial diagnoses and monitor the evolution of disease over time. For this reason, a whole range of new imaging modalities is currently being developed to supplement and support current modalities. As

mentioned in the previous section, among these technologies, there is microwave imaging, which involves the illumination of a portion of the body under investigation with low-power non-ionizing EM waves (in the microwave spectrum) and the use of the resultant backscattered signals to generate images of the internal structures of the body.



Figure 1.2: EMERALD's 13 early stage researchers (ESRs).

The scientific objective pursued by the EMERALD action is to accelerate the translation of research in EM medical imaging into clinical prototypes. To this end, EMERALD will establish a group of 13 outstanding early stage researchers who will be the European leaders in this field, through a unique scientific and training program. The EMERALD trained researchers will drive the future developments of EM imaging technology, thanks to the targeted skills, they will attain, and their established connections with clinicians and stakeholders.

The EMERALD consortium involves academic institutions, industrial partners, hospitals and university medical centers (as partner organizations). The success of EMERALD will ensure that all achieved innovative technological developments are translated into benefits to the end-user community with an impact on both the European society and scientific community.

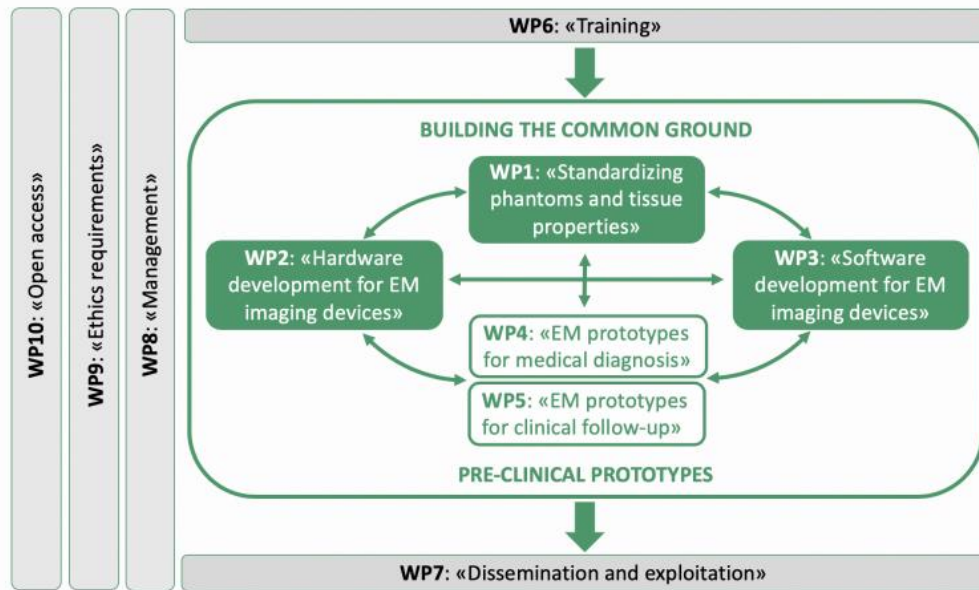


Figure 1.3: Work Plan (WP) scheme of the EMERALD project.

There are four main objective to the EMERALD project:

- To accelerate translation of research of EM medical imaging into clinical prototypes by advancing the technology, addressing possible standardizing procedures and developing prototypes for novel applications.
- To set-up and support the first complete scientific and training program in EM medical imaging at a European Level (and where possible worldwide).
- To provide the Early Stage Researchers (ESRs) with excellent, multi-disciplinary scientific training and a set of competitive, transferable skills.
- To expose the ESRs to academic and non-academic sectors, improving their future career perspectives.

In particular, the project is organized in 10 working plans. Five work plans are designed for 13 ESRs to be involved and their dissertations are defined based on them. Each work plan includes a few number of ESRs and between these work plans, there are mutual collaborations as you can see in figure 1.3.

My contribution to the EMERALD project as the ESR1 is to develop standardized phantoms that will provide unified benchmarks and allow comparing the results achieved by EM imaging with different modalities (WP1). The phantoms are used to assess the devices in which will be developed by other ESRs. They are realized with 3D printed technology and adapted to the geometry of the devices that other ESRs are working on. In order to get closer to a real medical imaging case, the 3D printed phantoms is filled with liquid mixtures that mimic different tissues at microwaves [Abedi *et al.*, 2021; Joachimowicz *et al.*, 2018]. Particular attention is devoted to head and axillary region tissues.

During my PhD based on the collaboration plan defined within the project, each ESR had to go to travel to other institutions to gain knowledge and apply new knowledge it to their own project. This is called attending secondment. A secondment is a temporary work placement of an employee in another place to that in which they normally work – they can be either internal or external. They are internal when the work is within another area of the same organization, and they are external when the employee transfers to another organization for the temporary change in roles. I have attended to three external secondments during my PhD program.

As a visiting researcher for secondments, I had the opportunity to work in different laboratories in Ireland, Serbia, Italy and France and was supervised by several pioneers on the subject from whom I gained a lot of experience. During my short-term secondments in these laboratories, I successfully found a common language with my colleagues despite our different backgrounds in research, language and culture. I was also able to publish our results in well-known journals. In Ireland, I worked with the team at "Translational Medical Device Lab" for two months (Jun-July 2019) and I learned how to characterize the dielectric properties of biological tissues with conducting several measurements. In Serbia, I worked at WIPL-D, a private company dedicated

to the development of commercial EM simulation software. In three months, I learned how to use a new software and export simulated data for tumor detection. Finally, during the last secondment I worked with microwave imaging team at CNR-IREA, introducing STL files of phantoms as a priori information into their inverse algorithms. Here we used data from simulation in our algorithms.

As a part of my institution contribution to the EMERALD project, we also hosted four ESRs from WP1, WP4 and WP5. During their stay at GeePs in Paris, they were introduced to the protocols of producing mixtures, which mimic dielectric properties of biological tissues. They also used our set-up of characterization (homemade probe coupled to a portable VNA) for measuring the dielectric properties of produced mixtures. As a part of their secondments, we also worked on segmentation of tissues from MRI and CT scan and we trained them on making their own 3D model of phantom and exporting it as STL files.

Working as a part of such a big project and having the chance of working in several laboratories and meeting different scientists and mentors helped me to gain many skills. These skills give me the confidence to be involved in projects that are multidisciplinary, in which I believe I can be successfully productive. I am aware of the impact of these multi-layered projects on people's lives and this makes me motivated about them even more.

### **1.3 Aim of the thesis**

The encompassing objective of this thesis is to provide standard anthropomorphic phantoms which are reproducible by an electrical engineer in a non-specific environment (no hood), and without drastic precautions. These phantoms are going to be used for testing MWI systems developed by other ESRs in EMERALD project.

Developing techniques to prepare numerical version of phantoms from MRI and CT scan is the first and most crucial step toward obtaining standard phantoms for MWI systems. These numerical phantoms can be used for 3D printing, simulations and inverse algorithms. The goal is to use open source and free software while preparing numerical version of phantoms to be sure that designers in different laboratories in different countries can follow the same procedure. These numerical files need to be prepared in such a way that will be readable for 3D printers. 3D printed standard phantoms are designed to be used in different experiments for testing several designed MWI systems. The 3D printed phantoms are cavities filled with mixtures with the same dielectric properties of the representing. This means that experimental protocols and measurements techniques have to be precisely developed. This ensures us that the phantom is going to have the same behavior while being illuminated by EM wave at microwave frequencies as biological tissues.

Before any experiment, electromagnetic simulators should be used for investigating the presence of standard phantoms in MWI systems. To be able to predict the results of the experiments, the numerical versions of phantoms and MWI systems has to be imported into different EM solvers for cross validation. The goal is to provide a systematic process, which helps researchers have pre-results before any experiments.

As mentioned in section 1.1, to improve the performance of inverse algorithms and reduce the reconstruction time having a priori information is essential. That is why in this thesis we are aiming for helping inverse algorithms by using numerical version of phantoms. This means by introducing the boundaries of the area of interest the algorithm can achieve its purpose in a more efficient and faster way. The goals of this work are summarized as:

- Design and production of 3-D printed breast and head phantoms adapted to the geometry of the devices in WP4-WP5, and their applications (cerebrovascular diseases, hyperthermia and tumor detection).
- Production and dielectric characterization of mixtures that mimic different breast and head tissues (fat, fibro-glandular, brain, cerebral spinal fluid (CSF), blood, bone, skin, lymph,...) in the microwave frequency range.
- Computation of the electromagnetic field inside the phantom with and without tumor or infarcted tissue mimicking anomaly.
- Influence of the coupling media, structure material, working frequency, source, and type of anomaly and composition of the target organ.
- Use of the numerical version of phantoms to include a priori information in microwave imaging algorithms.

## **1.4 Thesis structure**

This thesis is organized in five chapters, including the present chapter, which is a brief introduction of three different modalities of EM imaging. Moreover, in this chapter the objectives of EMERALD have explained and in the frame of this European funded project the goals of this thesis have been drawn.

The main contribution of this doctoral research is shared in chapter two to four. Each chapter elaborates one of the usages of numerical phantom files.

Chapter 2 covers instructions on production of 3D printed liquid anthropomorphic phantoms. To be able to produce tissue mimicking materials explanation on relaxation models, dielectric characterization techniques, fluid mixture laws and some practical protocols are provided. Moreover, general tools for creating numerical phantoms of the human body from MRI and CT



scan of the organ are introduced. These tools help the designer to segment the target organ and then modify it. In this chapter there are several phantoms designed, 3D printed and introduced adapted to MWI systems developed in EMERALD project.

Chapter 3 addresses the E-Field simulation on 3D anthropomorphic phantoms. This is a study on effect of different parameters of the phantom on electric field distribution inside of it and detection of the abnormal tissue inside. Simulations are done using numerical version of introduced phantoms in the previous chapter to prove the possibility of recognition of abnormal tissues in different environments.

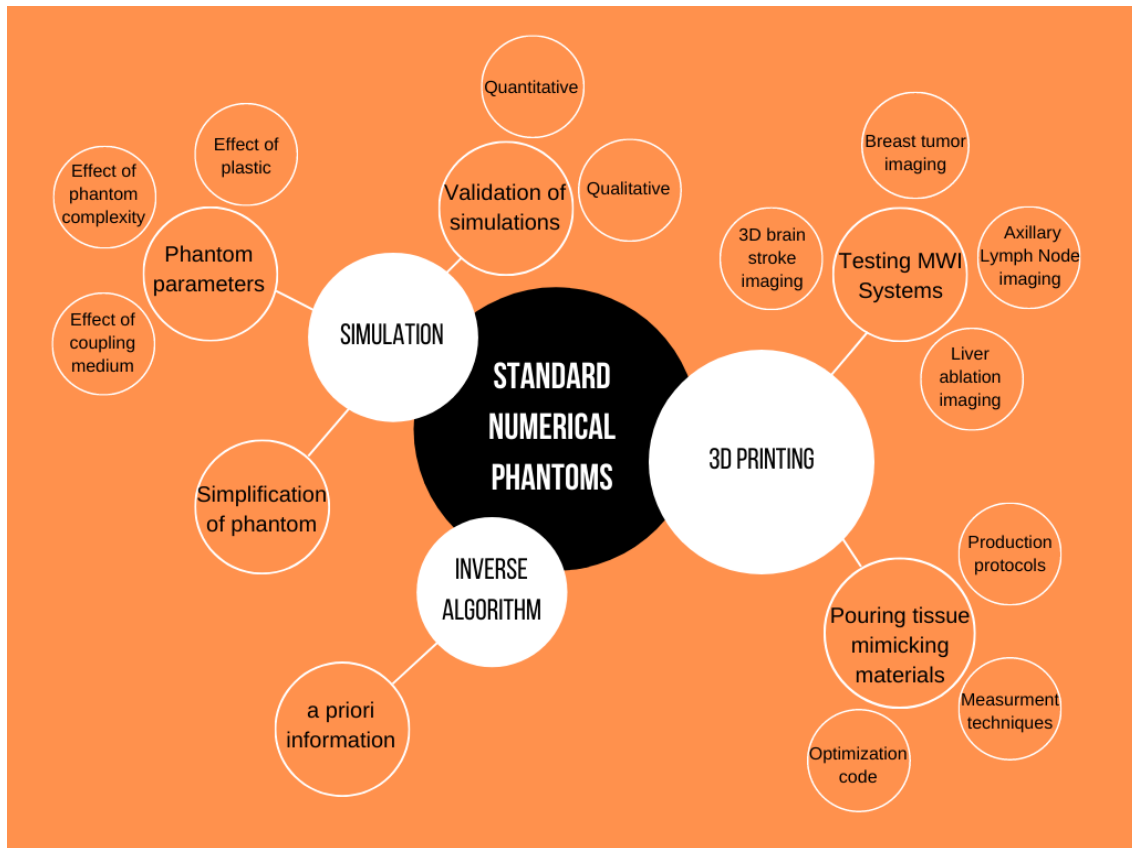


Figure 1.4: Three main chapters of the thesis are covering the usage of standard numerical Phantoms in details.

Chapter 4 focuses on the usage of numerical version of breast phantom as a priori information to help the inverse algorithm. The objective is to find the location and shape of the tumor inside

the breast. In this chapter, we will try to find a way to introduce a priori information to the inverse algorithm to improve the spatial resolution of the images and detect anomalies.

In the last chapter, a flow chart concludes all results presented in this thesis and with some suggestions for future work, the thesis is closed.

## 2 Anthropomorphic phantom

### 2.1 Introduction

In recent work by our group, it has been shown that mixtures based on TritonX-100 and salt water can dielectrically mimic the different tissues of the breast and head in a wide range of frequencies and are easily fabricated [Joachimowicz *et al.*, 2018]. These stable mixtures are contained in cavities representing the specific organ. The fabrication of an anthropomorphic phantom therefore consists of designing and 3D printing cavities, with tissue mimicking materials poured inside.

In this work, the feasibility of this process is tested and extended to the production of phantoms adapted to the microwave imaging systems developed in EMERALD project at Politecnico di Torino (POLITO), Faculdade de Ciências da Universidade de Lisboa (FCUL) and CNR-IREA.

After a review of the phantoms developed in the literature for microwave imaging, and the motivations for developing anthropomorphic cavities filled with liquid mixtures in the context of the EMERALD project, section (2.2) is devoted to the method used to determine the tissue mimicking materials in the frequency range of [0.5 - 6] GHz. In particular, we will see how this issue can be reduced to an optimization problem of two unknowns, corresponding to the concentrations of the mixture components. Section (2.3) deals with the fabrication of 3D printed anthropomorphic cavities. From an MRI scan, an STL file is created in two steps: a segmentation process using the 3D-Slicer software and a design process using the Blender CAD software. The last section (2.4) is devoted to the realization of three phantoms adapted to the electromagnetic devices developed by our EMERALD partners that represent the head [Rodriguez-Duarte *et al.*, 2021], the thorax [Savazzi *et al.*, 2020] and the liver with ablation [Wang *et al.*, 2021].



Figure 2.1: Filling the cavity, which represents human breast with mixture mimicking breast tissues.

### 2.1.1 Phantoms for MWI in the literature

Developments of microwave imaging systems not only rely on computer simulations but also preclinical experiments on human body. Due to several reasons, it is not possible to employ the human body for testing MWI devices that have electromagnetic interaction with human body. Beside safety reasons, respiratory movement, cardiovascular vibration, and variable skin humidity can be mentioned as obstacles of using human tissues in imaging systems. In many laboratories there are objects used as alternatives of human body, which are neither physically nor dielectrically close to human tissues. However, since a phantom is designed to be exposed to the electromagnetic waves, its shape plays an important role to have relatively accurate reflections and penetrations based on the realistic anatomy of the organ. Emulating a human organ or tissue with an exact substitute requires an accurate artificial phantom that is expected to have three features: 1) realistic anatomy 2) dielectric precision across the band of interest, and 3) a long lifetime [Mobashsher, 2015]. The dielectric properties of the phantom have to mimic the dielectric properties of real tissues in the frequency range of interest. The lifetime of the phantom is important due to the need

of conducting several experiments in the same conditions. It means that for instance for liquid phantoms, the phantom should be stable and has homogenous mixtures inside over a long period.

Phantoms are classified into various types from different perspectives. Depending on the electrical properties, they can be low- and high- water-content materials [McDermott *et al.*, 2017; Abedi *et al.*, 2019]. Here we classified the phantoms based on their physical appearance. The head is one of the most complicated structures of the human body. Due to the sophisticated fabrication techniques, there are limited numbers of solid human head phantoms developed. In Figure 2.2, two examples of solid head phantoms are presented.

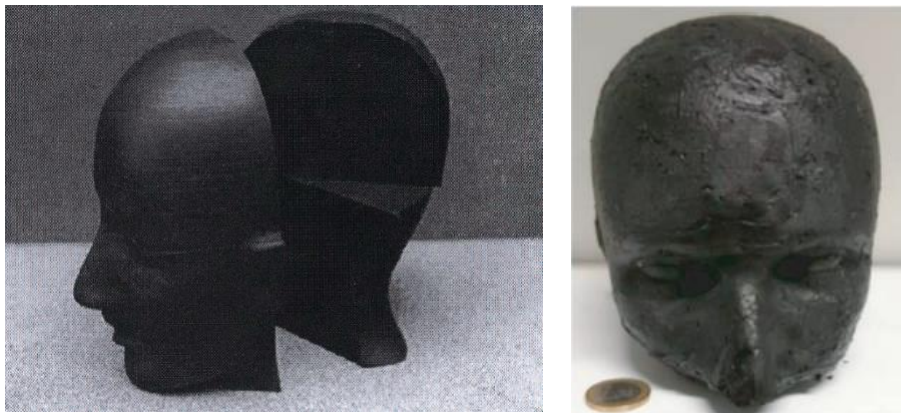


Figure 2.2: (a) The solid human-head phantom reported in [Kobayashi *et al.*, 1993], (b) Human head phantom based on graphite, carbon black, polyurethane, and acetone or isopropanol [McDermott *et al.*, 2017].

Gel head phantoms are made of polymer- or agar-based substances. For broadband application one can take semi-solid head phantoms as a good candidate. These phantoms are made of several homogenous materials to fabricate layered or heterogeneous semi-solid phantoms [Mohammed *et al.*, 2013; Mobashsher *et al.*, 2014]. These phantoms are generally agar-based to have a realistic shape of the head.

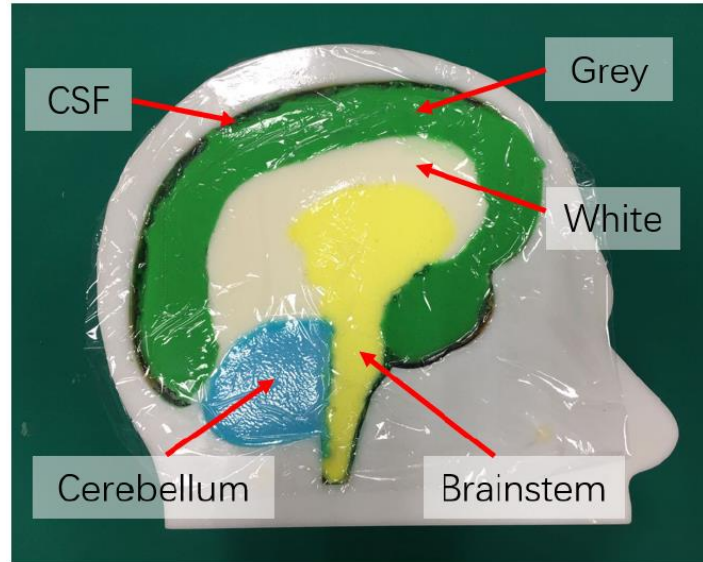


Figure 2.3: A completed left-half semi-solid head phantom. [Gong *et al.*, 2021]

Researchers are interested in liquid phantoms since the production process is easy and the phantom properties can be changed by adding or removing components. Beside sugar-water-salt-based solutions, mixture of propylene glycol and deionized water has been used for homogeneous liquid phantoms [Rodrigues *et al.*, 2014]. The techniques to produce biological tissue-mimicking liquids suggested in the literature are generally not easy to set up and often require specific equipment.

### 2.1.2 Motivation of using 3D printed liquid phantoms

As mentioned in the previous section, microwave imaging is working based on the interaction between electromagnetic waves and the target object, so the phantom must necessarily mimic both the physical form and dielectric properties of the target organ in the human body. Moreover, these phantoms are going to be developed in the framework of the European EMERALD project and need to be easy to produce, stable in time, accurate enough for doing experiments in a wide frequency band and remotely producible in different labs.

Among the three described types of phantoms (solid, semi-solid, liquid), liquid phantoms are the easier to produce and adjustable, and stable in time. Furthermore, the use of 3D printing technology and Segmentation/CAD software to design the phantom from MRI and CT scans allows for an accurate shape. The cavities are solid, stable over time and remotely reproducible. Thus, an efficient choice could be to produce anthropomorphic cavities filled with liquid mixtures. The question is which liquids are the most suitable to mimic living tissues in a wideband. In practice, tissues with water content, such as most of the brain parts, have high dielectric properties. Therefore using water as one of the components of the Tissue Mimicking Materials (TMMs) seems to be reasonable. For low permittivity tissues like bone and fat, liquid TMM can still be used by decreasing the percentage of water and adding liquid components that are miscible in water and have low permittivity such as Glycerin [Meaney *et al.*, 2017], Sugar [Hartsgrove *et al.*, 1987] and Triton X-100 [Joachimowicz *et al.*, 2018].

Pure Triton X-100 has dielectric properties similar to those of fatty tissues (whose permittivity is the lowest) on a wide band and is viscous providing stability to the mixture over time. Moreover, the use of a binary mixture, i.e. with two components, presents several advantages, including the ability to be modeled by a binary mixing law. Therefore, in this study, saltwater-based mixtures with TritonX-100 are investigated.

In conclusion, 3D printed liquid anthropomorphic human phantoms provide high accurate shape of the organ with dielectric properties in a wide band, reproducible, adjustable, reusable and easy to produce that none of the other type of phantoms can offer.

## **2.2 Tissue Mimicking Materials' (TMMs) fabrication**

This part is devoted to the prediction of the Triton X and salt concentration in mixtures for several types of tissues over wide range of frequency. In this part a description of relaxation phenomenon is presented (section 2.2.1). An experimental protocol is developed to produce the wideband mimetic mixtures (section 2.2.2). For dielectric characterization of mixtures open-ended coaxial probe is used. In section 2.2.3, the theory behind it is explained. To calculate the concentrations of components of the mixture mimicking different biological tissues, different binary laws are suggested in the literature. Section 2.2.4 is dedicated to comparison of outcome of three binary laws in order to identify the one with higher accuracy over a broad range of frequency. The selected binary model is introduced in an optimization code (section 2.2.5) that minimizes in an iterative way (Gauss-Newton technique [Walter, 2014]), a cost function that represents the difference between the reference values and those given by the binary law.

### **2.2.1 Relaxation models**

The first step to produce a mixture with dielectric properties close to the living tissues is having the dielectric properties of that organ as the reference values. The need for extensive data on the dielectric properties of human tissues as a reference is strongly felt among scientists and researchers involved in the interactions of electromagnetic (EM) fields and biological systems. Relaxation models are used commonly to extrapolate the measured relative permittivity of biological tissues to higher frequencies. The outcomes of these models are used as reference in the process of producing tissue mimicking materials.

Human body is made of between 50 to 70 percentage water. This is why biological tissues show lossy characteristics by being illuminated to EM waves. Both permittivity and conductivity of living tissues are highly nonlinear over frequency [Foster and Schwan, 1986]. This frequency



dependency is modeled mathematically by equations known as relaxation models such as Debye model and Cole-Cole model [Cole and Cole, 1941]. Cole-Cole relaxation models, for instance, are frequently used to model propagation in dispersive biological because they represent the frequency-dependent relative permittivity better than classical Debye models and over a wide frequency range [Maundy and Elwakil, 2012]. The parameters of these models are different for each tissue. By defining these parameters, the model function can be fitted to the dielectric properties of experimental data and track them over an arbitrary range of frequency.

When E-field is illuminated to a biological tissue at a certain frequency the dielectric dispersion takes place, the characteristic orientation motions of the dipoles result in a frequency variation of the dielectric constant and dielectric loss happens over a broad band of frequencies. Dielectric relaxation theory is the ability of polar molecules to align with the E-field. If the frequency of the electric field is sufficiently high, the molecular forces impeding the dipole orientation dominate and the dipole becomes unable to follow the changes. This frequency is called the relaxation frequency of the molecule. The phase lag between the external electric field and the dipole orientation enables the material to draw energy from the source and dissipate it in the form of heat. Since the polarization does not occur instantaneously, relaxation time is measurable for each tissue [Thakur and Singh, 2008; Said and Varadan, 2009].

One simple relaxation model is Debye model. Using this model the complex permittivity of the tissue ( $\epsilon_t(\omega)$ ) can be defined as:

$$\epsilon_t(\omega) = \epsilon_\infty + \frac{\epsilon_s - \epsilon_\infty}{1 + j\omega\tau} - j \frac{\sigma}{\omega\epsilon_0} \quad (2.1)$$

where the static permittivity ( $\epsilon_s$ ), the high frequency permittivity limit ( $\epsilon_\infty$ ), the relaxation time ( $\tau$ ) and the conductivity ( $\sigma$ ) are four parameters of the model which form corresponding response.

Dielectric properties values obtained from measurement data of living tissues mostly show a relaxation behavior that is far broader than the simple Debye type, which is due to the superposition of several relaxation processes. There are three relaxation processes mainly responsible for the dielectric properties of tissues: dipolar orientation, interfacial polarization, and ionic diffusion. The polarization does not occur instantaneously and as mentioned before this lag, which is due to, polarization is called the relaxation time. To be able to fit the data properly a modified function known as Cole-Cole is proposed to take into account the effect of the latter. Moreover, in Cole-Cole model one exponent factor ( $\alpha$ ) is added in addition to other parameters used in Debye model. Among works done in the literature on this topic Gabriel et al. provides detailed measurements of a variety of tissues up to 20 GHz [Gabriel et al., 1996]. They proposed a four-pole Cole-Cole model with the parameters obtained from the best fit to measured data.

According to the Gabriel's work, a database [IFAC, online] is provided on dielectric properties of different human tissues over the full frequency span managed (this span goes from 10 Hz up to 100 GHz in 10 decades). The model selected for the dielectric data across the frequency range is a summation of a four-pole Cole-Cole expression as reported in the text:

$$\varepsilon_t(\omega) = \varepsilon_\infty + \sum_{i=1}^4 \frac{\Delta\varepsilon_i}{1+(j\omega\tau_i)^{(1-\alpha_i)}} - j \frac{\sigma_i}{\omega\varepsilon_0} \quad (2.2)$$

Where  $\Delta\varepsilon$  is the magnitude of dispersion (magnitude of relaxation) between the "static" and "infinite frequency" dielectric constants,  $\omega$  is the angular frequency and  $\tau$  is a time constant (relaxation time).

This model has been chosen to compute the references values over the frequency range [500 MHz-6 GHz] of all the biological tissues considered in this study.

### 2.2.2 Mixture production protocols

Used in the framework on the EMERALD project, the manufacturing process has to be easily reproducible by an electrical engineer in a non-specific environment (no hood), and without drastic precautions (figure 2.4).



Figure 2.4. Non-specific environment and without drastic precautions.

The masses of TritonX-100 ( $m_{TX}$ ), NaCL ( $m_{NaCL}$ ), and H<sub>2</sub>O ( $m_{H_2O}$ ) are calculated for a given volume of the mixture  $V_{tot}$  according to the following. A protocol by addition of the mass is considered for producing the mixtures.

The concentration of NaCL in the mixture, denotes here  $S_{NaCL}$  and the volumic concentration of Triton X,  $V_{TX}/V_{tot}$  of each mixture are the output of an optimizing code explained in the section 2.2.5. From those quantities, we obtain

$$m_{NaCL} = S_{NaCL} \times V_{tot} \quad (2.3)$$

$$m_{TX} = V_{TX} \times \rho_{TX} \quad (2.4)$$

$$m_{H_2O} = (V_{tot} - V_{TX} - m_{NaCL}/\rho_{NaCL}) \times \rho_{H_2O} \quad (2.5)$$

With  $\rho_{H_2O}=1g/ml$ ,  $\rho_{TX} = 1.061 g/ml$ , and  $\rho_{NaCL} = 2.16 g/ml$ .

A digital balance scale, heater and stirrer, magnetic bars for stirring mixtures, and several beakers are standard lab equipment we used to produce our mixtures. The process can be summarized as follows:

- Tare the balance with an empty beaker.
- Add successively the masses of NaCl and deionized water and tare the balance between each step.
- Stir the solution with a magnetic bar - when the salt is dissolved, tare the balance.
- Add the mass of TritonX-100. Note that, the TritonX100 is very viscous at room temperature, and then it must be heated first separately in a 45 ° C water bath.
- Place the beaker in a water bath and stir the solution with a magnetic bar. The bath water must cover all the mixture. Note that the 40-60% solutions of TritonX-100, depending on their salt concentration, can be gelled at room temperature. It is therefore necessary to increase the temperature to obtain homogeneous mixtures in any case.
- Once the solution is homogeneous, pour it into an airtight container and keep the sample at room temperature and safe from light.

The dielectric properties of the liquid mixtures have to be close to those provided by the 4-pole Cole-Cole models and are accessible for each tissue on [IFAC, online]. Next, we will check if the produced TMMs can mimic on a wide frequency range the biological tissues. This will be done by comparison of the reference values given by IFAC with the measured dielectric properties of the manufactured mixtures. A non-invasive technique is chosen for the dielectric characterization of the mixture.

### 2.2.3 Dielectric characterization with an open-ended coaxial system

Several dielectric characterization techniques have been developed to measure the dielectric properties of biological tissues. Factors like material shape and form, accuracy and convenience determine the best method to use on each specific case. The main advantage about using the coaxial probe method to measure relative permittivity is being a non-destructive.

#### Description of the Open-ended coaxial system

Measured results presented in this thesis are all obtained using a homemade open-ended coaxial probe of GeePs coupled to a portable vector network analyzer (VNA) Rhode & Schwartz ZVB8 VNA.

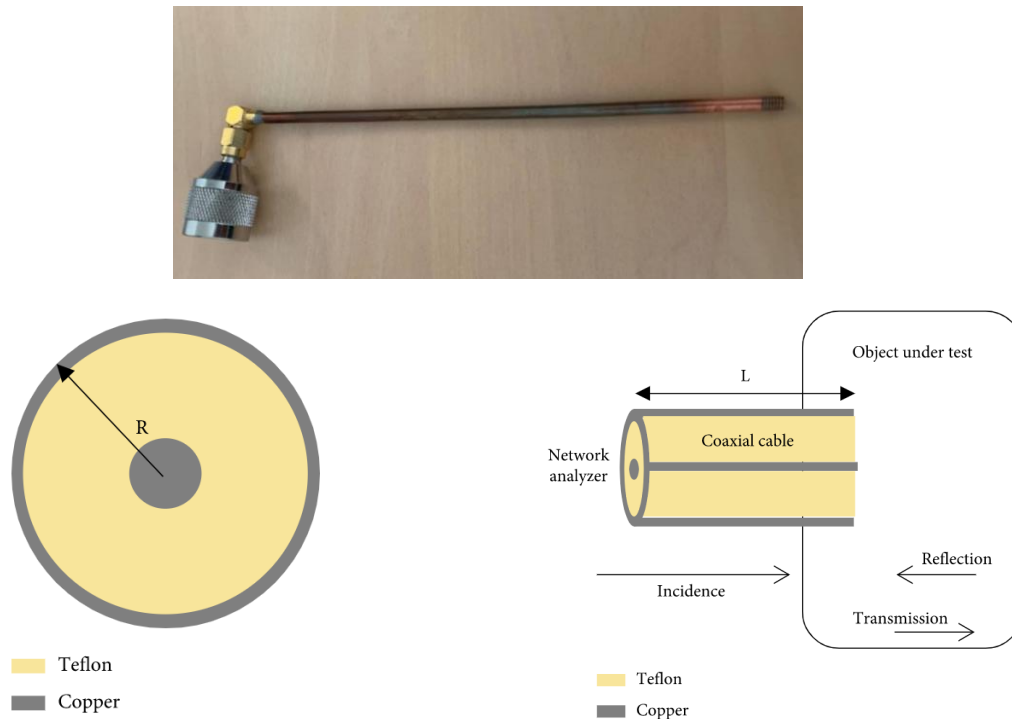


Figure 2.5: (a) The probe used for measurements in our laboratory. (b) The configuration of a coaxial cable. (c) Configuration of a permittivity measurement system using reflection methods [Wang *et al.*, 2020].

The open-ended coaxial cable reflection method is based on the measurement of the complex reflection coefficient at a single network port. Measuring these reflection coefficients the dielectric properties of the tissue under test can be calculated. The coaxial cable is built up from a 3.6-mm-diameter, 15-cm-long, Teflon-filled copper rigid coaxial cable.

### **Equivalent circuit model and calibration**

To calculate the dielectric properties of the tissue from the measured reflection coefficient, it is useful to use an equivalent circuit of an open-ended coaxial line. To do so, the end of the probe is considered as two capacitors in parallel (figure 2.6).  $C_f$  is the capacitance representing the electric field concentrated inside the Teflon and  $C(\omega)$  is the capacitance related to the fringing field in the unknown medium which is the product of  $C_0$  ( capacitance of the air-filled parallel plate) and  $\epsilon$  (the relative permittivity of the object under test). The conductance  $G(\epsilon)$  is radiation into the dielectric surrounding the cable and is frequency dependent.

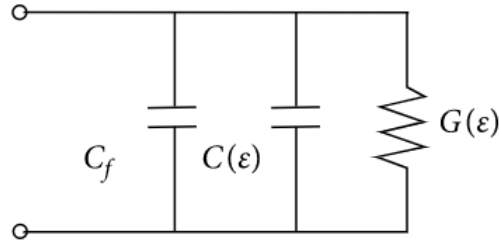


Figure 2.6: Circuit equivalent of the probe.

The equivalence admittance of open-ended coaxial cable can be calculated as:

$$Y = j\omega C_f + j\omega C(\epsilon) + G(\epsilon) = j\omega C_f + j\omega C_0 \epsilon + G(\epsilon) \quad (2.6)$$

From transmission theory, terminal admittance can be defined from the complex reflection coefficient ( $\Gamma$ ) as it is shown below:

$$Y = \left( \frac{1-\Gamma}{1+\Gamma} \right) \frac{1}{Z_0} \quad (2.7)$$

where  $Z_0$  represents the characteristic impedance of the coaxial line ( $50 \Omega$ ). Considering the negligible external radiation of the coaxial cable,  $G(\varepsilon)$  is assumed zero, which leads to an equation with complex permittivity ( $\varepsilon' + j\varepsilon''$ ) on one side and the reflection coefficient on the other side. Thus, the relative dielectric constant and the loss factor can be calculated using equations (2.6) and (2.7).

$$\varepsilon' = \frac{1}{2\pi f Z_0 C_0} \times \frac{-2|\Gamma| \sin(\varphi)}{1+2|\Gamma| \cos(\varphi)+|\Gamma|^2} - \frac{C_f}{C_0} \quad (2.8)$$

$$\varepsilon'' = \frac{1}{2\pi f Z_0 C_0} \times \frac{1-|\Gamma|^2}{1+2|\Gamma| \cos(\varphi)+|\Gamma|^2} \quad (2.9)$$

where  $|\Gamma|$  and  $\varphi$  are the modulus and phase of the reflection coefficient measured by the probe, respectively.

It is important to notice that the reflection coefficients measured by VNA ( $\Gamma_m$ ) at its port is not the one which should input in the equations. Due to the variation of the potential along the probe, it is needed to calculate the reflection coefficient  $\Gamma$  at the probe-mixture interface. This can be done by considering the probe equivalent to a Quadrupole.

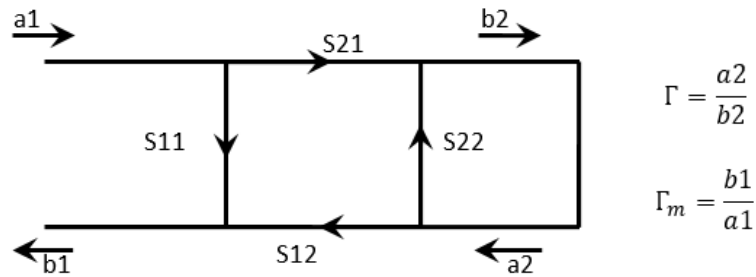


Figure 2.7: Quadrupole equivalent of the probe.

Thus, the reflection coefficient measured at the tip of the probe from the one measured by VNA is given by the following equation:

$$\Gamma = \frac{\Gamma_m - S_{11}}{S_{22}\Gamma_m + S_{12}S_{21} - S_{11}S_{22}} \quad (2.10)$$

$\Gamma_m$  is known since the VNA measures it, however the values of ( $S_{11}$ ,  $S_{21}$ ,  $S_{12}$ , and  $S_{22}$ ) on the right side of the formula are unknown. Therefore, to find the three unknown, three calibrations with three standards are necessary. Open circuit ( $\Gamma = 1$ ), short circuit ( $\Gamma = -1$ ), and calibration using distilled water are collaborations needed for the calculating  $\Gamma$  at the probe-mixture interface. It is noteworthy that the use of distilled water makes the system more suitable for measuring water-based liquids. In this case,  $\Gamma$  is obtained from the dielectric properties computed by a Stogryn model for a given temperature and frequency range [Stogryn, 1971].

#### 2.2.4 Selection of a fluid mixture law

Prediction of dielectric properties of mixtures composed of known components was a big challenge over years and several formulas has been proposed depending upon shape of inclusions, conductivity of the inclusions, etc. [Hasted, 1973; Kraszewski, 1977].

The permittivity of two components of the tissue mimicking mixtures proposed in this work, are provided from the literature given by Debye's models developed for salted water [Stogryn, 1971] and for fatty tissue [Lazebnik *et al.*, 2007], since the TritonX-100 has quite the same dielectric properties as the latter. Hence, if a binary law is able to trace the dielectric properties of TMM over a frequency range, it can be used to compute the dielectric properties of the mixture for a given concentration of salt and TritonX-100 for a given range of frequencies. The question is which binary law gives the best result in such a way that the dielectric properties of the mixture obtained by applying this binary law are the closest to those given by the relaxation model of the target biological tissue.

The theories, which can be used for studying the dielectric properties of emulsions, are based on the influence of obstacles in an electric field [Rayleigh, 1892; Wiener, 1912] and the permittivity



of molecular mixtures [Mossotti, 1846; Onsager, 1936]. In this part, three of most well-known theories which are used in the literature are investigated (Böttcher, Lichtenecker, Looyenga). Considering the studies based on the static permittivity of emulsions, any passive and homogeneous medium is made of two phases, a dispersed one and a continuous one. The dispersed phase (D) is made of spherical micelles, which has small dimensions compared to the medium. The volume fraction  $V_D$  and  $V_C$  are occupied by phase D (in our case TritonX-100) in the total volume and the continuous phase C (saline water) in the same volume, relatively. Hence, the aggregation of these two volume fractions is a unit ( $V_D + V_C = 1$ ). The dielectric properties of components are defined as the dielectric constant of the dispersed phase ( $\epsilon_D$ ) and continuous phase ( $\epsilon_C$ ).

Böttcher law is one of the theories based on molecular models [Böttcher and Bordewijk, 1978]. The classical molecular theories on the dielectric behavior of mixtures always sum up to the calculation of average dipole moments of each molecular species to determine the relative permittivity  $\epsilon_E$  can be determined by using the definition of the polarization:

$$\epsilon_0(\epsilon_E - 1)\mathbf{E} = \sum_j N_{Mj} \langle \mathbf{m}_j \rangle \quad (2.11)$$

In this expression  $\epsilon_0$  is the permittivity in vacuum,  $\mathbf{E}$  the macroscopic field in the dielectric,  $N_{Mj}$  the number of molecules of the  $j$  species by volume unite and  $\langle \mathbf{m}_j \rangle$  their average dipole moment. To calculate the average molecular moments it is needed to consider that a permanent dipole moment and a polarizability  $\alpha_j$  are given to the molecules of each species. Moreover, by illumination of the macroscopic field  $\mathbf{E}$ , a local field  $\mathbf{F}_j$  is created where the molecule of the  $j$  species is.

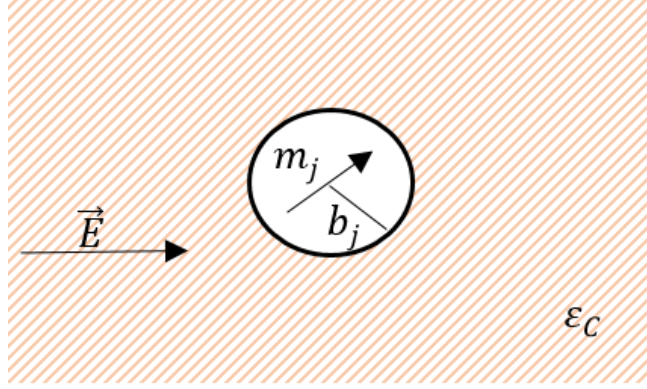


Figure 2.8: Böttcher cavity.

In Böttcher theory [Böttcher and Bordewijk, 1978], the system is modeled as spherical cavities with radius of  $b$  in a continuous system with relative permittivity of  $\epsilon_C$ . The local field is a uniform field and results from the cavity field  $\mathbf{C} = (3\epsilon_C/(2\epsilon_C + 1))\mathbf{E}$  and reaction field  $\mathbf{R}_j = [2(\epsilon_C - 1)/(2\epsilon_C + 1)][(\bar{\mathbf{m}}_j/4\pi\epsilon_0 b_j^3)]$ . Böttcher came up with the following expression for permittivity by using the Onsager theory [Onsager, 1936] for emulsions:

$$\epsilon_0(\epsilon_E - 1) = \frac{3\epsilon_E}{2\epsilon_E + 1} \left[ \frac{N_D a_D}{1 - \frac{2(\epsilon_E - 1)}{2\epsilon_E + 1} \frac{a_D}{4\pi\epsilon_0 a_D^3}} + \frac{N_C a_C}{1 - \frac{2(\epsilon_E - 1)}{2\epsilon_E + 1} \frac{a_C}{4\pi\epsilon_0 a_C^3}} \right] \quad (2.12)$$

With  $a_D$  and  $a_C$  the polarizability of dispersed and continuous phase molecules, respectively. From equation 2.12 the well-known Böttcher mixture model can be derived:

$$\frac{(\epsilon_E - \epsilon_C)(2\epsilon_E + \epsilon_D)}{3\epsilon_E} = V_D(\epsilon_D - \epsilon_C) \quad (2.13)$$

Where  $V_D$  is the volume fraction of TX-100 and  $\epsilon_D$  and  $\epsilon_C$  are dielectric properties of TX-100 and saline water which are respectively described over a microwave frequency range by the Debye model.  $\epsilon_E$  is the dielectric properties of the emulsion.

By Lichtenecker theory, an expression of the permittivity of system with two components can be obtained with three mathematical hypothesis explained in [Lichtenecker, 1931].

$$\ln \varepsilon_E = V_D \ln \varepsilon_D + (1 - V_D) \ln \varepsilon_C \quad (2.14)$$

Looyenga theory considers a homogenous emulsion as the succession of regions whose concentrations are slightly different. As developed in [Looyenga, 1965], a new equation is proposed for the calculation of the dielectric properties of the mixture:

$$\varepsilon_E^{1/3} = V_D \varepsilon_D^{1/3} + (1 - V_D) \varepsilon_C^{1/3} \quad (2.15)$$

Next, we will produce and characterize several salted water TritonX-100 mixtures. Considering Cole-Cole model as the reference, the measured dielectric properties of the mixtures of different tissues should be in a close match with the reference values given by Cole-Cole models in a wide range of frequency. Starting from the Spleen tissue mixture, we tested different concentrations of TX-100 and saline water to find empirically the best concentrations.

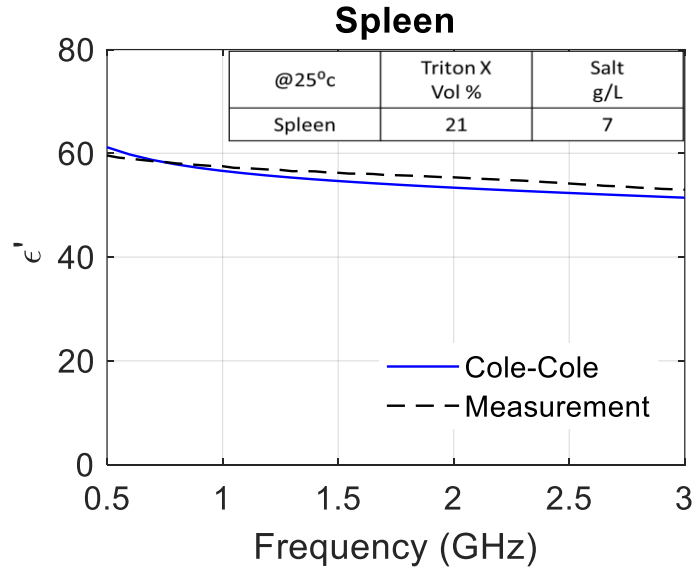


Figure 2.9: Comparing relative permittivity of Spleen based on Cole-Cole model and measurement with defined concentrations.

Figure 2.9 compares the dielectric properties of the mixture for 21% of Triton X-100 and 7g/L of NaCL with the values given by the Cole-Cole model for the Spleen tissue over the frequency range [1 - 3 GHz]. There is a good match between the measurement and the reference model (see

figure 2.9). Thus, by inputting these concentrations in different binary laws, it is possible to check the outcome of each binary law and pick the one with less error.

Several binary laws have been tested using the experimental values of Triton-X and salt's concentrations. Among them, the Böttcher law represents the best results over the [0.5-3] GHz frequency range, according to the measured calculated dielectric properties of the liquid mixture mimicking Spleen given on figure 2.10. This result has been observed for all the mimicked biological tissues produced.

As a conclusion, the Böttcher law is the one that best fits the measurement results. Therefore, we will consider it as the most appropriate one for the theoretical representation of saltwater and TritonX-100 mixtures. In the next section, this law will be introduced in an optimization algorithm, which, by iterative adjustments of the salt and TritonX-100 concentrations will minimize the difference between the reference values of the Cole-Cole models and the one given by the Böttcher law.

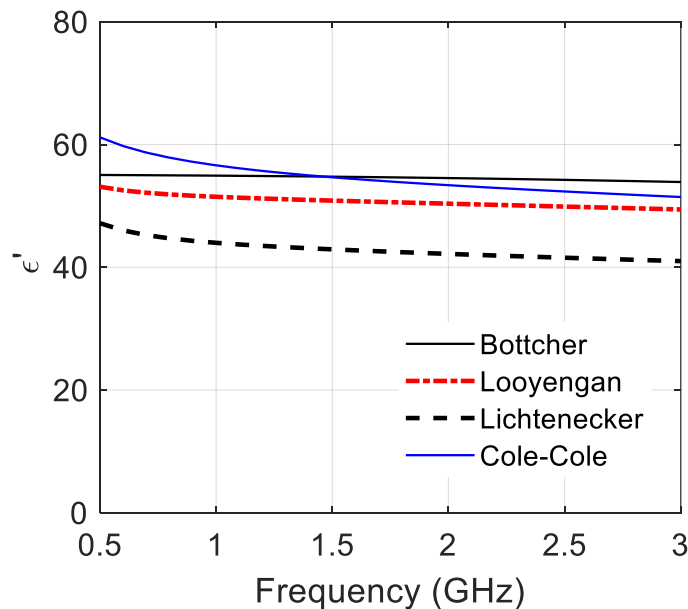


Figure 2.10: Comparison between different binary laws and Cole-Cole model for the spleen tissue.

### 2.2.5 Optimization code

After selecting the Böttcher binary law to model the mixture, we look for the exact concentration of the components of TMMs. Instead of finding it empirically, an optimization code has been developed to adjust the amount of Salt and TX-100 concentration, @  $T=25^{\circ}\text{C}$  (room temperature) for each tissue by minimization a cost function which represents the quadratic error between the complex permittivity values given by the Böttcher law and the Cole-Cole model [IFAC, online].

We assume that the TX100-saline water mixture is a binary mixture, for which both the Debye's model for the Triton X-100 (group three [Lazebnik *et al.*, 2007]) and that for saltwater [Stogryn, 1971] are known. The complex permittivity of the mixture is computed using the Böttcher formula (equation 2.13), and compared to the reference values given by the Cole-Cole model for a given tissue, in a specific frequency range.

Hence, the Triton-X and salt concentrations ( $V_D, S_E$ ) need to mimic a specific tissue that can be computed by fitting the complex permittivity of the mixture model  $\epsilon_E$  to the one of the tissue  $\epsilon_t$  over a specific frequency range. This is done by using a Gauss-Newton process [Walter, 2014], where at each iteration, the NaCl concentration and volume fraction of Triton-X are determined at discrete frequencies over  $[0.5 \text{ GHz} - 3 \text{ GHz}]$ , by minimizing the cost functional  $J = \sum_f \omega_f |\epsilon_E - \epsilon_t|_f^2$ , where  $\omega_f = 1/|\epsilon_t|_f^2$ . The inputs of this procedure are the Debye model of TritonX-100 and salt water and the reference model of the dielectric properties of the target tissue. This reference model can be the four-pole Cole-Cole model presented in [IFAC, online] or the ex-vivo and in-vivo measurements performed on the tissue of interest in the literature. The outcomes of the optimization process are the needed volume fraction of Triton-x 100 and the amount of salt to produce a mixture mimicking the dielectric properties of the target tissue.

The quadratic cost function is approached by its first (gradient  $\mathbf{g}$ ) and second (approximate Hessian  $\mathbf{H}$ ) derivatives with respect to the NaCl mass concentration and Triton-X volume fraction, which are computed analytically.

$$\mathbf{g} = 2 \sum_f \omega_f \Re e[(\varepsilon_E - \varepsilon_t)_f^* \mathbf{\varepsilon}_E]_f \quad (2.16)$$

$$\mathbf{H} = 2 \sum_f \omega_f \Re e(\varepsilon_E'^* \varepsilon_E'^\dagger)_f \quad (2.17)$$

In the above equations  $\varepsilon_E' = (\partial \varepsilon_E / \partial V_D, \partial \varepsilon_E / \partial S_E)^\dagger$  where  $S_E$  indicates the NaCl concentration of the mixture,  $V_D$  the Triton-X volume fraction,  $*$  the conjugate, and  $\dagger$  the transposition.

Then by considering equation 2.13,  $\varepsilon_E'$  becomes:

$$\varepsilon_E' = \left( \frac{3\gamma(\varepsilon_D - \varepsilon_C)/(4\delta)}{[(\gamma(3V_C - 1) + 4\varepsilon_D)/(4V_C\delta)] \partial \varepsilon_C / \partial S_C} \right), \quad (2.18)$$

With:

$$\begin{aligned} \gamma &= \delta - \eta, \quad \delta = (\eta^2 + 8\varepsilon_D\varepsilon_C)^{1/2} \\ \eta &= \varepsilon_D - 2\varepsilon_C - 3V_D(\varepsilon_D - \varepsilon_C). \end{aligned}$$

As it is mentioned in [Joachimowicz *et al.*, 2018] the term  $\partial \varepsilon_C / \partial S_C$  can be inferred from the salted water parametric model [Stogryn, 1971], where  $S_C$  represents the salt concentration saline water.

At iteration step  $k+1$ ,  $\mathbf{x} = (V_D, S_E)^\dagger$  the solution reads:

$$\mathbf{x}^{k+1} = \mathbf{x}^k - \mathbf{H}^{-1}(\mathbf{x}^k) \mathbf{g}(\mathbf{x}^k) \quad (2.19)$$

This process converges towards a stable solution in a few iterations, most of the time independently of the initial NaCl concentration and Triton-X volume fraction, by inverting at each iteration, the approximate Hessian matrix  $\mathbf{H}$  of rank 2.

Initial run of the optimization algorithm allowed adjusting numerically the concentration of TX-100 and salt, required to produce TMMs with dielectric properties similar to 10 biological tissues, at room temperature, over a wide frequency range [Abedi *et al.*, 2019]. Table 2.1 shows the results at 1.5 GHz provided by the optimization code for 10 mixtures.

Table 2.1. Outcome of the optimization code for 10 new biological tissues at 1.5 GHz, by using Böttcher's law as the binary law. Last two columns belong to Cole-Cole model, which is the reference model of dielectric properties of biological tissues in the literature [Abedi *et al.*, 2019].

@ 25°C, 1.5 GHz	Mixture		Böttcher		Cole-Cole	
Tissue	TX-100 vol %	NaCl g/L	$\epsilon_r$	$\sigma$ S/m	$\epsilon_r$	$\sigma$ S/m
Stomach	12	7	63.7	1.5	63.8	1.5
Spleen	20	7	55.1	1.5	54.7	1.6
Liver	30	5	45.1	1.0	44.9	1.1
Small Intestine	16	14	57.0	2.5	56.8	2.5
Gall- bladder	16	7	58.6	1.5	58.5	1.5
Kidney	19	8	56.0	1.6	55.4	1.7
Colon	19	6	56.1	1.3	55.9	1.4
Heart	17	7	57.6	1.4	57.2	1.6
Nerf	44	4	31.5	0.7	31.3	0.7
Lung Inflated	56	4	21.3	0.6	21.2	0.6

The concentrations given by the optimization process, lead to a good match for all 10 tissues for both the permittivity and the conductivity. Next is concerned with the experimental validation of the TMM recipes.

### **2.2.6 Experimental validation**

The 10 mixtures were produced according the protocol given section 2.2.2, and their dielectric properties are measured using the open-ended coaxial probe method described section 2.2.3. As already mentioned this method is simple, non-destructive, in a wide frequency bandwidth and suitable for measuring semi-solid materials.

#### **2.2.6.1 Production and characterization of the 10 mixtures**

Several mixtures including different concentration of TX-100 and saline water for 10 different human tissues based on the outcome of the optimization code, were produced. After each measurement, results were compared with the Cole-Cole model. To have more accurate results, in the other words reducing the error between the measured results and Cole-Cole model, the amount of TX-100 or salt was changed slightly. Results presented in figure 2.11 validate the generalization of the process to any biological part of the body and show that it is possible to make mixtures mimicking the dielectric contrasts between the different tissues on a wideband. Those results were validated by the reproduction of the mixtures and their dielectric characterization done at National University of Ireland Galway (NUIG).



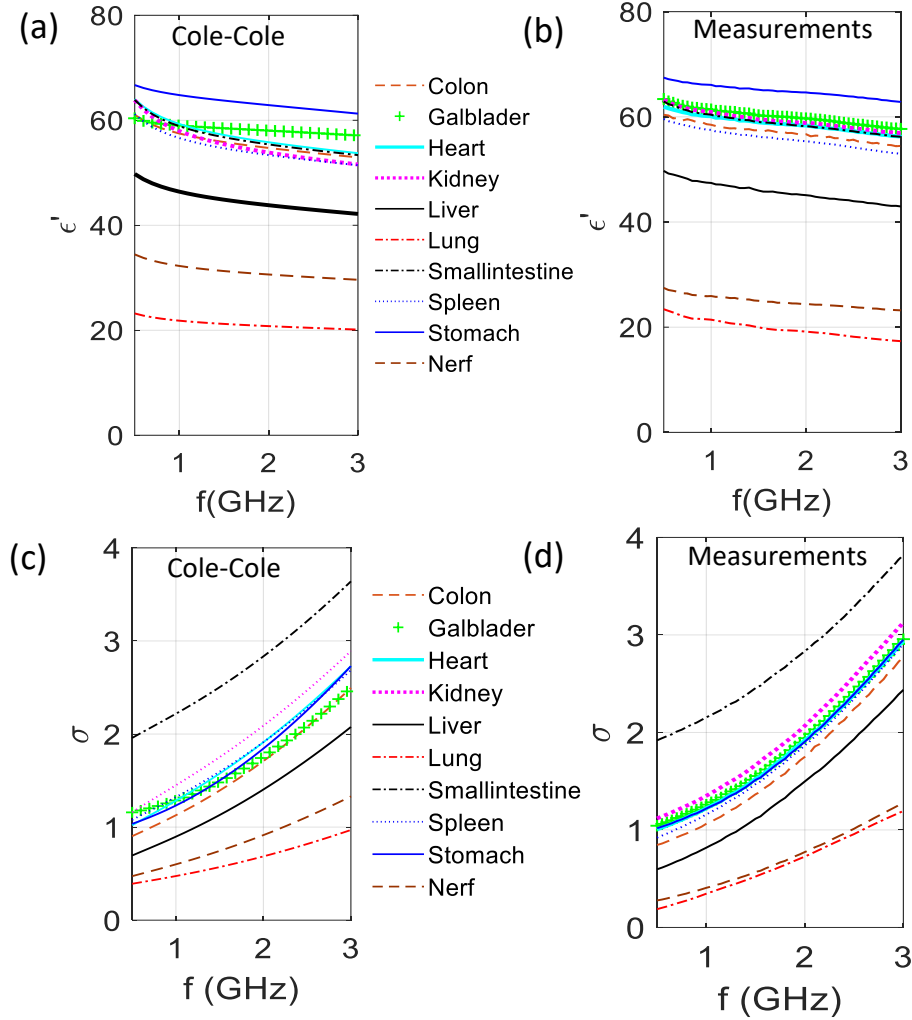


Figure 2.11: Comparison of the dielectric constant and conductivity of 10 different biological tissues of the values obtained from the Cole-Cole model with the measured values of produced mixtures at room temperature, over the [500 MHz - 3 GHz] frequency range.

### 2.2.6.2 Reproducibility of the results–NUIG/CNRS

One of the reasons that liquid phantoms seem to be more practical is that the mixtures are easily reproducible remotely in different labs and this is due to the fact that mixing certain amount of salt, water, and TX-100 will result in an exact value of permittivity and conductivity in all around the world. Figure 2.12 is a demonstration of that. As a member of the EMERALD group, we are designing a protocol for other groups in the project to be able to test their MWI systems and algorithms. This process has to be simple and an electrical engineer should be able to remotely reproduce the mixtures and obtain same results as we did.

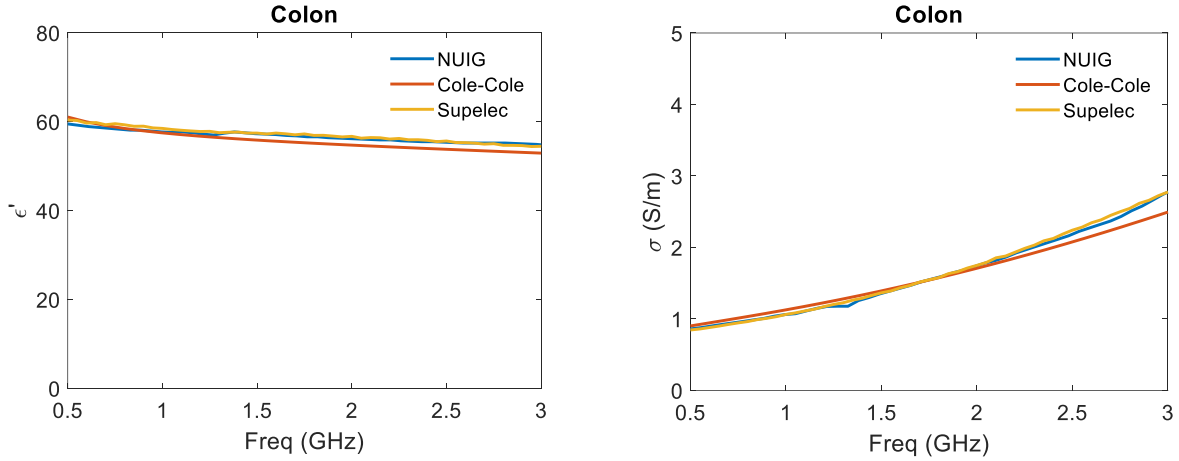


Figure 2.12: dielectric properties of Colon measured in France and Ireland compared with Cole-Cole model.

Figure 2.12 shows that the results of our measurements on mixtures produced in different labs (Supelec-FR / NUIG-IR) are the same. The set-ups used different probes (homemade / Keysight) and different network analyzers (Rhode & Schwartz ZVB8 VNA / Keysight E5063A). This proves the fact that the process and the results are reliable in different lab and with different set-ups.

### 2.2.6.3 Flowchart to produce the mixture

As the summary of this part, we are presenting a simple flowchart (figure 2.13), which indicates the process to follow to have mixtures with similar dielectric properties as biological tissues is introduced. Starting with calculating the concentration of the components of the mixture given by the optimization process, producing the mixture based on the protocols and in the end characterizing the dielectric properties of the mixtures and comparing them with the measured values or Cole-Cole model of that specific organ. To reduce the error between the measurements and the Cole-Cole model the concentrations need to be changed slightly and the production has to be done again.

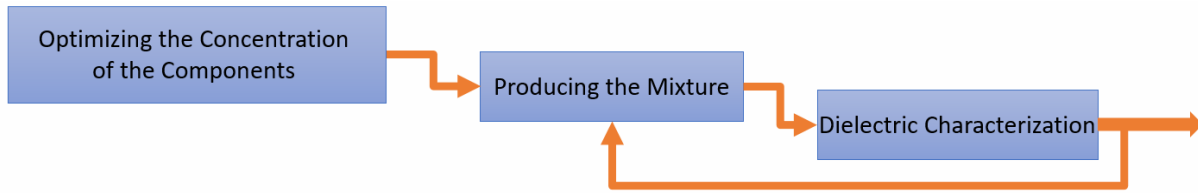


Figure 2.13: Diagram of preparation of the mixtures.

However, it is noteworthy that the TX-100 - salted water mixtures are significantly easy to produce, except when the TX-100 volume percentage is approximately in the 40 – 60% range since the mixture is rather viscous at 25°C. This phenomenon decreases by increasing the temperature and amount of salt. Indeed, very few TMM are concerned with this problem at room temperature. However, for the latter, the mixture components have to be warmed separately, then mixed, vigorously stirred and leave to rest at 45° C for a few minutes until air bubbles vanished. Note also that for those cases, the quantity of salt and TX100 can be adjusted experimentally to obtain a liquid mixture that has dielectric properties close to the expected values at the given temperature.

The next section is devoted to the fabrication of 3D printed anthropomorphic cavities filled with the outlined mixtures.

## 2.3 Development of anthropomorphic printable cavities

Choosing liquid phantoms for testing microwave imaging systems lead to make cavities as containers. These cavities should have similar shape as the organ of human body. To introduce this process, we first review 3D printing used in medical applications.

### 2.3.1 3D printing for medical application

In recent years, some researchers used 3D printing technology to make phantoms. In addition to surgical planning applications, 3D printed phantoms are essential for the validation of medical

computational models, as well as for medical training and patient education. In [Wang *et al.*, 2017] there is a comprehensive recent review of the state of the art along with new developments and trends in 3D printed functional medical phantoms (i.e. tissue-mimicking medical phantoms, radiologically relevant medical phantoms, and physiological medical phantoms) and 3D bio-printed structures (i.e. hybrid scaffolding materials, convertible scaffolds, and integrated sensors) for regenerated tissues and organs. Another research on 3D printed tumors helps researchers on the study of metastasis and leads to facilitate complex treatment, surgery and therapies [Haleem *et al.*, 2020]. In this way, 3D printing can significantly improve patient comfort and treatment accuracy [Asfia *et al.*, 2020]. In the microwave imaging domain, anthropomorphic head phantoms were developed by printing 3D molds intended to be filled with gel-based parts of the head [Mobashsher and Abbosh, 2015; Pokorny and Tesarik, 2019] or mixtures based on graphite carbon black polyurethane [Garrett and Fear, 2015; McDermott *et al.*, 2017]. A review for the development of anthropomorphic breast phantoms is given in [Khuda, 2017]. In this work, we took advantage of this recent development in 3D printing technology to engineer anthropomorphic cavities.

### **2.3.2 Modeling and printing 3D cavities**

To develop realistic phantoms for microwave imaging it is crucial to get as close to the anatomy. To obtain the outline of a biological organ there are several options. We can take advantage of online phantom libraries like [Plasticboy, online] or obtain the shape of the organ from the segmentation of MRI/CT scan. Here we are going to shed lights on the segmentation techniques by introducing the 3D Slicer software. Then the files are modified with the CAD software Blender to develop printable cavities in such a way that the resulting phantom is fillable and compatible

with the experimental system. The numerical version of the obtained phantom at the end of the process must be readable by 3D printers, i.e. in STL format.

### 2.3.2.1 STL format files

STL (an abbreviation of "stereolithography") is a file format native to the stereolithography CAD software created by 3D Systems [Roscoe, 1988]. STL has several backronyms such as "Standard Triangle Language" and "Standard Tessellation Language" [Grimm, 2004]. This file format is supported by many other software packages; it is widely used for rapid prototyping, 3D printing and computer-aided manufacturing [Chua *et al.*, 2010]. STL files describe only the surface geometry of a three-dimensional object without any representation of color, texture or other common CAD model attributes. The STL format specifies both ASCII and binary representations. Binary files are more common since they are more compact.

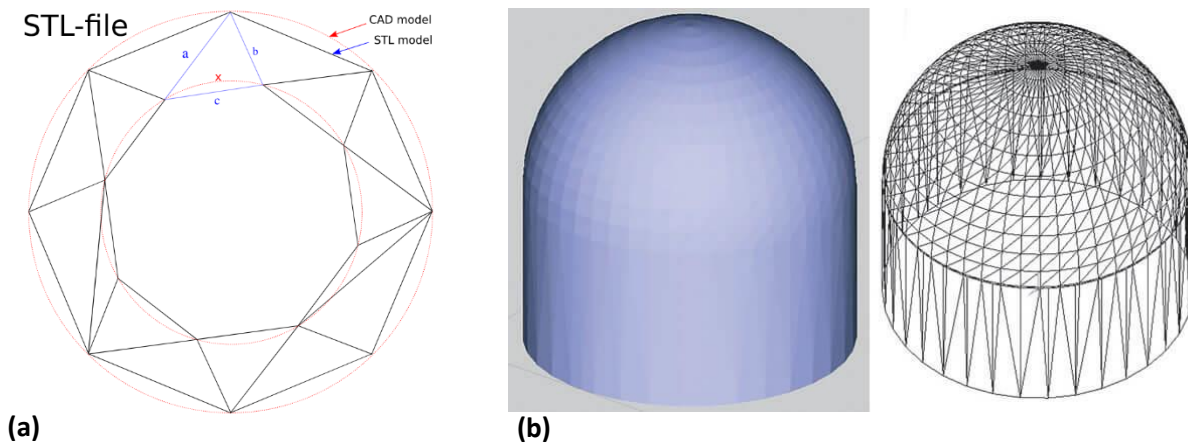


Figure 2.14: (a) 2D CAD representation of a torus (shown as two concentric red circles) and an STL approximation of the same shape (composed of triangular planes). (b) 3D representation of CAD and STL format of an object.

An STL file describes a raw, unstructured triangulated surface by the unit normal and vertices (ordered by the right-hand rule) of the triangles using a three-dimensional Cartesian coordinate system. Thus, the STL files define the coordinates of each organ of the human body.

### 2.3.2.2 Segmentation with 3D Slicer

3D Slicer is a software application for visualization and analysis of medical image computing data sets. All commonly used data sets are supported, such as images, segmentations, surfaces, annotations, transformations, etc., in 2D, 3D, and 4D. Visualization is available on desktop and in virtual reality. Analysis includes segmentation, registration, and various quantifications.

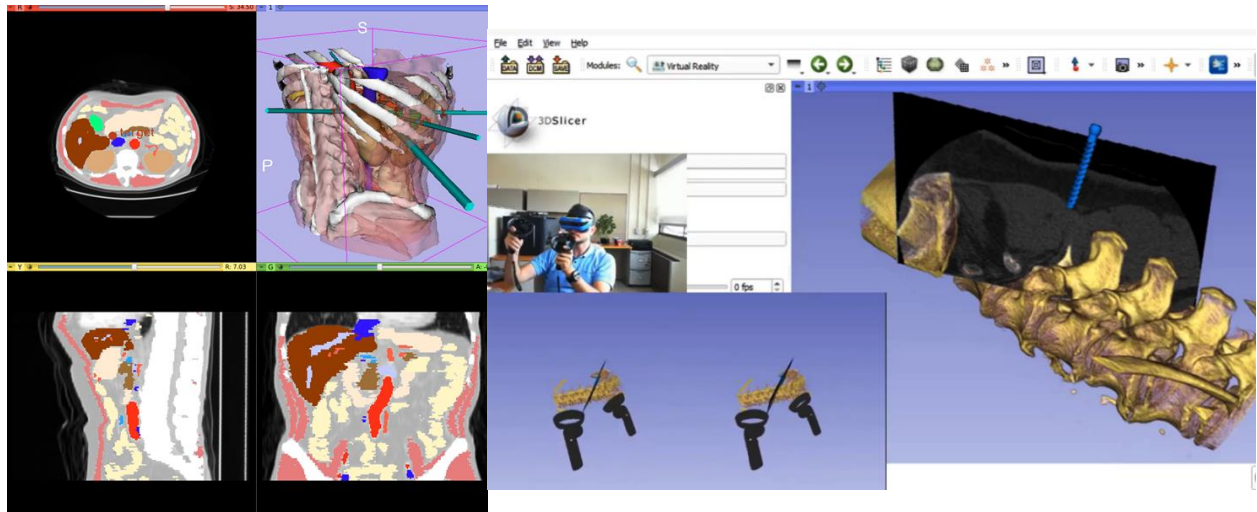


Figure 2.15: Two different functions of 3D Slicer, adding surgical ports and virtual reality.

It is a research software platform, which allows researchers to quickly develop and evaluate new methods and distribute them to clinical users. The software provides product development platform, which also allows companies to quickly prototype and release products. Developers can focus on developing new methods and do not need to spend time with redeveloping basic data import/export, visualization, interaction features. The application is designed to be highly customizable (with custom branding, simplified user interface, etc.). 3D Slicer is completely free and there are no restrictions on how it is used - it is up to the software distributor to ensure that the developed application is suitable for the intended use [3D slicer, online].

Uploading the DICOM images in the software, we will have access to all layers of these images in three different views. Figure 2.16 shows MRI of head in three views.

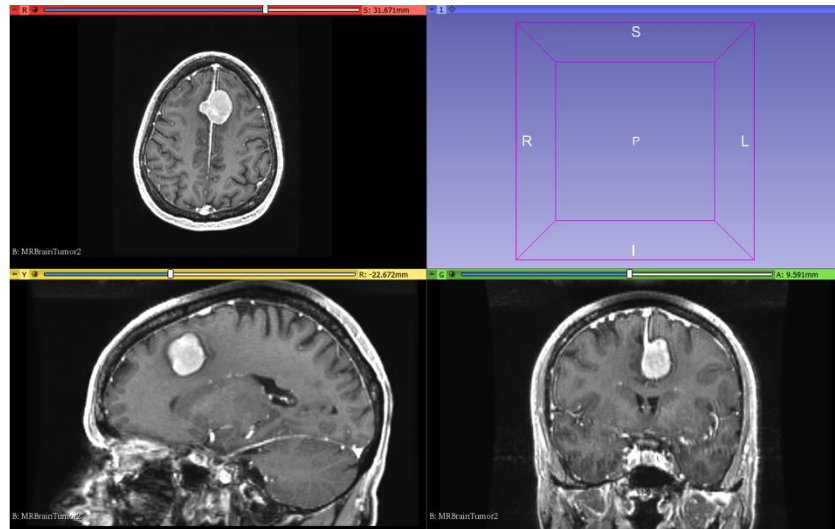


Figure 2.16: MRI of head in 3D Slicer for three views.

Using 3D slicer we are able to choose different parts of the head, detected based on contrast difference, and extract chosen area. In figure 2.16, there is a tumor inside the brain. By setting the right threshold to distinguish the contrast of the tumor tissues from the brain tissues, we can have a 3D model of the tumor. This is shown in figure 2.17.

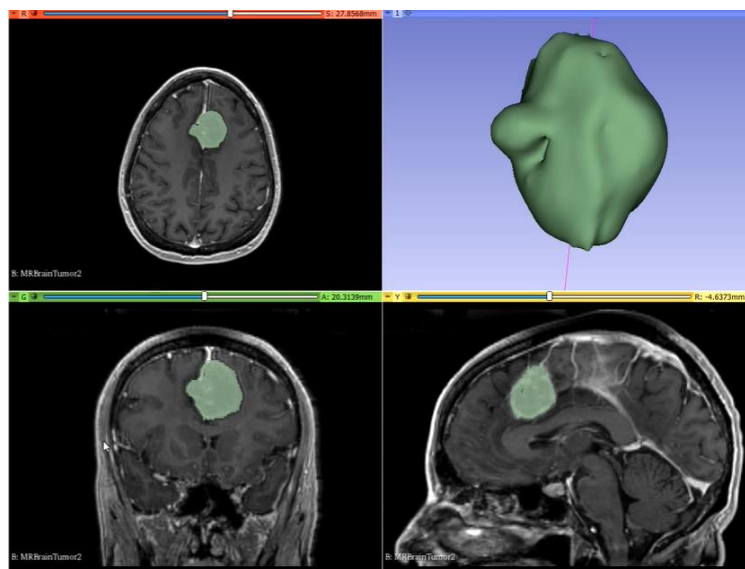


Figure 2.17: 3D model of segmented tumor.

This technique is applicable to different parts of human body. After extracting the 3D model of the target organ, 3D Slicer gives us a tool to export STL format of the model. This file format is it

is widely used for rapid prototyping, 3D printing and computer-aided manufacturing. The STL format specifies both ASCII and binary representations. Binary files are more common, since they are more compact. This means these numerical versions of the model can be used in inverse algorithms as well. This topic will be covered in the chapter 4.

### 2.3.2.3 Design and realization with Blender

Blender is a free and open source graphic software helping us adjusting 3D models and preparing them for 3D printing.

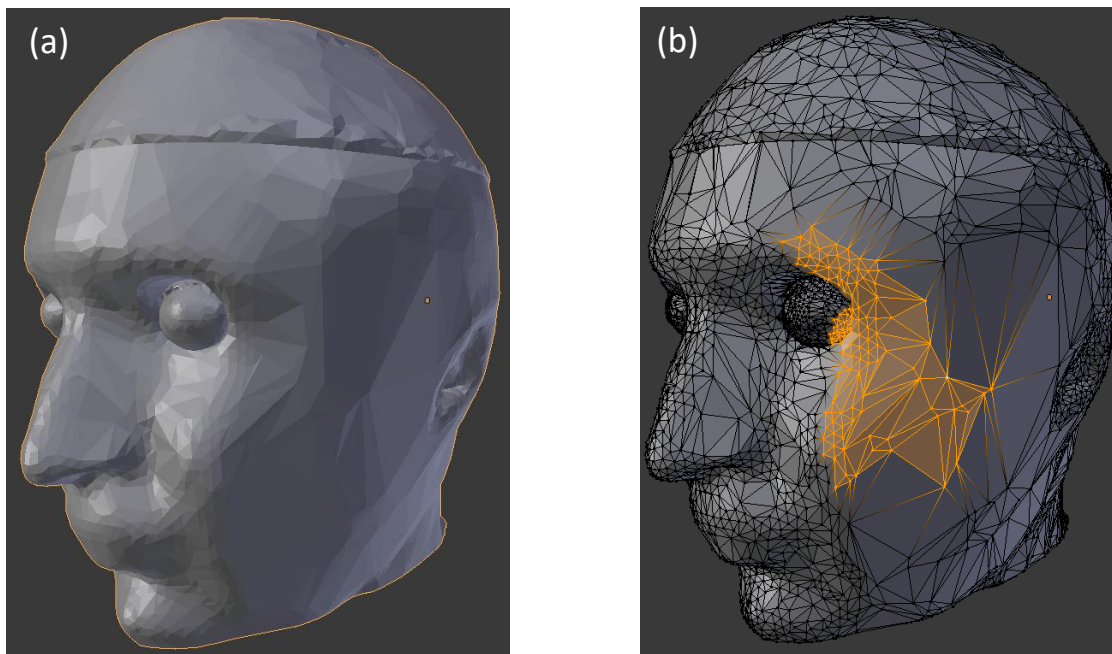


Figure 2.18: (a) Imported a 3D model of head (object mode) and (b) the meshed version of the model prepared by Blender (edit mode) ready for further adjustments.

Blender offers several interaction modes. Object mode represents the shape of the model after 3D printing. By entering the edit mode one can observe that the model is meshed by triangles and several tools provided by Blender make it possible to change the shape and all corners of the 3D model precisely (see figure 2.18 b). After applying these changes, by going to the object mode the effect of adjustments can be seen.



Blender provides a variety of tools for editing meshes. These are tools used to add, duplicate, move and delete elements (each triangle is an element), which allow us to shape the 3D model as it is desired. Boolean is an operation can be done to selected objects in Blender. This tool is needed to make cavities out of the 3D model exported from 3D slicer. Moreover, solidifier is another tool to define a thickness to the outer shell of the designed cavity.

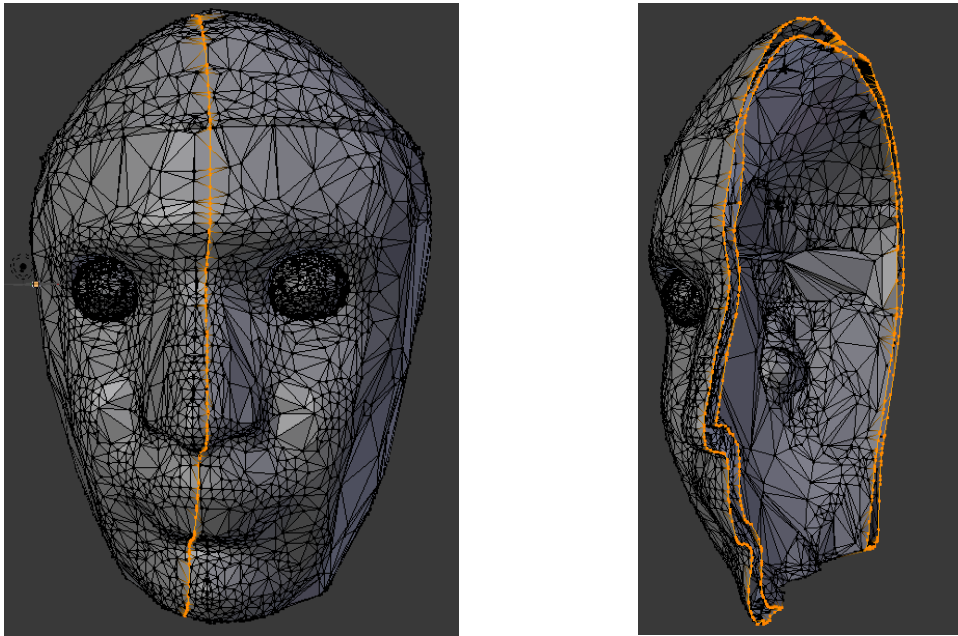


Figure 2.19: Selection of one cut of the model to indicate the thickness of the head phantom.

After designing and finalizing the 3D model of the phantom, in the 3D printing section on the software it is possible to check if the model is printable. In case the file is not printable, the software gives us the option to see where the problem is. This is a useful tool to avoid loss of materials while printing and malfunction of the 3D printer.

#### 2.3.2.4 Application to the realization of a brain cavity

To obtain the STL format file of a 3D model, a MRI scan of the organ of interest is needed, as for instance, the brain. This image (see figure 2.20) contains three images in different slices of the brain then putting these all together, one can obtain the 3D model of the head.

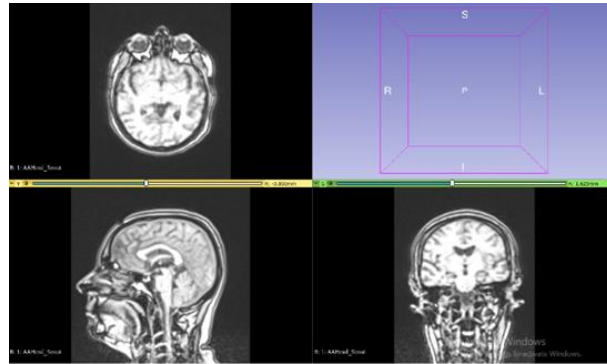


Figure 2.20: MR Image of the head, files were imported to the 3D Slicer for segmentation.

Since the MRI scan of the head contains different organs like skull, eyes, muscles, teeth, etc. then we have to be able to extract the brain from it, as described before. By using the segmentation tool provided by 3D Slicer and choosing the right threshold, we will be able to segment and extract the brain from the head. The software offers exporting the file in different formats including the STL format.

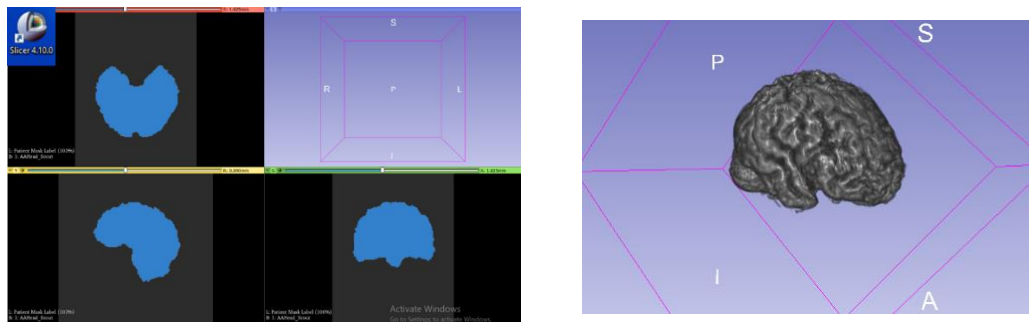


Figure 2.21: Segmented brain and the outcome of the software for extracting the brain form the MR image of the head.

The extracted brain shown in figure 2.21 is exported as an STL file.

## 2.4 GeePs anthropomorphic phantoms

The main goal of this thesis is to develop standardized phantoms, which provides unified benchmarks and allow comparing the results achieved by EM imaging with other modalities. These phantoms are designed to be used in different microwave imaging systems, by other research groups in EMERALD project. They will be realized with 3-D printed technology. The 3D printed cavities will be filled with liquid mixtures that mimic different tissues at microwave frequency.

As it is defined in the framework of the EMERALD project, the manufacturing process used to build up accurate ultra-wideband (UWB) phantoms that have to be easily reproducible by an electrical engineer in a non-specific environment without extreme precautions, and to some extent at low cost. In the next sections, we present three phantoms: head, thorax and ablated liver, adapted to the experimental setups developed in the EMERALD project. These phantoms have been designed and developed according to the process described in this work.

### 2.4.1 Head phantoms designed for POLITO system

Brain stroke is one of the most common cardiovascular diseases causing permanent injuries or even death [*World health report*, online]. There are two types of strokes either ischemic (having a clogged vessel) or hemorrhagic (having a broken vessel) and the treatments are completely different. Thus, a clear understanding of the type of stroke is vital before starting any treatment.

In [*Tobon Vasquez et al.*, 2020] a novel prototype is presented and characterized. The MWI device is developed at Polytechnic University of Turin and as a part of our collaboration to the EMERALD project we have designed and 3D printed head phantoms for testing this MWI system.

### 2.4.1.1 POLITO system

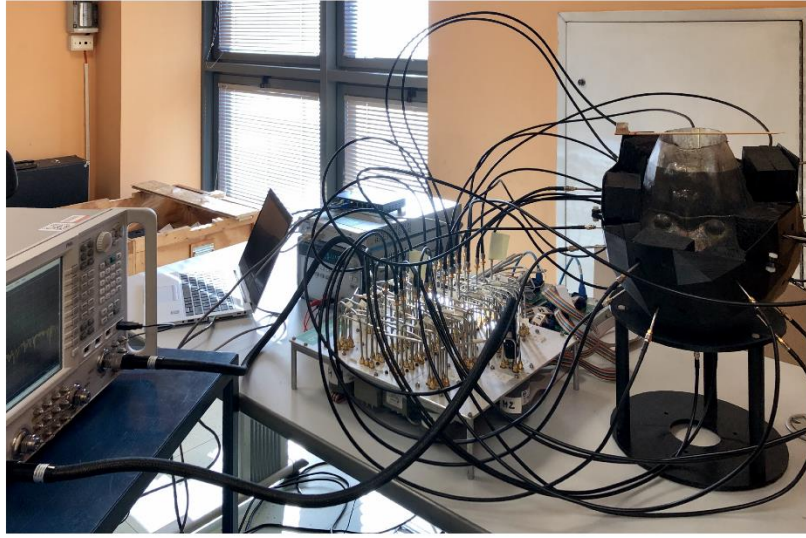


Figure 2.22: POLITO MWI system. From left to right: VNA, switching matrix and head phantom wearing a helmet interconnected to the switching matrix by means of coaxial cables [Tobon Vasquez *et al.*, 2020].

For providing 3D images of head, 24 antennas are organized as an anatomically conformal shape forming a helmet providing the information for 3D image of head. Each antenna is embedded in a box of graphite-silicon material, acting as the coupling medium, and connected to a two-port VNA through a  $24 \times 24$  switching matrix, which allows the whole differential scattering matrix required for imaging to be acquired [Tobon Vasquez *et al.*, 2020]. Anthropomorphic head phantoms designed in our group are compatible to this system. The phantom is going to be inserted in the blocks of antennas upside down.

### 2.4.1.2 Head cavities

Since these cavities have to be fitted in a microwave imaging system in Polytechnic Torino, they are designed in upside down configuration (Fig 2.23). Figure 2.23 shows 3D printed phantoms with one, two and three cavities from left to right, respectively. The material used to print these

phantoms is acrylonitrile butadiene styrene (ABS), which is resistance to Triton-X 100. The thickness of the different cavities of the head phantom varies between 2 to 8 mm.



Figure 2.23: Upside down head phantoms, prepared for the POLITO microwave imaging system.

The reason behind having several cavities is that we need to fill each cavity with a mixture with different dielectric properties. These cavities will be filled with mixtures that are prepared before mimicking the dielectric properties of different sections of head like brain, CSF, and muscle.



Figure 2.24: Head phantoms including on Right: two cavities and on left: three cavities with a circumvolution's brain.

By using Blender software, a pair of cylinders are added to some cavities. One can fill them and as it is shown in figure 2.25 put any object inside the brain for testing different microwave imaging systems and imaging algorithms in a differential mode, according to the time evolution of the stroke. The brain is cut in two slices then inside of it is reachable to be cleaned after each

experiment and the position of the stroke can be easily fixed. Each part is designed as Lego so after putting two parts of the brain together there will be no evidence of leakage.



Figure 2.25: A sphere located in the head phantom as a stroke.

#### **2.4.1.3 TMM recipes and dielectric properties for head phantom**

By following the process shown in the diagram of preparation of the mixtures (figure 2.13), the concentrations of TX-100 and saline water for different tissues used in the head phantom are obtained. After 3D printing the cavities of the head phantom, each cavity is filled with the appropriate Triton-X salted water liquid.

Table 2.2 displays the results obtained for the head TMMs at 1 GHz. The comparison between the measured dielectric properties of the each mixture and the values given by Cole-Cole model assures us that the mixtures are mimicking the dielectric properties of the target tissue. The brain in this study is considered as a blend of white and grey matters (75% of white matter and 25% of grey matter).

Table 2.2: Concentration values and properties of head TMMs at 1 GHz and 37 °C versus the values inferred from Cole–Cole models [Joachimowicz *et al.*, 2018].

mixture composition			averaged measurements		Cole-Cole	
Tissue	TX-100 (vol %)	NaCl (g/L)	$\epsilon_r$	$\sigma$ (S/m)	$\epsilon_r$	$\sigma$ (S/m)
Brain	38	5.2	44±1	0.84±0.02	42	1.0
CSF	6	13.7	70±4	2.7±0.2	68	2.5
Muscle	24	5	54±1	0.97±0.02	55	1.0
Blood	14	9.6	61±2	1.72±0.05	61	1.6

#### 2.4.1.4 Alternative material for 3D printing cavities

[McDermott *et al.*, 2017] proposes an alternative for phantoms made of ABS. In this article a novel, anatomically realistic, multi-layered head phantom made from dielectrically accurate, stable, low-cost tissue-mimicking materials for testing of microwave diagnostic systems. They proposed to use carbon black, graphite, and rubber to make this new phantom. Tissue-mimicking materials composed of graphite, carbon black, and polyurethane with small volumes of acetone or isopropanol were fabricated and dielectric properties were measured across the [1 – 8.5] GHz band. The concentration of components of the tissue mimicking material properties were adjusted until their dielectric properties matched those of reference values for target tissues of interest.

Since mixing these ingredients are not an easy task and it is almost impossible to have a homogenous mixture then here we propose to use this technique for small strokes inside the head. C-black phantoms do not interact with TX-100. Next step the protocol to make C-black phantoms are described.





Figure 2.26: Photograph of the fabricated dielectrically and anatomically realistic C-black head phantom [McDermott *et al.*, 2017].

First, we start to weigh C black and Graphite separately. Rubber is included of two different mixtures and need to be mixed to have the polymer. After mixing the right amount of ingredients, we will add C black and Graphite slowly to have a homogeneous mixture. Ideally, we would like to avoid air bubbles inside the mixture. At a point that the mixture is solid and there is no chance mix any more powder, we will start adding isopropanol gradually. This increases the conductivity of our solution and at the end, our material will be a bit more fragile compared with the case that we do not use these ethanol.

Next step is to put the solution in a mold. Before pouring it its preferred spraying inside the mold, which helps the material not to stick to the mold. In the end after taking out the C-black phantom from the mold, have to sand it to have smooth surface for checking the dielectric properties of the phantom. Due to the fact that this phantom was made by hand and it is not a perfect homogeneous material it is normal to have different results during changing the probe location.



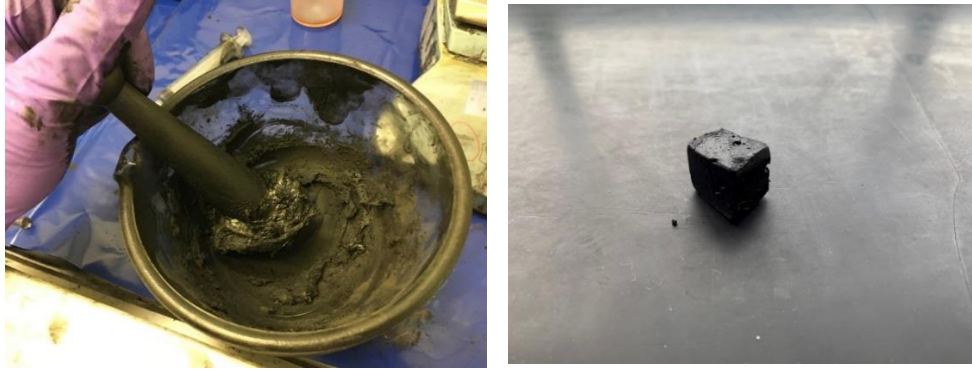


Figure 2.27: C-black phantom made in National University of Ireland Galway (NUIG).

Keysight VNA (E5063A) has an option for multi measurements over on point during a few minutes. In this way, one can check the stability of the measurements. If it is not stable, you might use paper sand to make surface smooth. In addition, it is important to consider the tension on the surface, which is caused by the probe then over time we can find out different dielectric properties. The other point that is important during the measurements is to be sure not to bend the probe. Some times for putting the probe inside a tissue or material we unintentionally bend it slightly, which can cause decalibration of the probe.

#### **2.4.2 Axillary Phantom designed for FCUL microwave imaging system**

Breast cancer is the most frequently diagnosed and cause of cancer death among women [Bray *et al.*, 2018]. Metastases (i.e., cancer's spread to secondary locations) are the leading cause of death for patients suffering from breast cancer. Seventy-five percent of the lymph from the breast drains into Axillary Lymph Nodes (ALNs), making them vulnerable area to breast metastases. The microwave imaging system developed by our partners at Faculty of Sciences of the University of Lisbon, as other MWI systems, needs to be tested by an anthropomorphic phantom before any clinical trial.

### 2.4.2.1 FCUL system

This is a new MWI system designed to be a complementary screening modality helping breast cancer staging by detecting axillary lymph nodes [Godinho *et al.*, 2021]. An ultra-wide band low power radar pulses in a monostatic configuration is used. Beside the VNA, a single Vivaldi antenna with working frequency of [2-5] GHz is implemented in the system. This single antenna covers a cylindrical area since it is attached to an angular positioner (figure 2.28).

To make the axillary region more accessible, the patient would be asked to be in the position indicated in Figure 2.28. The antennas should cover the area in a way that receivers get access to enough information for reconstruction of the image. The proposed positioning of the patient has a direct impact on the phantom development and the axillary phantom is designed based on a CT scan with the same gesture from the patient [Savazzi *et al.*, 2020].

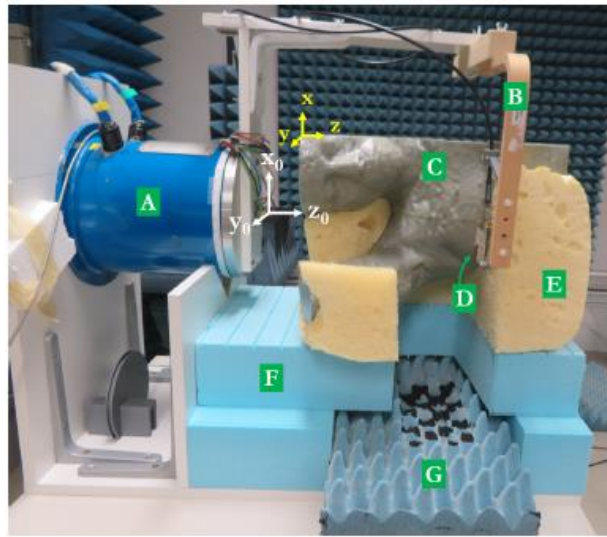


Figure 2.28: Measurement setup (a) with all components (roll positioner [A], antenna support arm [B], phantom [C] and the antenna [D]). The yellow and blue pieces [E, F] supporting the phantom are Styrofoam. The blue piece at the bottom [G] is an Eccosorb CV type microwave absorber, which is used for testing purposes to minimize the table's reflection [Godinho *et al.*, 2021].

#### 2.4.2.2 Thorax cavities

The microwave imaging system developed by Faculty of Sciences of the University of Lisbon needs to be tested on an anthropomorphic phantom before any clinical trial. First version of thorax cavities is developed based on a thoracic CT of a patient diagnosed with breast cancer and was undergoing treatment at the Champalimaud Foundation [*Fundação Champalimaud*, online].

Using the segmented models, including skin, muscles, lung, bones and lymph nodes, we created printable 3D models and exported them as STL files. Importing these data in a 3D printer, our axillary phantom can be inserted into the setup. In this phantom (Figure 2.29), there is a thin layer of plastic, which defines the shape of the body and encompasses the rest of the cavities. The lung cavity is fixed inside the skin cavity and can be filled through two cylinders attached to it. The bone part, which represents the scapula and humerus (upper arm), is made of ABS. Fat cavity is between the outer layer and muscle cavity and have lymph nodes inside of it. Lymph nodes are elliptical cavities with different sizes. Difference in size represents anomaly. These elliptical cavities are connected by a plastic pipe in order to be filled.

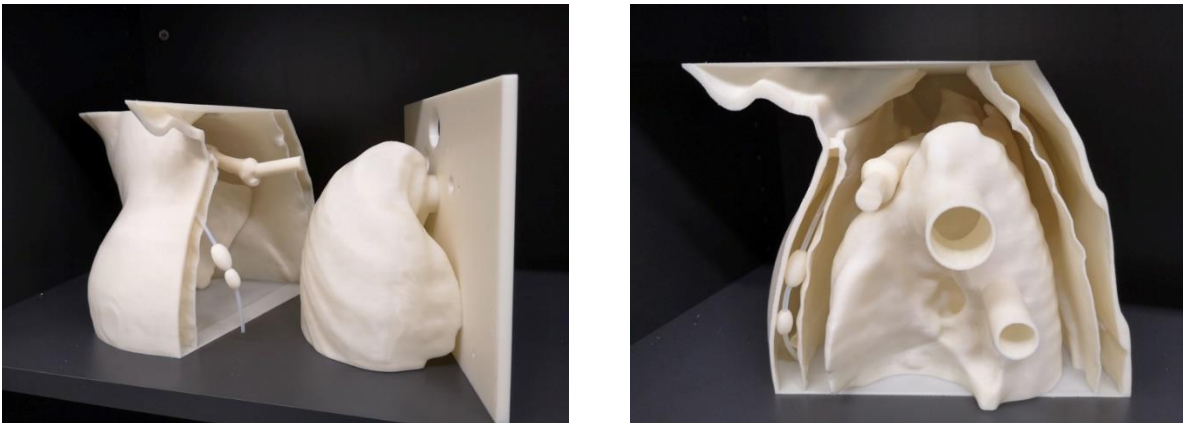


Figure 2.29: 3D printed axillary phantom. This phantom includes an outer shell with the shape of skin, fat cavity below the skin, lymph nodes embedded inside the fat cavity, and lung cavity and shoulder bone fixed in the muscle cavity.

As mentioned in previous sections, it is also possible to use online phantom library in which you have access to different 3D models related to the anatomy of human body. For instance to have the second version of axillary phantom we had to choose couple of lymph nodes and cut the part of the shoulder which is the area of interest for us. From the prepared 3D model of the human body available online, the second version of thorax cavities has been designed. We considered only scapula and humerus and lung, so we had to get rid of the rest of the organs exist in the phantom obtained from the library. We used Blender to do all these adjustments and in the end by adding cylinders to the lung cavity, we will be able to 3D print and fill it with TMMs. Inside the bigger cavity there are some spots to fix the bone and lung cavity. In this way, the system will be more stable and resistance toward movements.



Figure 2.30: 3D printed axillary phantom based on online phantom library.

#### **2.4.2.3 TMM recipes for axillary phantom**

To fill cavities of the axillary phantom introduced in section 2.4.2.2 with TMMs, the concentrations of TX-100 and salt are calculated using the optimization code. Based on the protocols explained in section 2.2.2 the mixtures are produced and measured. Muscle, fat, lung and lymph node are four mixtures provided for the axillary phantom (Table 2.3) for the frequency range of [1-8] GHz.

Table 2.3: Concentration values and properties of axillary phantom TMMs for frequency band of 1 GHz to 8 GHz [Savazzi *et al.*, 2020].

Tissue	mixture composition	
	TX-100 (vol %)	NaCl (g/L)
Muscle	26.5	7.4
Lung	55	4.51
Fat	100	0
ALN	25	8.59

### 2.4.3 Liver Phantom designed for CNR-IREA system

Liver cancer is a major health problem by being ranked fifth in men and eighth in women among all cancer diseases [Bosch *et al.*, 1999]. This fatal health issue is increasing yearly despite the advanced technologies. Over the last decades, thermal ablation techniques are developed as an alternative to surgical approaches. In fact, Microwave thermal ablation (MTA) is a cancer treatment targeting focal malignancies, in which a zone in tissue is targeted by high temperatures at microwave (MW) frequencies (typically 915 MHz or 2.45 GHz) [Lopresto *et al.*, 2018].

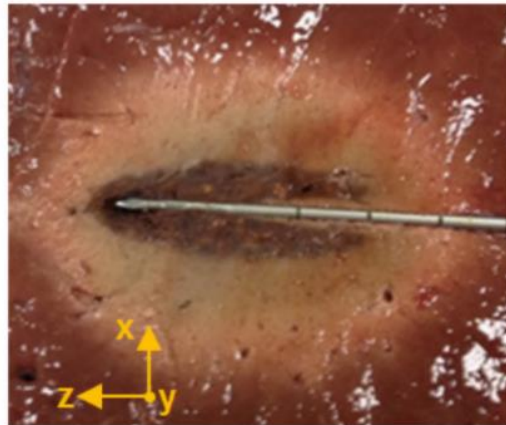


Figure 2.31: Schematic representation of the zone of ablation from the MTA procedure. The central (dark) area is the carbonized tissue, surrounded by the area of (white) coagulated tissue; externally is the (red) untreated tissue [Lopresto *et al.*, 2018].

Our partners at IREA-CNR in Naples are developing a microwave imaging system for continuous monitoring of liver tumor ablation.

#### **2.4.3.1 CNR-IREA system**

MWI system developed at IREA in Naples is shown in figure 2.32. The set-up includes of a tank made of ABS material filled with a coupling medium which was designed in a way to maximize the electromagnetic power delivered to the liver [Wang *et al.*, 2022]. An ellipsoidal phantom representing the liver tissue after the ablation treatment is located inside the tank. The phantom is a 3D-printed structure made of ABS material and filled with Triton-X-100/water mixture as tissue-mimicking material. A slot-loaded Vivaldi antenna which was designed specifically for this MWI system is placed 35mm away from the phantom, moving in a linear direction measuring the scattering parameters [Wang *et al.*, 2022].

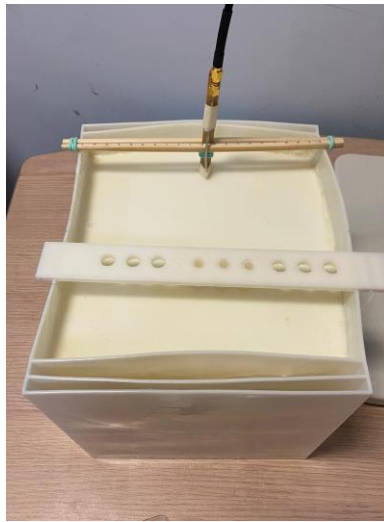


Figure 2.32: MWI system for liver ablation.

#### **2.4.3.2 Liver cavities**

The phantom should represent different sections of the ablated area as indicated. After agreeing on the size of the phantom, a tank made of ABS with different layers representing skin, fat and

liver is designed. The size of this container is  $21 \times 24 \times 21 \text{ cm}^3$ . These dimensions are set based on the size of the microwave imaging system designed in IREA and the limitation of the 3D printer at GeePs.

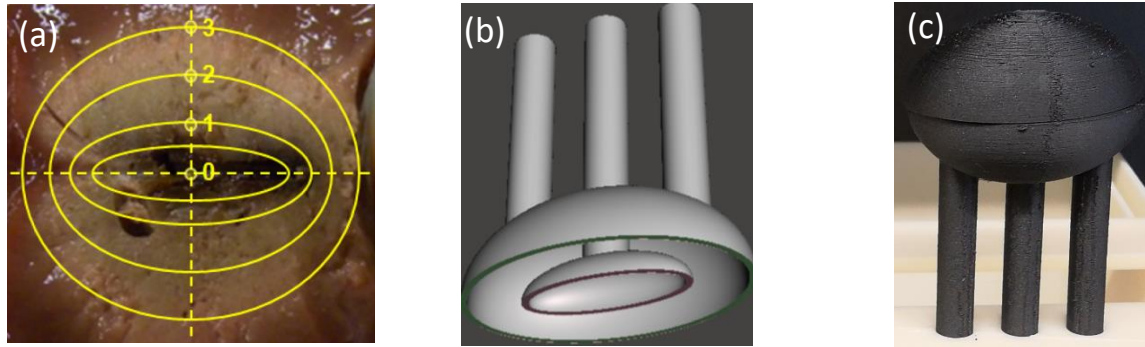


Figure 2.33: Elliptical phantom representing ablated tissues. (a) Different zones of ablated tissue [Lopresto *et al*, 2012], (b) CAD model, (c) PA printed cavities.

Inside the liver cavity, there is an ellipsoidal phantom mimicking the ablated Region. In a study the ablated part of the liver is divided to 4 zones [Lopresto *et al*, 2012]. After ablation process, those zones with similar tissue damage are considered as one zone. The tip of the antenna is at the center of zone zero (figure 2.33a). For the sake of simplification of the phantom and avoiding using several cavities in a small space, the ablation part of the phantom is designed as it is shown in figure 2.33b,c. mixtures mimicking zone zero will be poured in the inner cavity and the rest will be for zone 1 or 3. Based on the dielectric properties of zone two, the concentration of TritonX-100 will be in such a way that the solution will be gel. To avoid this, zone two is not considered. Thus, ablation phantom has two cavities representing carbonized and coagulated tissue.



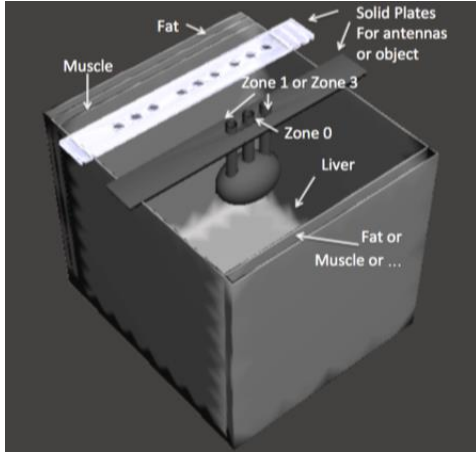


Figure 2.34: First prototype of a multilayer abdomen with the ablated liver cavity

The ablated phantom is hanging from a plate fixed on the top side of the tank. This plate has several holes on it. This gives us the chance to move the elliptical phantom and perform the experiments with different position of the antennas with respect to the phantom.

#### 2.4.3.3 TMM recipes and dielectric properties for liver phantom

Dielectric characterization of liver, muscle, and ablated part for this phantom are provided to us by ESR13, who is working on design and realization of a device for non-invasive monitoring of ablation treatments. The recipes of three zone out of four zones are going to be provided. Indeed as previously mentioned, zone two's mixture is going to be gel at room temperature since the TX-100 concentration is in the range of 40-55 %, which makes the solution gel. Thus, this zone is not taken into account. Values given in [Lopresto *et al*, 2012] at 2.45 GHz is used as the input of the optimization code and the extrapolation is done on the range of [1-3.5] GHz. Table 2.4 shows the recipes of different TMMs for liver phantom that contained an ablated part (Z1 or Z3) and a carbonized part (Z0) at 2.45 GHz in the room temperature.



Table 2.4 Concentration values and properties of live phantom TMMs at 2.45 GHz.

Tissue	mixture composition		averaged		Reference	
			measurements			
	TX-100 (vol %)	NaCl (g/L)	$\epsilon_r$	$\sigma$ (S/m)	$\epsilon_r$	$\sigma$ (S/m)
Zone 0	88	4.5	8.3	0.4	8.33*	0.39*
Zone 1	60	9	21.6	1.1	21.57*	1.14*
Zone 3	37	8.5	37.2	1.6	37.24*	1.6*
Liver	31	5	43.5	1.6	43	1.68
Muscle	24	5	52	0.2	52.7	0.24

\*From [Lopresto *et al.*, 2012]

## 2.5 Conclusion

This chapter addressed the tools to produce anthropomorphic phantoms for numerical and experimental validation of microwave imaging systems. To set up a MW imaging system, several simulations need to be done before building up the system in the lab. Having a numerical version of human body is essential for these simulations. Moreover, after setting up the imaging system many tests are needed to analyze the performance of the system and feasibility of it. These tests cannot be done on a human, which is why a 3D printed human phantom with dielectric properties of target tissues is desirable.

After reviewing different types of phantoms in the literature, in this chapter liquid phantoms are proposed as anthropomorphic phantoms including 3D printed cavities filled with tissue mimicking materials (a mixture of TX-100 and salted water in this case). For production of TMMs, knowledge of relaxation models, dielectric characterization techniques, fluid mixture laws and some practical protocols is essential which is explained in section 2.3. The other important part of

this chapter is modeling and printing 3D cavities. In section 2.3.2, general tools for creating STL files of the human body from MRI and CT scan of the organ are given. These tools give the designer the opportunity to segment the target organ and then modify it. In the end, a 3D model of the organ can be exported as a STL file. To elaborate on it, several cases are studied as examples. The numerical files of different head, axillary and liver phantoms are prepared and used for 3D printing of these phantoms as shown in section 2.4. Numerical versions of these phantoms will be used in the next chapter for studying the behavior of the phantoms in the microwave imaging systems by simulations. Moreover, these numerical versions are used to obtain 3D printed phantoms. These 3D printed phantoms will be sent to our partners in the other countries since they are compatible to MW imaging systems developed in POLITO (Italy), FCUL (Portugal) and IREA (Italy).

### **3 E-Field simulation of 3D anthropomorphic phantoms**

#### **3.1 Introduction**

Several research groups have already introduced phantoms consisting of plastic cavities filled with liquid mixtures into their microwave imaging systems. For instance the GeePs-L2S breast phantom which has been developed by our group has been used by [Meaney *et al.*, 2016; Casu *et al.*, 2017; Koutsoupidou *et al.*, 2017; Felício *et al.*, 2019], as part of the TD1301 cost action (2014-2017) for simulations and experiments. In this chapter, we propose a simulation-based technique to analyze the characteristics of designed the anthropomorphic phantoms developed in the previous chapter. The simulations are done using two commercial EM simulators CST and WIPL-D. In the first step, STL files of the phantoms are imported into these EM solvers. In this way, the shape and the dimensions of the cases studies in simulations are the same as the 3D printed phantoms, used in different experimental configurations. This gives us the opportunity to have a proper cross validation between simulated and experimental results, as for instance is presented in [Rodriguez-Duarte *et al.*, 2021]. In this chapter after a brief description of the methods used by CST and WIPL-D to solve EM problems, several simulations on different phantoms with the purpose of understanding the effect of parameters of the phantom are carried out. Simulation configuration on the head is based on the microwave imaging system designed at POLITO [Tobon Vasquez *et al.*, 2020] while the ones on the axillary phantom are related to the system which is developing at FCUL [Savazzi *et al.*, 2020]. The results of these simulations can be used as the reference for future experiments in different laboratories.

##### **3.1.1 The Finite Integration Technique (FIT) and Method of Moment (MOM)**

The transient high frequency solver inside CST is based on the Finite Integration Technique (FIT), first proposed by [Weiland, 1977]. This method describes Maxwell's equations on a grid

space and makes handling large radiating structures and even complete arrays with more than some hundreds of radiating elements possible. This represents a significant performance advantage compared to non-time domain methods, which entail the simulation of a large number of discrete frequencies for broadband data extraction.

FIT discretizes the following integral form of Maxwell's equations rather than the differential one:

$$\oint_{\partial A} \vec{E} \cdot d\vec{s} = - \iint_A \frac{\partial \vec{B}}{\partial t} \cdot d\vec{A}, \quad \oint_{\partial A} \vec{H} \cdot d\vec{s} = \iint_A \left( \frac{\partial \vec{D}}{\partial t} + \vec{J} \right) \cdot d\vec{A} \quad (3.1, 3.2)$$

$$\iint_{\partial V} \left( \frac{\partial \vec{D}}{\partial t} + \vec{J} \right) \cdot d\vec{A} = 0, \quad \iint_{\partial V} \vec{B} \cdot d\vec{A} = 0 \quad (3.3, 3.4)$$

To solve these equations numerically, you must define a finite calculation domain, enclosing the considered application problem. Creating a suitable mesh system splits this domain up into many small elements or volume grid cells.

On the other hand, the EM modeling software WIPL-D Pro is based on a Method of Moments (MoM) solution of the Surface Integral Equations employing higher-order basis functions and a quadrilateral mesh. Flexible modeling of an arbitrary electromagnetic 3D structure is based on Wires and PLates, the property that has been highlighted in the very name of the program code (WIPL). Right truncated cones are used to approximate the wires, and plates are used to approximate flat or curved surfaces. Plates, also called quads, are actually the bilinear surfaces determined by four points arbitrarily located in space [WIPL-D, online].

An unknown current along a wire is approximated by single polynomial expansion, while a current over a plate is approximated using double polynomial expansion. Higher Order Basis Functions (HOBFs) satisfying the continuity of currents are used to approximate the currents on a mesh element. A large structure can be adequately modeled using approximately an order of magnitude fewer unknown coefficients compared with other MoM codes, which use triangular

meshing and Rao-Wilton-Glisson (RWG) basis functions. “Unknown” is an unknown coefficient in the approximation of the current [WIPL-D, online].

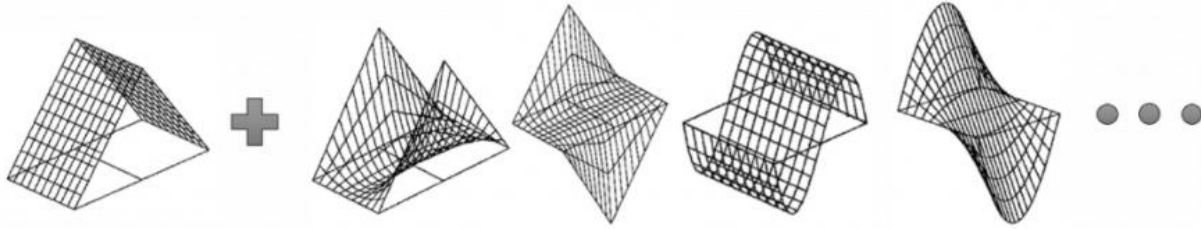


Figure 3.1: Different orders of basis function [WIPL-D, online].

To define unknown coefficients of the basis function, a system of linear equations is obtained by applying Galerkin testing procedure. The more complex the problem, the more coefficient (N) are required for a good approximation, and more unknown functions need to be determined. The final step in the resolution of the problem is the inversion of a  $N \times N$  matrix [WIPL-D, online].

### 3.1.2 Accuracy of FIT and MOM

To compare the accuracy of the numerical methods used in CST and WIPL-D, a study is conducted here to analyze the interaction of a plane wave and a simple object. In order to define a configuration close to our cases of interest (dielectric media), we have chosen a dielectric plate of low thickness (0.5 cm) and high permittivity. Knowing that In CST by increasing the number of meshes and in WIPL-D by increasing the order of the used basis function higher accuracy in results can be achieved, the study focuses on these two parameters. For a same scenario, the convergence of outcomes of CST and WIPL-D in high accurate simulation configuration is expected.

### 3.1.3 Rectangular plate

Consider a rectangular cube with dimensions of 0.5 cm x 4 cm x 6 cm (x,y,z) ( $\lambda_0 = 1\text{ m}$ ) with dielectric properties of  $\epsilon_r=70$  and  $\sigma=1\text{ S/m}$ . The plate is illuminated by a plane wave propagating along axis z at 300 MHz. The electric field is linearly polarized along x-axis.

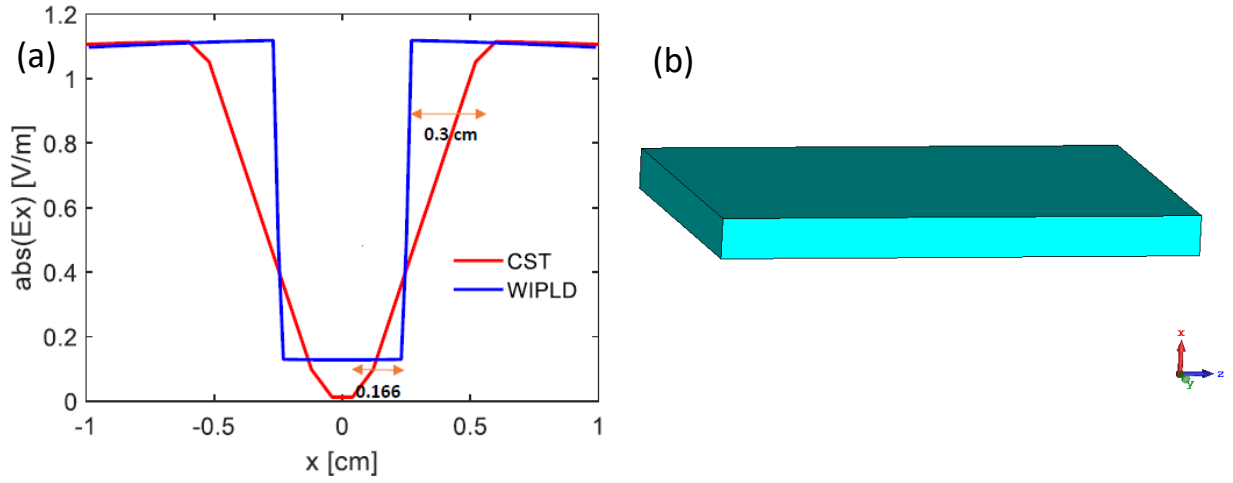


Figure 3.2: (a) Field module of  $E_x$  for CST and WIPL-D. The representations of the plate created in (b) CST.

For the CST simulator, the automatic meshing results in a mesh size of 0.166 cm inside the plate corresponding to  $0.013\lambda_d$  ( $\lambda_d = \lambda_0/8.3$ ). The size of the mesh outside the brick is 0.3 cm that is  $0.003\lambda_0$ . In WIPL-D, the size of the mesh on each side is the dimension of the plate since the software uses low number of meshes and high order of base function. The basis function is set automatically so that in next steps it is possible to increase it for more accuracy. Based on this, regarding to the figure 3.2, one can see the module of the Electric field around the edges of the plate in CST gradually changes but it is an abrupt change at the edges of the plate for WIPL-D. The slow change obtained with CST is related to the size of the mesh around the edges, thus by increasing the number of the meshes close to the edges the slope of the variation of the electric field will be increased approaching the solution given by WIPL-D.

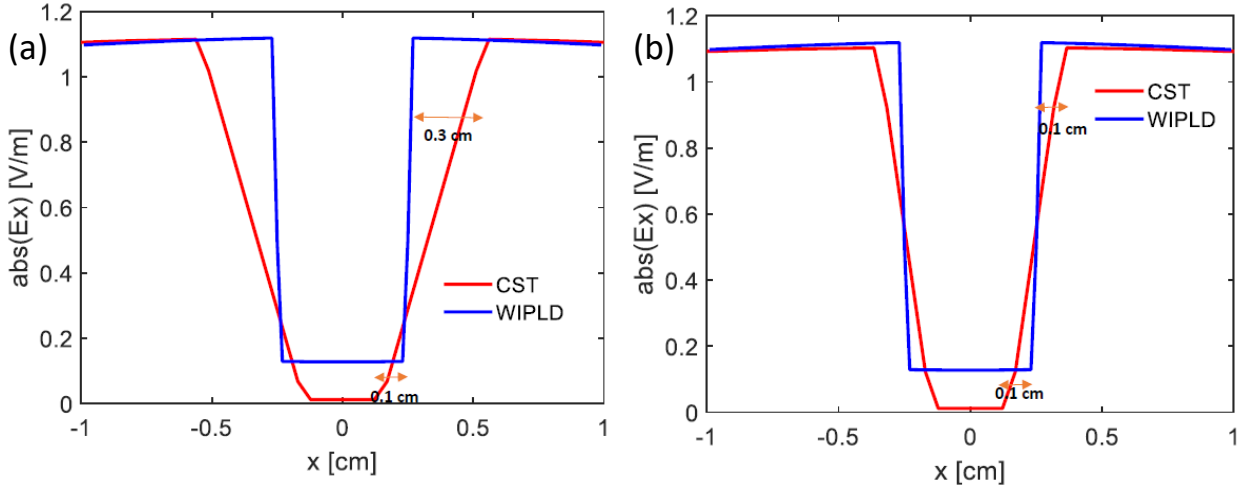


Figure 3.3: Decreasing the number of meshes (a) inside the plate from 0.16cm to 0.1cm and (b) outside the plate from 0.3cm to 0.1cm.

In the figure 3.3, you can see that when the meshes inside and outside the plate is decreased to the size of 0.1 cm, the results are getting closer to WIPL-D outcome. On the other hand, the accuracy of the level of electric field inside the plate is not improved by changing the mesh sizes.

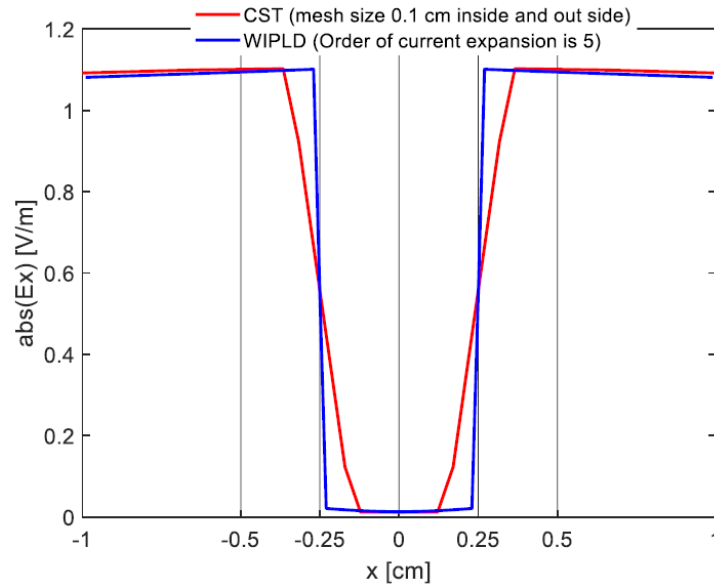


Figure 3.4: Comparison of the outcome of CST with mesh size of 0.1 cm and WIPL-D with order of current expansion of five.

By increasing the number of meshes in CST and the order of current expansion in WIPL-D, it can be seen, on one hand, that the number of meshes in CST directly has effects on the module of E-field on the borders of the object. On the other hand, by increasing the order of basis functions

in WIPL-D, the module of the E-field inside the object will change and convergence to the solution obtained with CST.

As a conclusion, the calculation of the field in CST and WIPL-D is sensitive to a precise description of contours (mesh steps on borders of the object) and order of the basis function, respectively. In this section, it is proven that by increasing the accuracy of simulations in CST and WIPL-D, a cross validation of obtained results is possible.

### **3.2 Importing STL files into an EM solver**

According to what mentioned before, to simulate the interaction of an electromagnetic source with a part of the human body, we must have a 3D model that allows us to describe the geometry of the body as closely as possible.

To create simple models, there are various tools in simulators such as CST and WIPL-D. On the other hand, more complex shapes need to be prepared in advance using 3D computer graphics software (e.g. Blender) and then imported into the EM solver. As explained in the previous chapter we are interested in using STL files because they can be used also for 3D printing and running simulation. In chapter 2, the process of preparing 3D phantoms using MRI or CT scans was explained and several examples were shown. To use the 3D models of the human body in the simulations it is needed to import the STL files of these models into the EM simulator. Most of the EM solvers have the option of importing STL files. Since these files contain information about the shape and the location of the model then different simulations in various simulators with the exact same condition can be done.

After importing the STL file into the software (figure 3.5a), we need to add the information about the dielectric properties of each part of the model by selecting each section and setting the right



values for each domain (figure 3.5b). The rest of this chapter is dedicated to results of various numerical simulations on different phantoms.

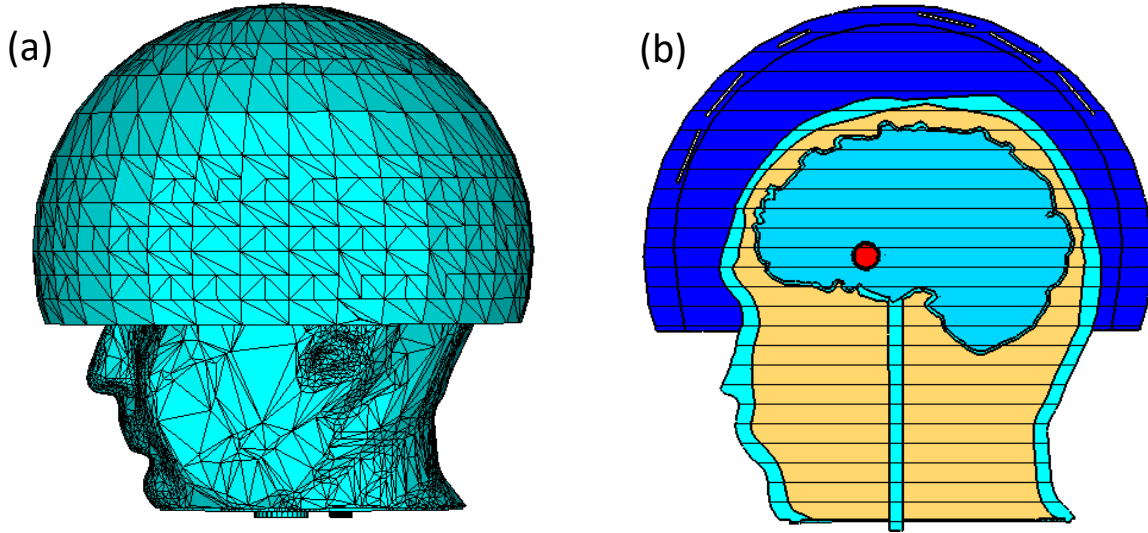


Figure 3.5: Representation of (a) imported STL files of a head phantom and a helmet, (b) the defined dielectric domains for each cavity at CST.

### 3.3 Numerical simulations on head phantoms

Having the STL format files of the head ready, we are capable of importing these files to CST microwave studio. Using this simulator, we can analyze different scenarios to see for which antennas configuration is more adapted to localize and detect abnormal tissues as for example ischemic or hemorrhagic strokes in the head. By EM simulations, it is possible to analyze the influence of the different parameter used for the phantom and microwave imaging system design. Since we are working in the platform of EMERALD project, the configuration of the microwave imaging system, developed by [Rodriguez-Duarte *et al.*, 2021] is used here. STL files of the head phantom include some cavities, which are made of ABS. Thus, in simulations we define the dielectric properties of cavity shells as the dielectric properties of plastic (whose relative permittivity and conductivity are 3 and 0.004 S/m, respectively at 1 GHz). In this configuration, head phantom is covered by a conformal helmet made of TX-100 with relative permittivity and

conductivity of 23 and 0.3 S/m, respectively at 1 GHz, according to [Rodriguez-Duarte *et al.*, 2020]. Moreover, 24 implemented monopole antennas are included in the helmet. Further details on the choice of the antenna array (arrangement and number of antennas, the working frequency and the matching medium), as well as on the brick-shaped antenna module used in the POLITO imaging system are given in [Scapaticci *et al.*, 2018] and [Rodriguez-Duarte *et al.*, 2020] respectively.

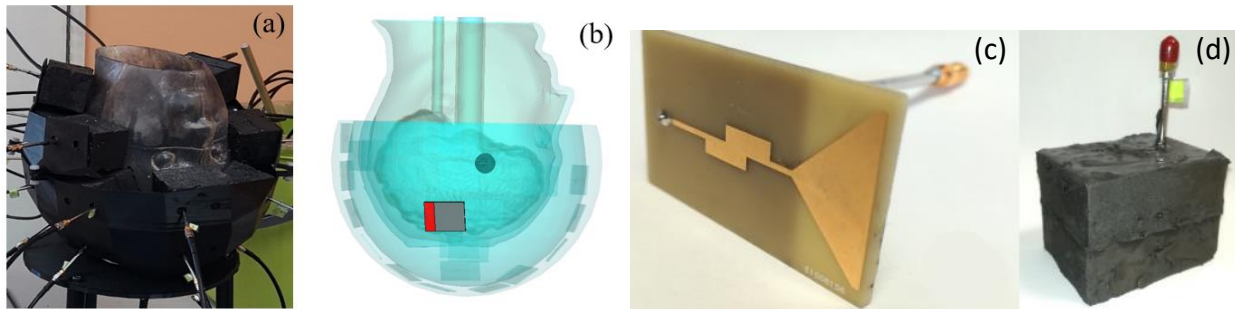


Figure 3.6: The imaging system, including a head phantom with a stroke mimicking anomaly and a 24-antennas array conformal to the head (a,b); (c) monopole antenna printed on FR4 substrate; (d): monopole antenna embedded into the brick [Rodriguez-Duarte *et al.*, 2020].

There are different parameters of the phantom that must be studied before any real experiment. For instance, the idea of having several separated cavities inside the head representing different tissues needs to be proved. Moreover, the effect of coupling medium, plastic shell and considering vessels in the brain on the E-field distribution inside the head is going to be studied.

Validation of feasibility of using these types of phantoms in a microwave imaging system is essential. It is needed to be sure if the phantom interaction with E-field helps with not only defining the shape and location of abnormal tissues but also tracking the changes in dielectric properties of tissues. In this section, studying the magnitude variation of E-field inside the head is proposed. In order to localize a tissue change, a differential field technique is used. By subtracting the electric field obtained inside the head in the absence of the stroke-affected tissue from the one obtained in its presence, we will achieve the differential E-field inside the head. The purpose is to obtain a

final figure that shows the effect of the presence of abnormal tissues. The influence of variation of parameters such as the coupling medium and the printed material (ABS) on the E-field distribution is more tangible by applying this method.

Simulations are done while only one of the 24 antennas (the one shown in red in Figure 3.6b) is active. Some of the presented results from CST simulations are normalized as follows:

$$\text{Normalized Module} = (\text{Module} - C_{min}) / (C_{max} - C_{min}) \quad (3.5)$$

where Module is the magnitude of total E field (the three components),  $C_{max}$  and  $C_{min}$  are the max and min values. The range of the color bar used to display the normalized electric field distribution is given in dB between  $-10$  to  $-40$  dB while the differential field distribution is presented in V/m.

### 3.3.1 Effect of coupling medium

The existence of coupling medium in this microwave imaging system is justified by not only the enhancement of EM field penetration in the head but also the easiness positioning of the antennas. The influence of variation of dielectric properties of the coupling medium is studied when one of the 24 antennas is active. The magnitude of the electromagnetic field distribution inside the phantom for two different coupling mediums (figure 3.7) indicates that by using TX-100/salted water as coupling media with a dielectric constant of around 20 at 1 GHz, as it has been suggested in [Tobon Vasquez et al., 2019], the Electric field penetrates better into the head. In the other words, the module of the electric field is higher by using TX-100/salted water than when using air as coupling medium. Choosing a proper coupling medium is particularly important here, due to the high attenuation of different layers of the head, a good coupling medium helps to have a clear image of the stroke despite of this higher attenuation.

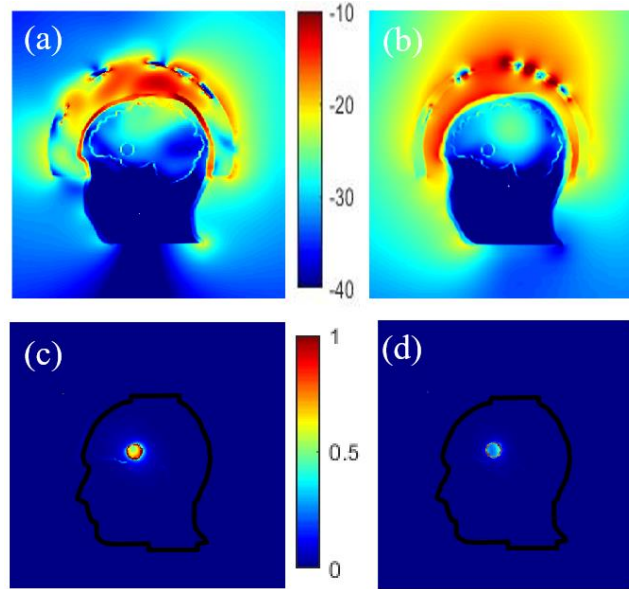


Figure 3.7: Normalized electric field magnitude distributions inside and outside the head for two different coupling mediums, (a) TX-100/salted water and (b) air. The corresponding differential field distributions, TX-100/salted water (c) and air (d) respectively.

### 3.3.2 Effect of Phantom Complexity

Head is the most complex part of human body. Hence, to design an anthropomorphic head phantom we need to consider this complexity (see figure 3.8). There are numerous types of tissues in different locations inside the head. To improve the design of our anthropomorphic head phantoms, we need to know if it is possible to dedicate a cavity to each tissue type. Moreover, the existence of blood vessels and blood flow is one of the other complexity, which needs to be taken care of. In this section, we are going to improve the design of the head phantom to reach a more complex one and will study the effect of these changes.

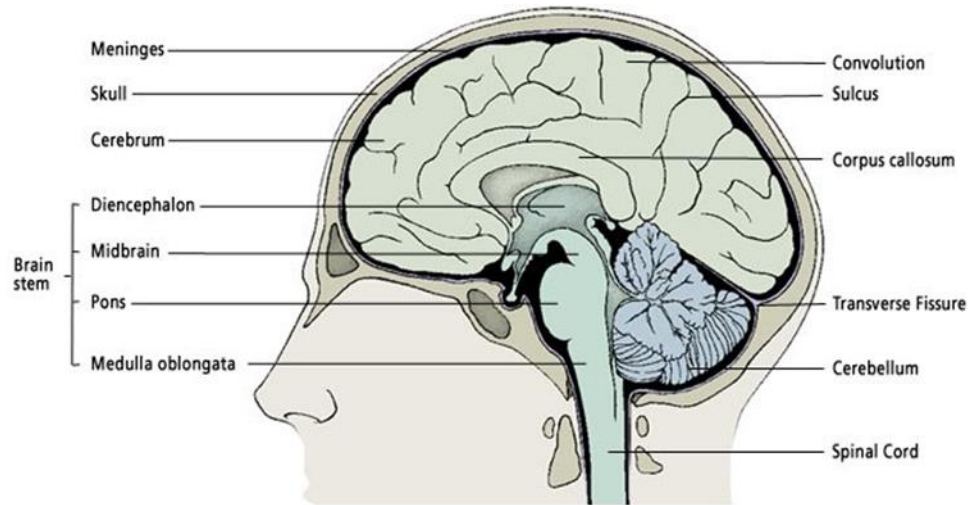


Figure 3.8: Complexity of human head. Head is a complex structured organ and it is needed to consider different tissues inside of it to be able to present a decent head model [brain anatomy, online].

### 3.3.2.1 Number of cavities

More realistic phantoms can be achieved by taking into account different parts of the brain or other tissues such as skin, muscle, and skull and designing additional cavities for them. Thus, before the experiments, the validity of the phantom can be evaluated numerically by studying the effects of adding new cavities in the simulations. Here, an additional cavity in the lower part of the head, filled with a mimicking mixture for muscle tissues (whose relative permittivity and conductivity are 55 and 1 S/m, respectively at 1 GHz), is considered.

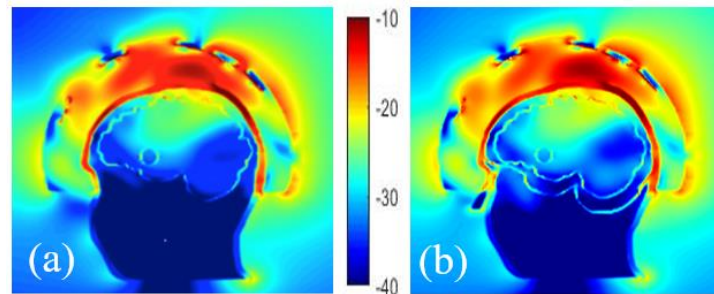


Figure 3.9: Comparison of the normalized E-field distribution inside and outside of head phantoms with a stroke, composed of 2 cavities (a) and 3 cavities (b).

Comparing the E-field distribution of these two cases (figure 3.9), it can be seen that the amplitude of the E-field inside the brain is similar. Due to the experimental configuration

considered (antennas array conformal to the head placed on top of the skull), the dielectric properties of the mixture in the lower part of the head and the extra cavity there seem to have a low effect on the distribution of the electric field in the brain.

### 3.3.2.2 Vessels around a randomly shaped stroke

A more sophisticated numerical head phantom including a brain model that accounts for blood vessels is investigated to check the possibility of recognizing a randomly shaped stroke. The vessels occupy a volume of height and width of 2.6 cm and 1.8 cm, respectively. The dielectric properties of the blood are 61 and 1.6 S/m for relative permittivity and conductivity, respectively at 1 GHz. The simulations are done with and without a plastic shell around the stroke, in the presence of the blood circulation.

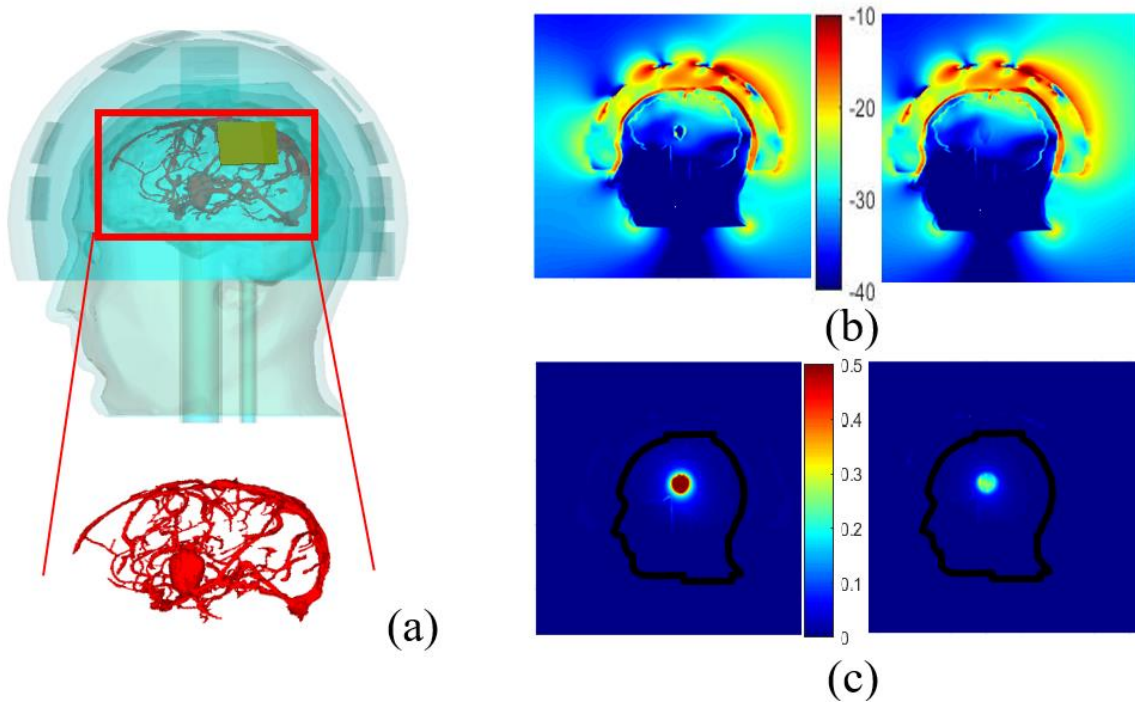


Figure 3.10. Head phantom including brain vessels and an elliptical stroke inside (a). Normalized magnitude of the E- field inside and outside the head by taking blood vessels into account and the elliptical stroke, surrounded by ABS (b, left), with no ABS (b, right); the corresponding differential E-field (c, left) and (c, right) respectively.

This model, including an elliptical stroke inside, is depicted in figure 3.10a, whereas figures 3.10 b,c display the total and differential E-field distributions, in the two different cases: with and without the plastic shell. In figure 3.10 b,c, it appears that the presence of the ABS structure leads to an overestimation of the differential field due to the low dielectric properties of the plastic compared with the TMM around it. Other simulations show that in the given experimental configuration of the system, the vascularization of the brain does not affect the differential distribution of the field, when a stroke is considered. As a result, this quantity  $\Delta E$ , remains a proper quantity to track the status of the stroke over time since the stroke is still visible and well positioned in the middle of the brain for both cases.

### 3.3.3 Effect of the Plastic

In clinical tests, skin and fat are the first layers of human body, exposed to the EM wave while imaging. Plastic is the alternative of skin in our phantoms. However, even though it has a little thickness compare to the wavelength, the difference of the electrical contrast between skin and plastic is high. Moreover, the use of plastic in the GeePs-L2S breast phantom was controversial [Rydholm *et al.*, 2018]. Then, there is a need to study the effect of plastic in the designed head phantom.

Different configurations are simulated to study the effect of plastic on the field distribution depending on its location, i.e., around the stroke, the stroke and the brain, the bone. Therefore, the cavities of phantom including head, brain, and stroke made of ABS are considered. The other scenario is to consider the containers with the same dielectric properties as the tissues. At first sight, using phantoms made of ABS may not seem practical due to the low relative permittivity of ABS but the results depicted in figure 3.11 indicate that removal of ABS does not have a noticeable effect on the E-field distribution inside the brain, except for the skull whose thickness varies from



2 to 8 mm. Thus, an alternative material whose dielectric constant is close to the bone's dielectric constant (around 10 at 1 GHz) should be more suitable to print the head external wall. “3D-Prima Conductive ABS” filament seems to be a good candidate [Faenger *et al.*, 2017].

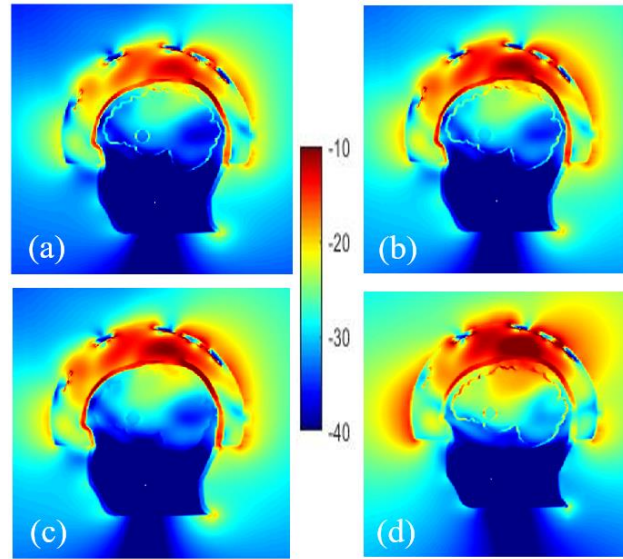


Figure 3.11: Normalized electric field magnitude distribution inside and outside the head including cavities made of: all the ABS shells (a), without ABS for stroke (b), stroke and brain (c) and only bone (d).

### 3.4 Simplification of head phantom

The number of unknowns in WIPL-D software is directly related to the number of the faces we use to build the surfaces representing the profile of the object modeled in the simulation. Normally importing a STL file in WIPL-D will lead to huge number of plates, which is not desirable. To fix this problem we started using different techniques to simplify the STL file of the head that is used for printing and simulating.

In previous chapter, the process of preparing different phantoms for microwave imaging purposes is explained. The numerical version of the head phantom, which is printed already, is imported in CST Microwave Studio for simulations, and also inserted in a setup including 24 antennas in POLITO for some experiments. The software Blender is used to simplify this phantom by decreasing its number of faces in a way that the simulation will be more efficient in WIPL-D.



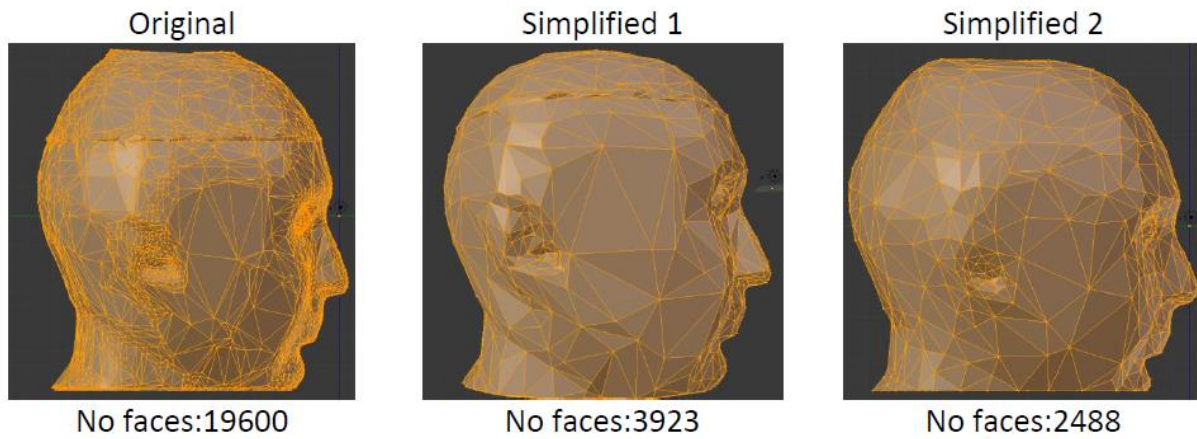


Figure 3.12: Different steps in using Blender to decrease the number of faces of the head phantom from 19 600 to 2 488.

In WIPL-D, after importing the STL file of the phantom we have to re-mesh it and convert the triangle meshes to quadrilateral meshes. The results of this conversion is shown in figure 3.13. Since WIPL-D merges triangles and creates quads, the number of meshes in WIPL-D are relatively lower than in Blender.

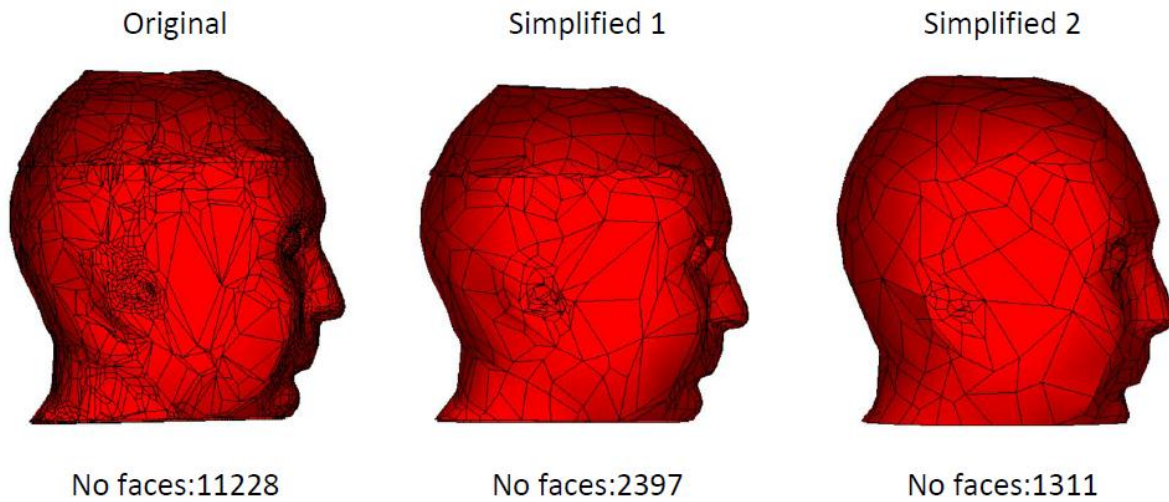


Figure 3.13: Using WIPL-D for re-meshing the head phantom, preparing it for new simulations in WIPL-D.

### 3.4.1 Validation of simplified phantom

To evaluate the effect of this simplification on the variation of the E-field distribution inside the head we considered only the head as a plastic shell. There is vacuum inside and outside of the shell and an incident plane wave at 1 GHz illuminate the phantom.

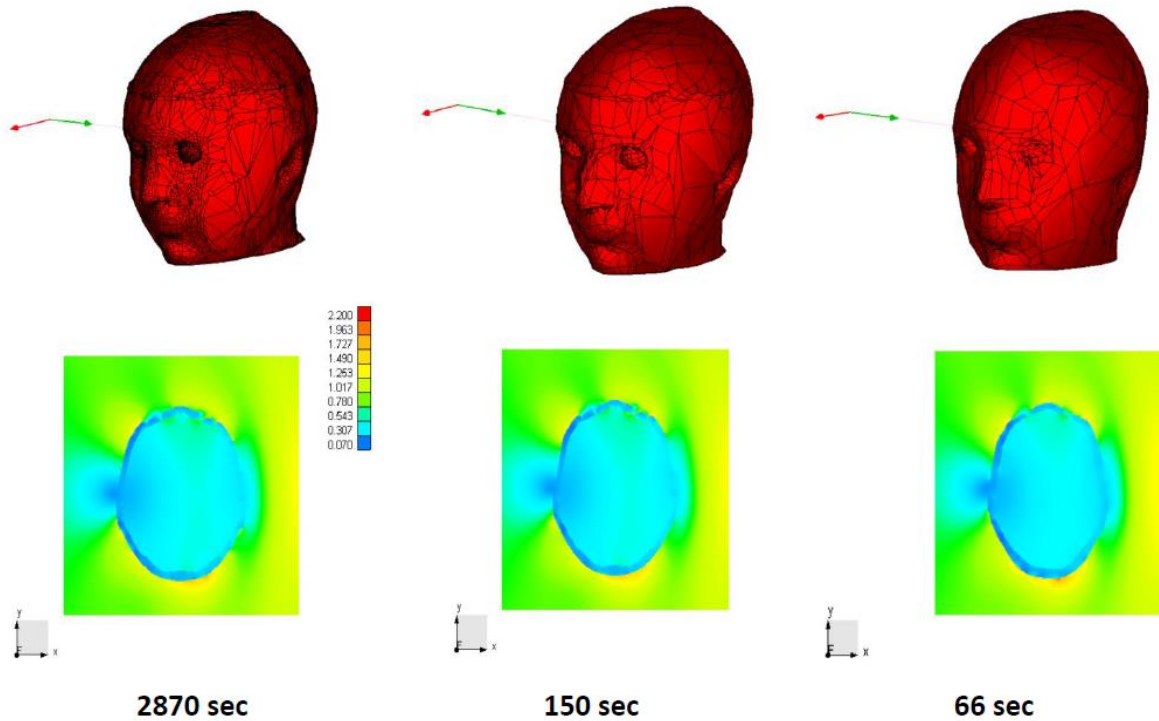


Figure 3.14: Three different phantoms and E-field distribution inside of them with the simulation time on a computer (using a PC with Intel(R) Xeon(R) W-2135 CPU working at 3.70GHz and 128 GB RAM).

Figure 14 shows that the electric field distribution inside the head is almost the same for all three phantoms used in the WIPL-D software. As depicted in figure 3.14, the simplification of the representation of the head phantom leads to less number of faces and unknowns, which means a shorter simulation time for same E-field distribution inside the head. Amongst the designed phantoms, simplified number 2 has the lowest simulation time while the electric field distribution is the same as the ones with dense meshed phantoms.

### 3.4.2 Validation of simulations

In this section, we compare the two different software: WIPL-D and CST. The numerical techniques behind these two EM simulators are explained previously in this chapter in section 3.1. The configuration considered here is the homogenous brain simplified phantom with a sphere stroke inside of it, illuminated by a plane wave at 1GHz. The phantom is composed of a plastic outer shell and homogenous brain inside of it. There is a sphere with dielectric properties of blood inside the brain (the relative permittivities and conductivities of brain and blood are given in figure 3.15). We keep this configuration for the rest of the chapter.

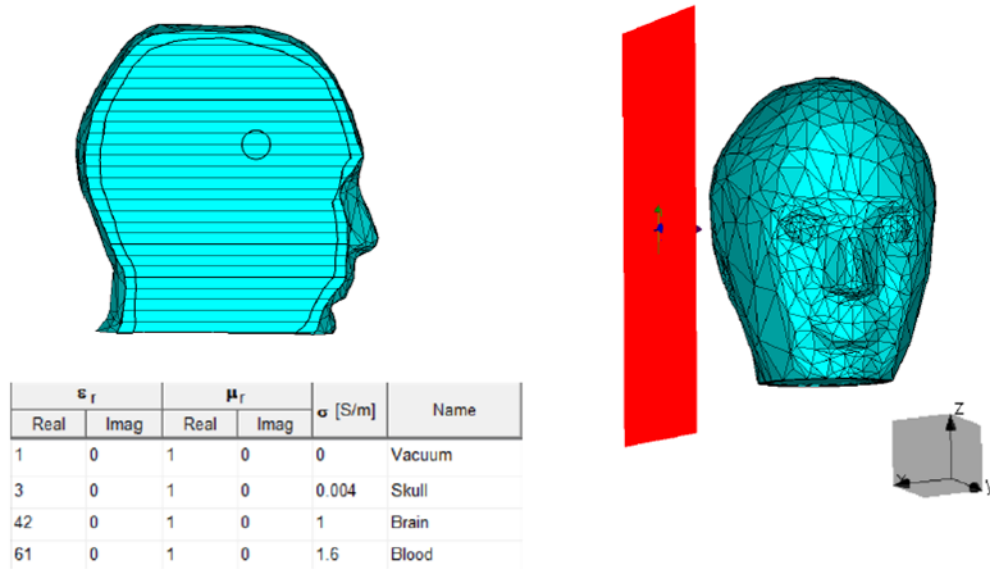


Figure 3.15: The configuration used for simulation validations in CST (image) and WPLD.

The purpose of this study, is to calculate the electric field inside the head using WIPL-D and then compare these results with the one obtained from CST. Since these EM solvers are using different methods to calculate the electric field distribution inside the head, this comparison can be considered as a cross validation.

### 3.4.2.1 Qualitative comparisons

Knowing that the working frequency is equal to 1GHz, the associated wavelength in vacuum is  $\lambda_0 = 0.3 \text{ m}$ . Wavelength in a medium with relative permittivity of 61 (blood) reduces to  $\lambda_d = 0.046 \text{ m}$ . Hence by choosing a spatial step of 0.5 mm ( $\sim \lambda_0/100$ ) to represent the variations of the electric field we expect to have a good representation of it. After exporting the results from the software, a Matlab code is used to plot the figures. At a first step, we compare results with no other means than our eyes. These results are normalized as explained in section 3.3. In this way, after exporting the results from CST and WIPL-D a Matlab code determines the maximum and minimum values of electric field ( $C_{max}$  and  $C_{min}$ ) for each field mapping. For instance, in figure 15 these values are reported in  $dB\mu$ . Then the outcome of each solver will be normalized regarding the maximum and minimum respective values.

Moreover, it is important to notice that Plotting  $20 \cdot \log((\text{Module} - C_{min}) / (C_{max} - C_{min}))$  at the place that module is minimum will cause infinity so by replacing it with  $1.1 \cdot C_{min}$  at the position of minimum of the field we can avoid this happening.

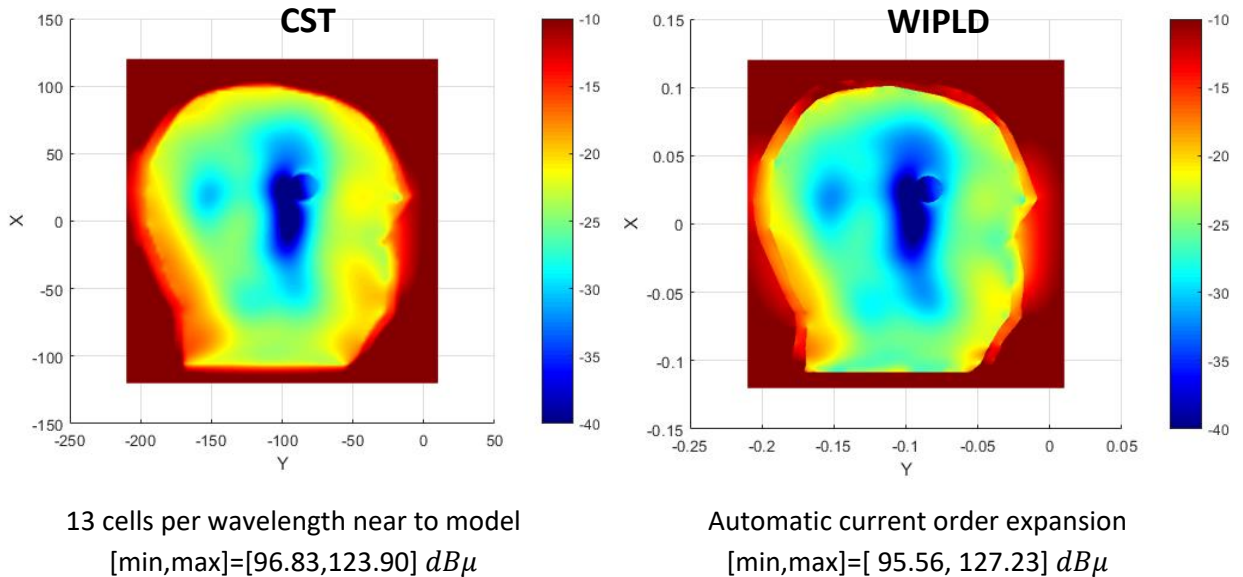


Figure 3.16: Comparison of the normalized E-field distribution inside the head from CST and WIPL-D.

This first comparison (figure 3.16) shows us that in both cases the position and shape of the hemorrhagic stroke is slightly detectable. On the other hand, the normalized electric field distributions for the two solvers are not the same. To study the origin of the difference between two outcomes, it is essential to make the comparison in the same conditions i.e. accuracy level, normalization function etc...

We have two software with different numerical methods to solve the problem and have the possibility to increase the accuracy of the calculations for both software. In CST, the accuracy defines with the size of meshes, which is set initially to  $\lambda/13$  while in WIPL-D the initial accuracy is set on automatic current order expansion. Moreover, Due to the differences in max and min values of the E-field in CST and WIPL-D simulations, the normalization is not applied fairly. To solve this problem, we define a fixed  $C_{max}$  and  $C_{min}$  based on the results previously obtained from the simulations. These values are defined as  $C_{max} = 2.3 \text{ V/m}$  and  $C_{min} = 0.06 \text{ V/m}$ .

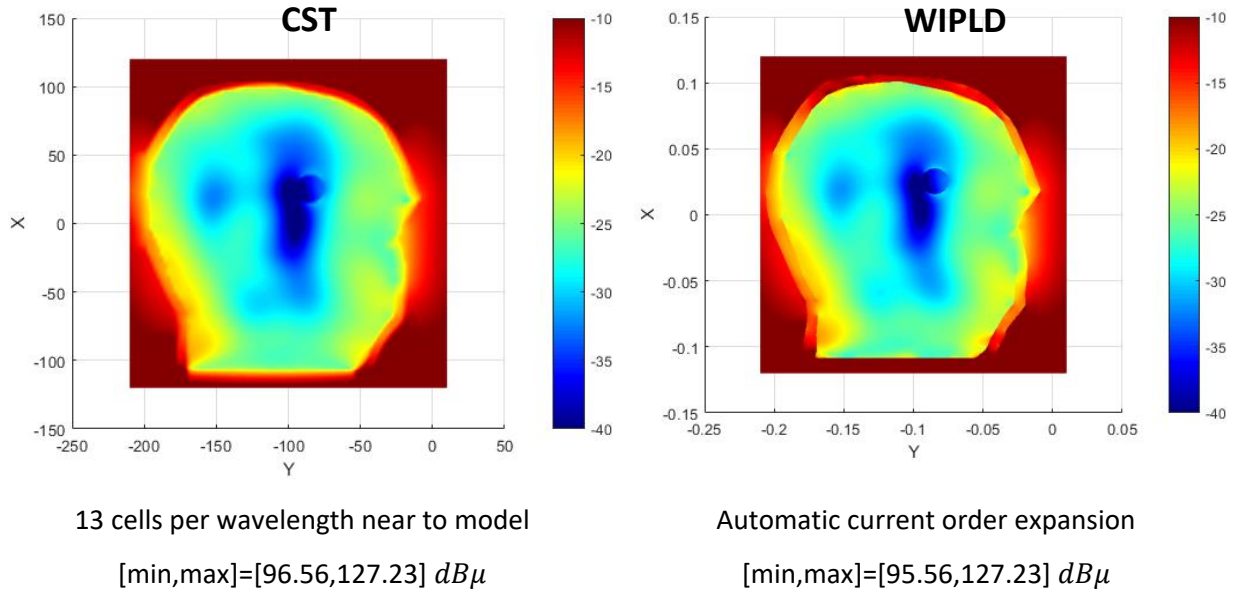


Figure 3.17: Normalized E-field distribution inside the head from CST and WIPL-D with the same normalization parameters.

The results obtained from CST and WIPL-D with same way of normalization are indicated in figure 3.17. Comparing these results with the one that we used different max and min for



normalization factors for each software output, one can see that considering the initial accuracy for both CST and WIPL-D results are in a close match. The next step is to increase the accuracy, which means increasing the number of mesh steps in CST, and current expansion orders in WIPL-D.

For checking the results in CST, the mesh steps are decreased from  $\lambda/13$  to  $\lambda/104$  while in WIPL-D the order of current expansion is increased two times than the initial default value.

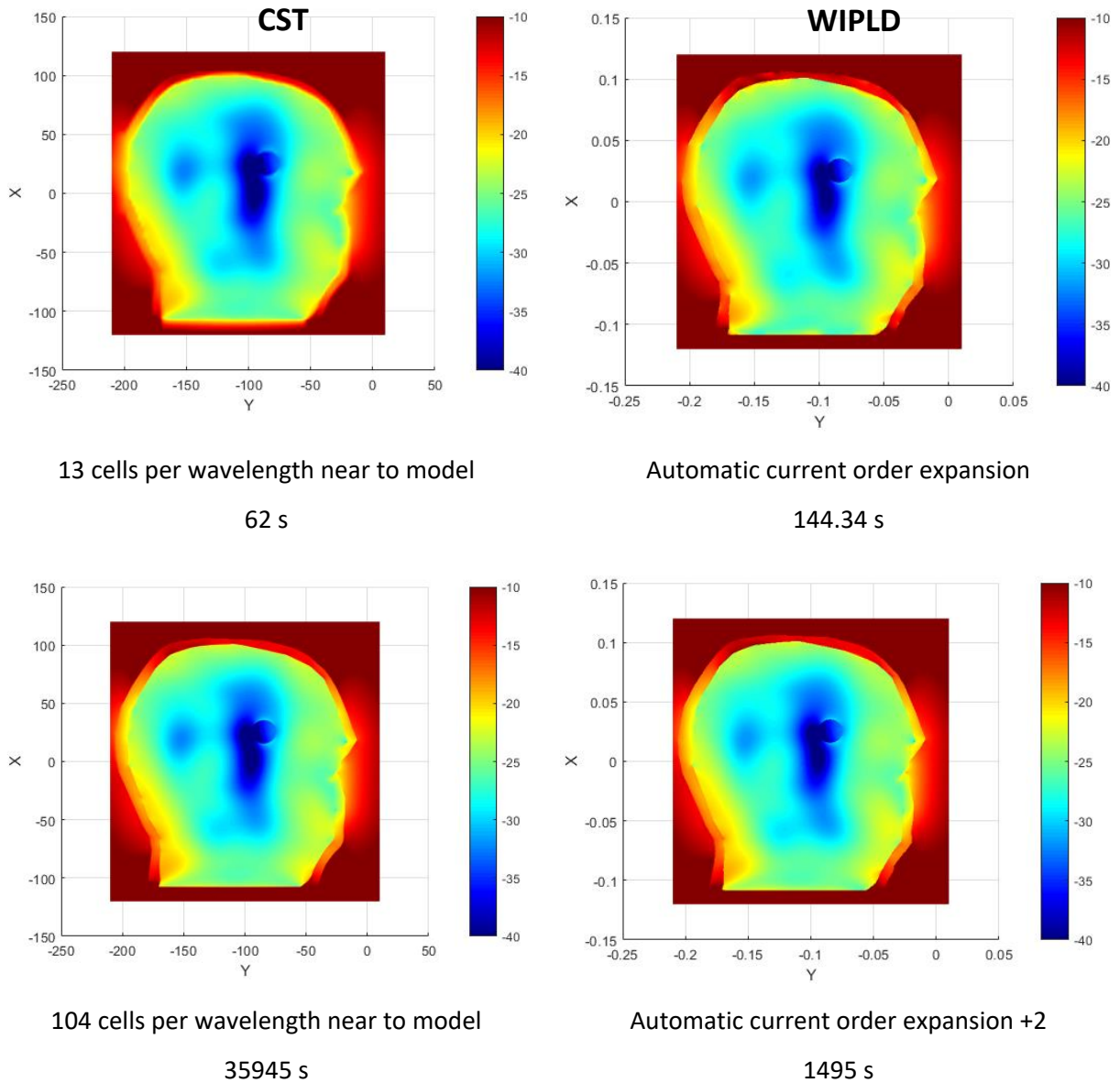


Figure 3.18: Normalized E-field distribution inside the head from CST and WIPL-D with the same normalization parameters and different accuracies. The simulation time for each simulation has reported below it.

By increasing the accuracy of the simulations, the simulation time increases as well. This is why we have to track the convergence of results and use the best simulation parameters. This means, the parameters in which gives us the most accurate results in the shortest time.

Comparing all results from different accuracies, we can see that the CST results when the mesh step is  $\lambda/26$  and WIPL-D results for Automatic current order expansion+1 are really close. The convergence of results for CST by increasing the accuracy of the simulations is acceptable since there is not a noticeable difference between CST figures by reducing the mesh steps. The same is happening for WIPL-D results and figures with Automatic current order expansion+1 and Automatic current order expansion+2 similar to each other. Based on the proposed most efficient configuration for two software (figure 3.19), it almost takes the same time for two software to run the simulations.

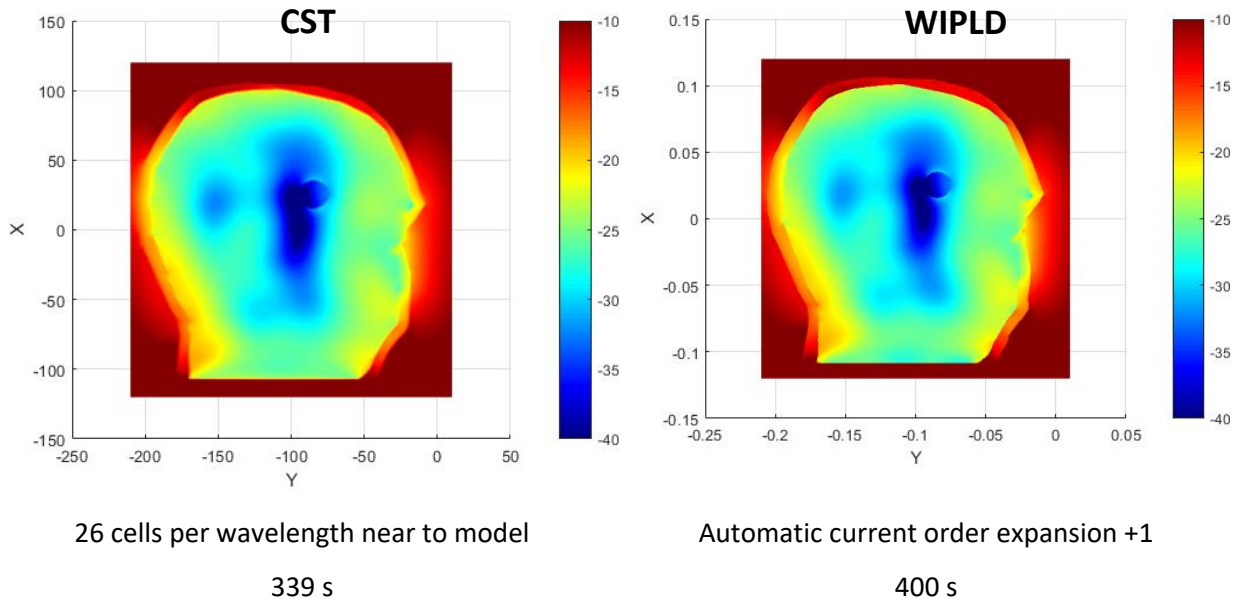


Figure 3.19: Normalized E-field distribution inside the head from CST and WIPL-D. The simulation parameters are the most efficient one based on comparison between simulation time and normalized E-field distribution.

### 3.4.2.2 Quantitative comparisons: Root Mean Square Error (RMSE) calculation

To translate the difference between simulations into number, the “Root Mean Square Error” between two data sets can be used on a specific plane. In addition, we will have an idea to choose the optimum simulation considering accuracy and simulation time. The RMSE is given by:

$$RMSE = \sqrt{\sum_{i=1}^n \frac{(x_i - \hat{x}_i)^2}{n}} \quad (3-6)$$

Where n is the total number of pixels, equal to  $441 \times 481 = 212121$ ,  $x_i$  is the module of the electric field obtained at pixel i of the model we are evaluating and  $\hat{x}_i$  is the module of the electric field obtained at pixel i of the reference model ( $\lambda/104$  for CST and w+2 for WIPL-D). W stands for results with the initial automatic accuracy in WIPL-D. +1 and +2 are symbols to show we increased the order of current expansion.

Table 3.1: RMSE values of simulations with different mesh steps and current order expansion compared with the highest accuracies in CST and WIPL-D.

CST	RMSE_v/m	RMSE_dB		WIPLD	RMSE_v/m	RMSE_dB
$\lambda/13, \lambda/104$	0.1163	1.3128		w,w+2	0.0144	0.2841
$\lambda/26, \lambda/104$	0.0345	0.4563		w+1,w+2	0.0048	0.1748
$\lambda/39, \lambda/104$	0.0242	0.2963				
$\lambda/52, \lambda/104$	0.0146	0.1753				
$\lambda/65, \lambda/104$	0.0102	0.1156				
$\lambda/78, \lambda/104$	0.0062	0.0753				
$\lambda/91, \lambda/104$	0.0039	0.0478				

To quantify the differences between each step after increasing the accuracy we calculate the RMSE for each step. Considering the simulation time for each simulation and the convergence pattern shared in the table below, one can decide the parameters of simulation efficiently.



CST	RMSE_v/m	RMSE_dB
$\lambda/13, \lambda/104$	0.0032	0.1784
$\lambda/26, \lambda/104$	0.00076	0.0498
$\lambda/39, \lambda/104$	0.00028	0.0191
$\lambda/52, \lambda/104$	0.00016	0.0104
$\lambda/65, \lambda/104$	0.0001	0.0059
$\lambda/78, \lambda/104$	0.00008	0.0042
$\lambda/91, \lambda/104$	0.000036	0.0019
WIPLD	RMSE	RMSE_dB
w,w+2	0.0024	0.1308
w+1,w+2	0.00068	0.0396

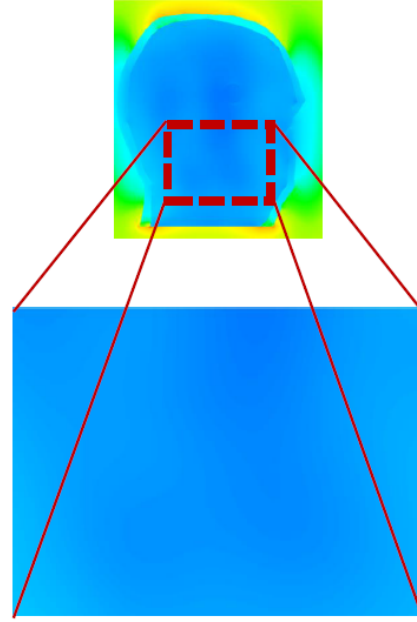


Figure 3.20: RMSE values of simulations with different mesh steps and current order expansion compared with the highest accuracies at the defined window inside the head phantom using CST and WIPL-D.

A visual comparison between the normalized E-field distributions in CST and WIPL-D for different accuracies showed us in the previous section that mesh step with  $\lambda/26$  and current order expansion of +1 in an efficient time gives us the best results and outcomes of two software are in good agreement. Here using RMSE analytically proves that the error between  $\lambda/26$  and  $\lambda/104$  is not significant while the simulation time is huge. In WIPL-D simulation same conclusion can be made, W+1 shows lower error than W while the simulation time differences between W+1 and W+2 makes us to choose W+1 as the current order expansion of the simulation.

It is noteworthy that CST uses the STL files of the phantom and does not change the meshing of the file while WIPL-D merges the triangles to quadrilaterals and this causes slight changes in the outer layer of the phantom and edges of it. These areas are the main sources of error in our studies. One solution to this is considering a window inside the head phantom and calculate the errors in

that specific area. Here we are studying the convergence of our results in the shown window by using CST and WIPL-D.

In this new configuration, RMSE is reduced drastically while the effect of edges is not considered. Same conclusion can be made by the RMSE values of the introduced window as the one made visually. Overall studying the RMSE of each simulation and the most accurate simulation is the chance firstly to check the convergence of the simulations and secondly to validate the results we get from different EM solvers.

### 3.5 Numerical simulations on axillary phantom

Electromagnetic simulations can be conducted on any phantom. As the second example, we consider the first prototype of axillary anthropomorphic phantoms designed to test the ongoing microwave device developed by FCUL. As described before in section 2.1.2, the phantoms contain lung and lymph node cavities and one piece of bone. In section 2.1.2 two types of phantoms are introduced. Here the one obtained from online library is used. In this phantom, a mixture with dielectric properties of muscle will fill the outer shell. The bone is made of plastic and the other cavities are the lung and lymph nodes, which are filled with relevant TMMs. The phantom is illuminated by a plane wave confronting the chest first at 1 GHz. As it is shown in figure 3.21, a difference of size instead of dielectric properties between malignant and healthy nodes is considered, since a lymph node that grows in size is pathological.

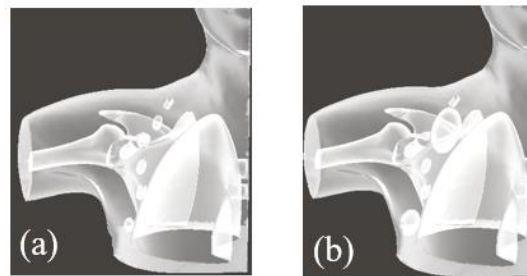


Figure 3.21: Thorax phantom including (a) healthy and (b) malignant lymph nodes.

### 3.5.1 Detection of different types of nodes

Here we distinguished the malignant and healthy nodes by their size instead of a difference in dielectric properties since it is not well developed in the literature. We consider a lymph node healthy with a width of 1 cm and malignant with a width between 2 to 3 cm. Figure 3.22 illustrates these two cases and the results of simulations.

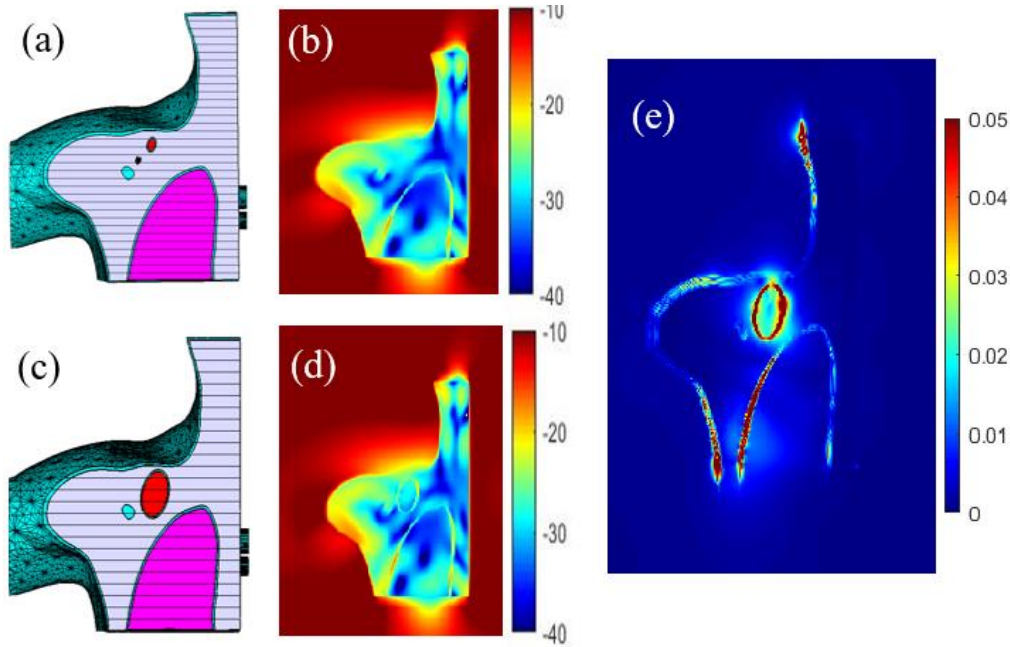


Figure 3.22: The normalized magnitude of the E-field outside and inside the Thorax phantom for detecting (a) healthy and (c) malignant lymph nodes, both in red. (e) The differential of field distributions for (b) healthy and (d) malignant lymph nodes.

It appears as one might expect, that the detection of large lymph node, unlike the small one, is more probable from the E-field distribution (figure 3.22b,d). The size of lymph nodes appears to affect the distribution of the field, allowing it to be detected despite the low dielectric contrast between the muscle and the lymph node. Note that in reality, there will probably be a dielectric contrast between the malignant and healthy nodes making the difference more significant.

### 3.5.2 Effect of the plastic

Effects of using plastic are studied by comparing the differential field distribution between malignant and healthy lymph nodes inside the thorax phantom with and without plastic shells in the simulations.

Figure 3.23 shows that this effect is different from the one on the head phantom since the source and the dielectric properties of materials used in the two phantoms are different. By only not considering the ABS around the lymph nodes, as it is indicated in Figure 3.23b the node is barely detectable. The results obtained from the CST simulations show that at the location of the malignant lymph node there is a variation of the electric field but the size and shape of the lymph node are not clear from it. Using plane wave as a source and different contrast of dielectric properties of the TMMs inside the thorax phantom can be counted as the reasons of high effect of plastic in this case study. Comparing Thorax phantom with the head phantom, the contrast between the dielectric constant of the bleeding case in head and brain is 45% while the contrast between the lymph node and the tissue around it is 8%. This leads to the point that by illuminating the thorax phantom by a plane wave, detecting the malignant lymph node will be difficult and the effect of the plastic shell looks dominant.

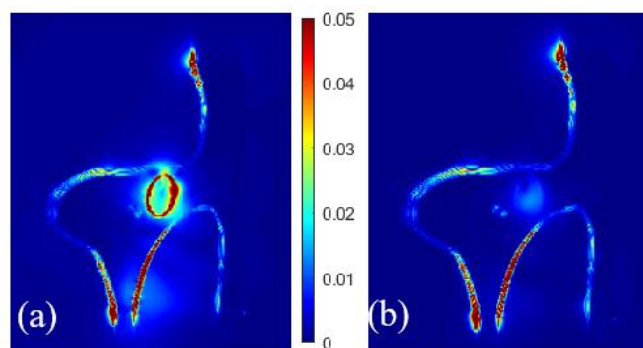


Figure 3.23: The differential field distribution inside the thorax phantom with malignant lymph nodes while (a) all cavities covered by plastic, (b) without ABS around the lymph nodes in our the simulations.

The study conducted by Matteo Savazzi using the same method (the differential field), which was practiced during his secondment in our laboratory, led to same conclusions [Savazzi *et al.*, 2020].

### 3.6 Conclusion

Simulation is an important part of our research since before conducting any experiment, the microwave imaging system configuration and phantom parameters can be studied and the most suitable setup can be used for the experiment. There are different commercial EM solvers. CST and WIPL-D are used for simulations in this thesis and based on two different numerical solvers, FIT and MoM, which are briefly explained in section 3.1.

There are several phantoms designed and printed during this PhD program. They were presented in chapter 2. In the “E-Field simulation of 3D anthropomorphic phantoms” chapter, different parameters of some of these phantoms are studied.

Head is one of the most complex parts of human body, which makes it an important case scenario for us. In this chapter, the importance of choosing a decent coupling medium is mentioned by studying the effect of two different coupling medium on E-field distribution inside the head phantom. The phantom design offers thickness of between 2 to 8 mm for phantom shell. It is shown by simulations that the thickness of plastic shell in this range does not have a significant effect of the E-field distribution inside the head phantom. The complexity of the head has also applied into the design to some extent by studying the number of cavities and adding blood vessels inside the brain cavity. It appeared that, in the frame of the POLITO system, it is not necessary to add a third cavity. Furthermore, the presence of vessels does not seem to have an effect on stroke detection.

Moreover, a part of this chapter is dedicated to a new technique in phantom design, which is numerical simplification of phantoms. This seems crucial since the STL files of the head originally

is densely meshes and it causes long simulation time in CST and WIPL-D. By using this technique, we reduce the number of meshes while designed cavities have almost the same shape as before simplification. The E-field distribution inside of the simplified head phantom is similar to the complex one, while the simulation time is reduced drastically when using WIPL-D. To support the simulation, WIPL-D is used to cross validate results obtain from CST.

Axillary phantom is another case, which enriches our studies, because this phantom is a different part of the human body. The objective is new and consists in finding malignant lymph nodes after using the differential technique. The dielectric properties of lymph node are different from a stroke and the environment around it has different dielectric characteristics. The phantom itself has more numbers of cavities and this makes it an important case study. This proves that the simulation-based technique proposed in this work, can be applied to any anthropomorphic phantom, as long as the model is in the format of an STL file. This opens new avenues to improve the design of phantoms and the device.

The axillary phantom used here is based on an online library one, which is justified and designed to its present form. The objective is detection of malignant lymph nodes inside the muscle cavity. Here we assumed that the malignant lymph node has the same dielectric characteristic as a normal node and the difference is only in size. This assumption is because the dielectric properties of malignant nodes are not reported precisely. Moreover, in reality malignant lymph nodes can be positioned in fat or muscles in axillary region. However, in this study we consider a malignant lymph node in muscle, which is more difficult to detect because of close dielectric properties between a lymph node and muscle. Results indicate that detection of malignant lymph nodes is possible by using differential technique while in the end of the chapter it has shown that the effect

of plastic shell around the lymph node cavity has a big impact on this detection, which is not desirable.

In this chapter there are several tools introduced for tissue extraction from MRI and CT scan, 3D modeling of anthropomorphic phantoms, and EM simulations. Due to the demands of the research groups collaborating in the frame of EMERALD project, there are several phantoms provided for each developed MWI system. The numerical version of these phantoms are used for 3D printing (as shown in chapter 2) and in this chapter several simulations are done to study different parameters of them before any experiment.

## 4 A priori information in inverse algorithms

### 4.1 Introduction

The work presented in this chapter is realized in collaboration with Lorenzo Crocco and Rosa Scapaticci of the CNR-IREA where I benefited from their expertise in the field of inversion during my last secondment.

In chapter two numerical versions of standard anthropomorphic phantoms were developed. This followed by studying the properties of the designed phantoms in chapter 3 and by introducing their anthropomorphic models into commercial electromagnetic software (CST and WIPL-D). The objective of chapter three is twofold, first to verify the accuracy of the electromagnetic field inside the anthropomorphic models by cross-validating the results provided by two different methods and second to develop a simulation methodology to characterize and improve the phantom and the device in the EMERALD project. In the current chapter, the gained knowledge of the phantom will be applied, through its numerical version, into the imaging algorithms in order to improve the spatial resolution of the microwave images.

The case study in this chapter is based on the GeePs-L2S breast phantom [Joachimowicz *et al.*, 2018]. Applying the simplification technique described in chapter 3.4 reduces the number of meshes of the anthropomorphic model. From the simplified STL file, a text file of the dielectric properties is produced including the dielectric properties of the phantom. This .txt file is the a priori information, which will be used to regularize the solution of the inverse algorithms. This allows us to calculate the theoretical induced currents in the breast, illuminated by a plane wave at 2.45 GHz, and to extract its contour. The permittivity map in a text format is also introduced in Matlab inversion codes developed by CNR-IREA [Scapaticci *et al.*, 2017]. These algorithms are based on the Truncated Singular Value decomposition (TSVD) [Bertero *et al.*, 2021].



This chapter is organized as follows. After introducing the microwave imaging problem (4.2), TSVD method is explained in 4.3.1. The next section (4.3.2) is devoted to the application of TSVD to a 2D breast phantom composed of only two layers. The effect of different parameters of the configuration on the reconstructed image are studied. Then, in section 4.3.3, the process is applied to the 3D anthropomorphic GeePs-L2S breast phantom and the reconstructed image's quality is improved by applying a priori information.

## **4.2 The microwave imaging problem**

During the last decade, microwave imaging has attracted an increasing interest for biomedical applications mainly due to the significant contrast in dielectric properties between normal and abnormal tissues. Compared to other conventional imaging modalities, such as X-ray mammography, microwave imaging is impressive in several aspects, for instance its non-ionizing nature and the low cost and compactness of the equipment associated with the hardware system. This is the reason why there are several researches conducted on bio-medical applications of microwave imaging right now around the world. This is evidenced by the emergence of several COST actions and projects. Among them, the European project “EMERALD” offers a unique opportunity for interactions between clinicians, instrumentation developers and researchers.

Hence, this study benefited from a complementary expertise of the CNR-IREA in the field of inverse problems (image reconstruction processes), laboratory where I spent three months and a half during my last secondment.

The imaging problem considered here seeks to retrieve a map of the dielectric contrast of biological tissues from measurements of the scattered electric fields that result from their interaction with a known interrogating wave (the incident field) in the microwave frequency range (herein 500 MHz – 6 GHz).

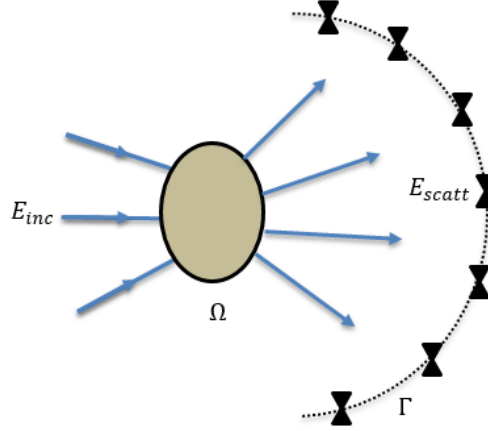


Figure 4.1: EM imaging is an invasive modality to qualitatively (or quantitatively) retrieve the image of inaccessible domain through EM probing.

Modeling of the wave – object interaction is based upon 3D domain integral representations of the electric fields that are radiated by Huygens-type sources induced within the object by the incident wave. This leads to two coupled integral equations that relate the measured scattered fields to the dielectric properties of the object.

$$E_s(R) = \int_{\Omega} G(R, r') \chi(r') E(r') dr' \quad R \in \Gamma \quad (4-1)$$

$$E(r) - E_{inc}(r) = \int_{\Omega} G(r, r') \chi(r') E(r') dr' \quad r \in \Omega \quad (4-2)$$

$\Gamma$  and  $\Omega$  are the observation and investigation domains.  $\chi$  is the dielectric contrast and accounts for the variation of the electric properties of the imaged scenario with respect to the reference one.

Retrieving the unknown object, while the incident and scattered fields are measured, is denoted as the inverse scattering problem. The equations show that the inverse problem is non linear and ill-posed. The latter means that the solutions do not simultaneously satisfy the conditions of existence, uniqueness and stability [Bertero *et al.*, 2021]. Therefore, they must be regularized which consists usually in introducing a priori information on the solution.

The purpose of this chapter is to introduce the contours of the developed anthropomorphic models as a priori information in the inverse algorithms developed at CNR-IREA. The study will be restricted to the contours of the breast Geeps-L2S phantom. Moreover, it is placed in the

framework of a pathological phenomenon follow-up (evolution of a tumor, or of a stroke, temperature increase...). In this context, this work is interested in small variations of a localized contrast, so the inverse problem to solve becomes linear.

### 4.3 Introduction of the contour as a priori information in TSVD method

#### 4.3.1 TSVD method and Born approximation

MWI systems developed in the frame of EMERALD project are all aiming to monitor the time evolution of abnormal tissues in different organs [Savazzi *et al.*, 2020; Wang *et al.*, 2021; Rodriguez-Duarte *et al.*, 2021]. Therefore, an imaging algorithm with differential approach can be suitable [Scapaticci *et al.*, 2018]. The TSVD inversion is one of these methods, which is a widely adopted way to solve linear ill-posed inverse problems. TSVD provides real-time results since the intensive computational part that consists of the computation of the total field distribution inside a given domain, can be done beforehand offline. This allows tracking the variations occurring in the tissues qualitatively.

Let us assume that  $\Omega$  is the volume of interest and this area is probed by means of  $N$  antennas at the frequency of  $f$ . The scattered field caused by the perturbation of the target will be gathered by the same set of antennas. By inputting the difference between scattering matrixes at two different times in the algorithm ( $\Delta S = S_{11}^2 - S_{11}^1$ ), the desired output is a map of electric contrast occurring between two measurements. The relationship between unknowns ( $\Delta\chi$  differential contrast) and the data ( $\Delta S$  differential scattering parameter) is provided by the linear integral equation in the frequency domain [Scapaticci *et al.*, 2018]:

$$\Delta S = \int_{\Omega} G(k, r, r_x) G(k, r_x, r) \Delta\chi(r, \omega) dr = L_0 \Delta\chi \quad (4-3)$$

Where  $r_x$  is the position of the antenna,  $k$  is the complex wavenumber in the background medium and  $G$  is the Green's function for background which is the solution of Helmholtz equation:

$$\Delta G(r, r_x) + k^2 G(r, r_x) = -\delta(r - r_x) \quad (4-4)$$

with  $G(r, r_x) = G(r_x, r)$  due to reciprocity [*de Hoop*, 1995]. Note that the Born approximation has been taken into account to derive equation (4-3) as well as the reciprocity property of Green's function which reflects that Green's function models both the radiation of the induced current to the receiving antenna,  $G(r_x, r)$ , as well as the field induced by the antenna in  $\Omega$ ,  $G(r, r_x)$ . Here the Green's function is not available analytically since the background is the reference scenario without anomaly, which is not a homogeneous space. Hence, instead of considering Hankel function to estimate (as in the 2D classical case), the Green's function is assumed to be related to the total field at the reference scenario [*Shea et al*, 2010]. Thus, it is possible to run some simulations beforehand using the numerical versions of phantoms and build up the numerical Green's function by using the E-field values calculated by the simulator.

Equation 4-3 is a linear problem since the relationship between the data and the unknowns is expressed through the linear operator  $L_0$ . In this inversion problem, the a priori information can come into play in the definition of  $L_0$ .

To solve such a linear and ill-posed inverse problem the TSVD scheme is used here and the unknown contrast is retrieved by means of the explicit inversion formula [*Bertero et al.*, 2021]:

$$\Delta\chi = \sum_{n=0}^T \frac{1}{\sigma_n} \langle u_n, \Delta S \rangle v_n \quad (4-5)$$

where  $\langle ., . \rangle$  denotes the scalar product in data space. Here  $\Delta\chi$  is a  $N_c \times 1$  matrix including the reconstructed differential contrast, with  $N_c$  being the number of the cells used to discretize the domain  $\Omega$ .  $\Delta S$  is a  $N_R * N_T \times 1$  vector (where  $N_R$  and  $N_T$  are the number of receiving and transmitting antennas) and  $\{u, \sigma, v\}$  denotes the singular value decomposition (SVD) of discrete

counterpart of the integral operator ( $L_0$ ) which is a  $N_c \times N_R * N_T$  matrix.  $\sigma_n$  are the singular values and their magnitude tend to zero for  $n \rightarrow \infty$ ,  $u_n$  and  $v_n$  are the left and right singular vectors of the linear operator  $L_0$ . In order to defeat the ill posed problem, a regularization has to be enforced by removing the lowest singular values. T in equation (4-5) is the truncation index of the SVD, acting as the regularization parameter being set manually in such a way to meet accuracy and stability of the reconstruction [Scapaticci *et al.*, 2017]. However, this operation removes probably the information about the presence of the high variations of contrast in the object. Indeed a comparison with the spectral algorithm named the diffraction tomography algorithm [Tabbara *et al.*, 1988] can be done here. In the latest, the filtering of the high spatial frequencies, which operates naturally in the spectral algorithm, should play the same role as the regularization parameter T introduced in the TSVD, in a way that the highest spatial frequencies in the spectral domain that contain information on the strong variations of the dielectric contrast should correspond to the lowest singular values. The introduction of a priori information on the contours, by allowing to fill the high frequency domain, should restore part of this information. Similarly, the introduction of a priori information in the TSVD method could restore the information included in the removed low singular values. Thus, this allows extending this technique to the detection of high contrast anomalies, such as tumors in the fatty part of the breast. In this chapter we propose initial investigations to explore these assumptions.

In the next section, the TSVD technique is applied to detect a tumor in a breast phantom by using the E-field distribution on a cross section of these phantoms. At the first stage, the phantom is a cylinder assumed to be infinite and we use a 2D version of the algorithm in order to test the effect of different parameters. Then we consider the 3D anthropomorphic phantom (GeePs-L2S breast phantom), the algorithm which is used is bi-dimensional and scalar instead of vectorial

tridimensional. However, note that there is no scalar approximation employed in the computation of the total field, since the total fields are computed by using a full-wave 3D numerical method (WIPL-D); the approximation is only in the construction of the inverse system. This is a real benefit of this technique.

The study goes further by introducing the outer contour of the phantom in the algorithm to improve the detection of the tumor.

#### 4.3.2 Numerical analysis on a 2D case

The 2D breast phantom consists of two 500 mm long, cylinders (almost  $4\lambda_0$  at 2.45 GHz) nested inside each other. The outer cylinder represents the fatty part and the other represents the tumor. The outer and the inner diameters are 96 mm and 20 mm, respectively.

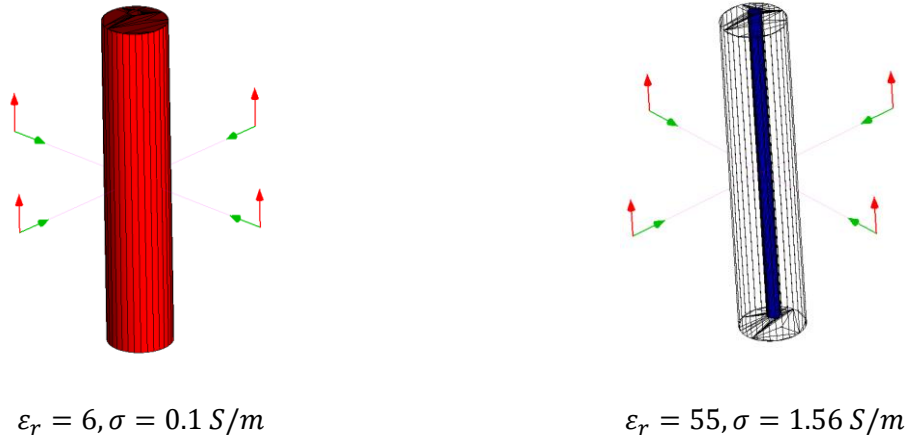


Figure 4.2: Fatty and tumor part of the breast with their dielectric properties.

##### 4.3.2.1 Cross-validation of the electromagnetic field computation

Accurate calculation of the total field in the object is crucial in TSVD technique. In order to evaluate the validity of the studied 2D configuration, a comparison between a 2D code developed in the laboratory based on an integral formulation solved by a Method of Moments [Joachimowicz *et al.*, 1991] and WIPL-D is proposed. The simulations are done at 2.45 GHz and four incident

plane wave illuminations are considered. The center of the bigger cylinder is (0, 0) while the smaller cylinder's center is located at (18 mm, 18 mm). At this frequency, the length of the cylinder is around four times of the wavelength, the question is whether it can be compared to an infinite cylinder.

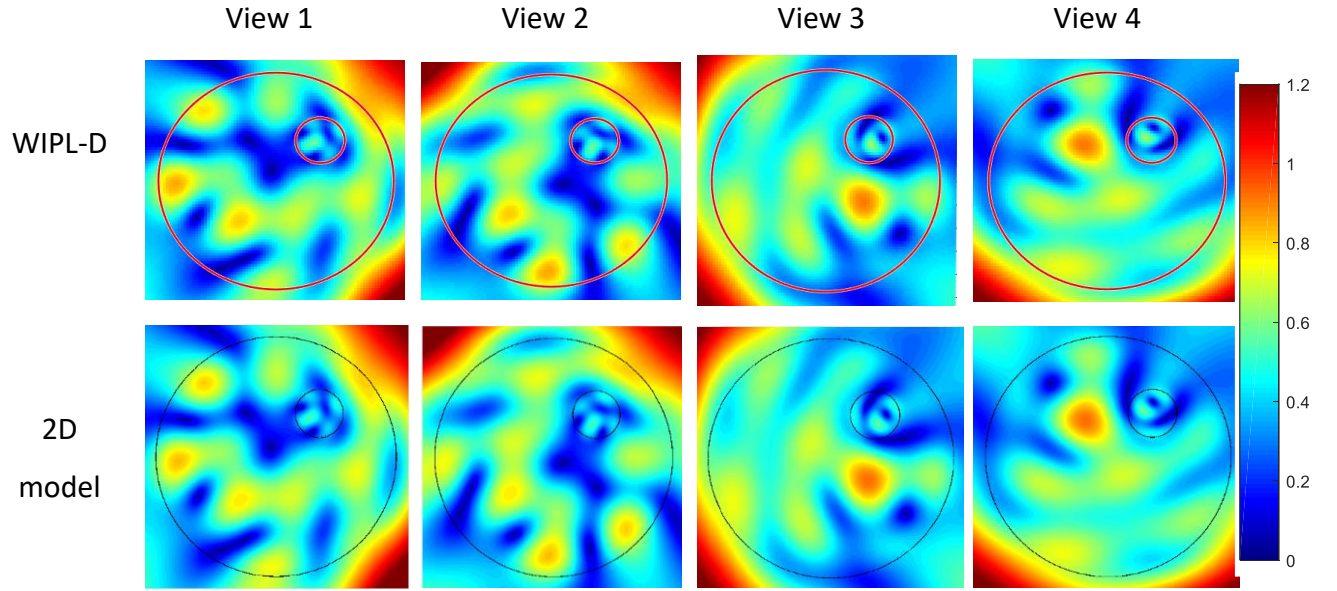


Figure 4.3: The magnitude (V/m) of total E-field distribution inside the cylinder for four incident plane waves using two different methods.

In figure 4.3, the magnitude of E-field distribution is shown for the 3D (WIPL-D) and 2D approaches [Joachimowicz *et al.*, 1991] at half height of the cylinder. The two results are in good agreement showing that the infinite cylinder approximation is valid for the case of study proposed here.

#### 4.3.2.2 Toward a suitable configuration

In this section, parameters of a suitable configuration including the number of antennas, the length of the antennas and the coupling medium are searched for. This leads us to obtain adequate information as the input data for the inverse algorithm. The goal here is to detect high contrast anomaly such as a tumor in fatty part.

For each case, the  $S$  matrix is computed for two scenarios (with and without tumor) and the differential data constitute the input of the will use TSVD algorithm to reconstruct the image. In fact, the knowledge of the structure inside of the breast comes into play in the construction of the Kernel of the integral operator, which is both Green's function, and the electric field of the reference scenario. In next steps, we will study different reference scenarios and their impacts on the reconstruction of the image. To use the contour of the phantom as an a priori information, we will use the STL file of the phantom to create a mask and will apply it to the algorithm in a way that it will only focus on the inside of the contour that we know the tumor is there.

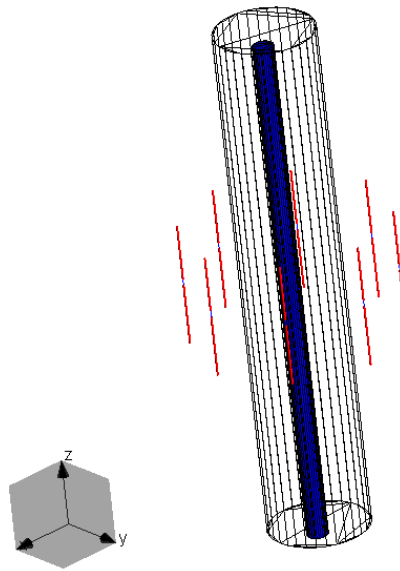


Figure 4.4: The same cylinder as figure 4.2 surrounded by 8 antennas with length of 120 mm collecting data for reconstruction.

#### Effect of the anomaly's contrast

To study the effect of the dielectric properties of the target on the reconstruction of the image, here the same cylinder as introduced previously is considered. Three different permittivities for the tumor are tested. There are eight dipole antennas parallel to the largest axis of the cylinder placed in free space, positioned on a circle with the radius of 100 mm on a plane at the mid height of the cylinder (see figure 4.4) with the same center as the bigger cylinder. Since in TSVD



algorithm some equations are simplified based on the Born approximation, by increasing the relative permittivity of the tumor from 8 to 55 the accuracy of the reconstruction will change. The singular value curves for these three scenarios are almost identical and the truncation index of 36 provides the best reconstruction. As expected, the most accurate result is when we use the lower contrast for the target (figure 4.5). From relative permittivity of 8 to 20 for the tumor, one can see a small shift in the position of its reconstructed image. Then by increasing it to 55, the reconstructed image shows false information on the location of the tumor.

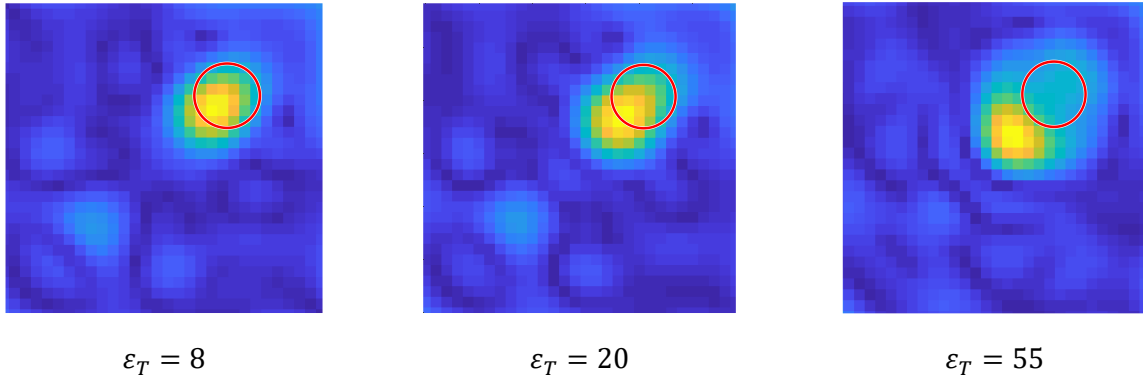


Figure 4.5: Losing the accuracy of the reconstructed image by increasing the dielectric properties of the tumor.

Next a priori information is introduced.

#### Effect of the mask as a priori information

Masking is a technique that can help the algorithm to find the target with more accuracy. To this end, we use the numerical model of the phantom (figure 4.6 b) to have the contour of the outer shape of it (figure 4.6 a). It is applied to the linear operator giving the algorithm a priori information that we are looking for the target only inside the domain defined by the mask.

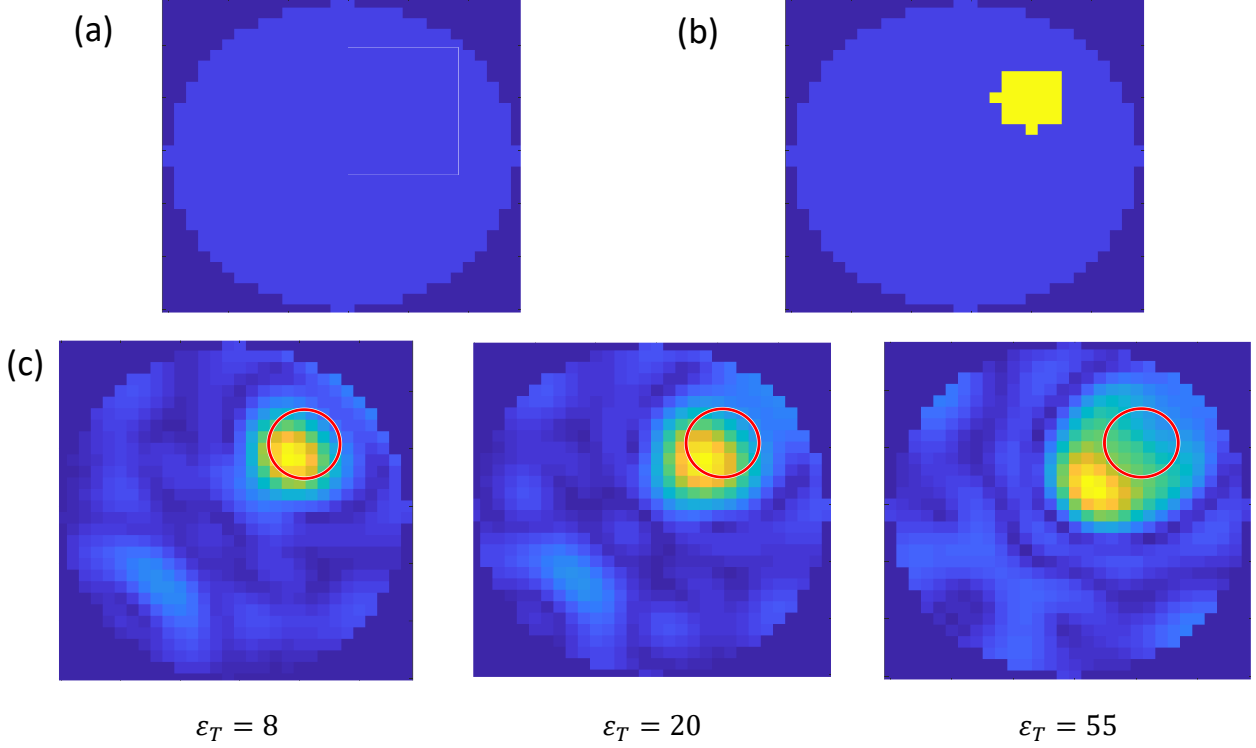


Figure 4.6: (a) The outer contour of fatty tissue, extracted from (b) the contrast map, is used for masking the linear operator. (c) Losing the accuracy of the reconstructed image by increasing the dielectric properties of the tumor while using the mask.

Figure 4.6 c indicates that the reconstructed image has no information outside the fatty cylinder. We observe that the a priori information added does not improve the quality of the image, the anomaly is still off center and the a priori information did not help the reconstruction for finding the target with high contrast permittivity such as tumor in fatty breast.

#### Effect of discretization

After running the reference scenarios and doing the initial computations to be able to build the Kernel of the integral operator, we need to extract the data from the EM software. The data can be exported with different resolutions, allowing us to study the effect of the resolution on outcome of the reconstruction. The behavior of the singular values is represented on the right part of the figure 4.7 for two different image resolutions and  $\epsilon_T = 55$ . This curve that gives the information on the ratio between the singular values and the highest value, allows the choice of the truncation

parameter  $T$ , around 35 in this example. As we can see, the same curve is observed when the resolution increases, which proves that the  $30 \times 30$  discretization is satisfactory. Because of that, the image of higher resolution has the same quality, in the respect that it does not help to find the location of the tumor.

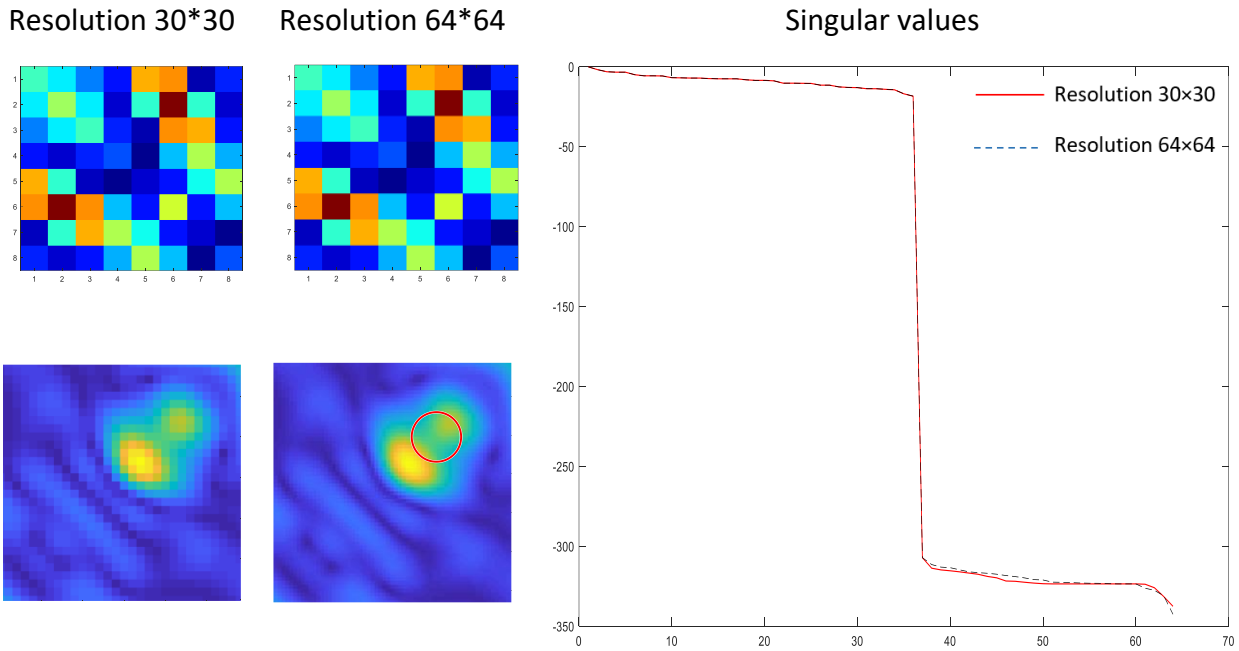
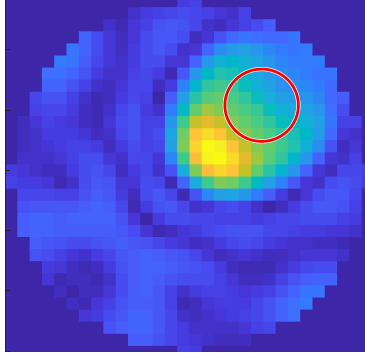


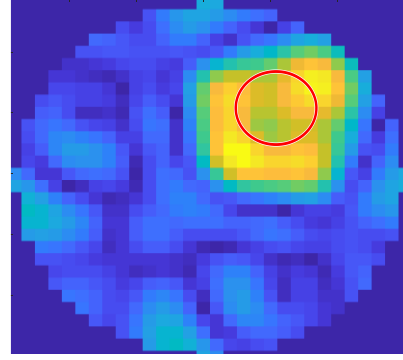
Figure 4.7: S matrix, reconstructed images for two resolutions of  $30 \times 30$  (red line) and  $64 \times 64$  (dashed black), and the singular values (in dB).

#### Effect of the antenna's size

Another interesting parameter to study is the size of the transmitting and receiving antennas. We know that using smaller antenna will help to detect the target inside the phantom better. In fact, by having a small sized antenna compared to the wavelength, the beam will be uniform and in this way, it covers more surface of the phantom. It is noteworthy that by changing the size of antenna, the power emitted by the antenna is changed and the emitted power is affected by that.



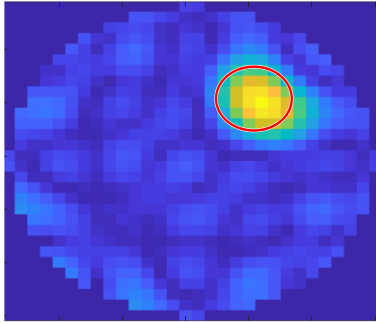
Antenna size: 120 mm



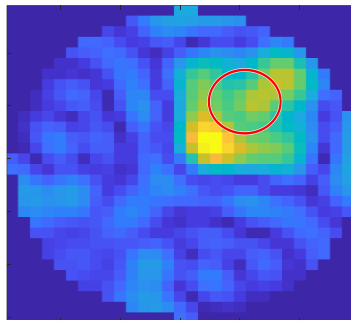
Antenna size: 12 mm

Figure 4.8: The effect of changing the length of antennas around the phantom on reconstructed image.

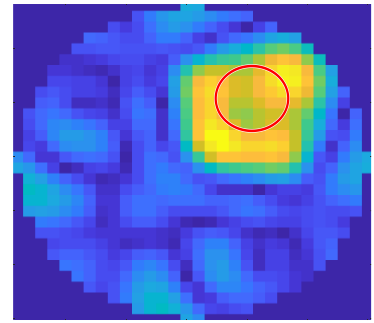
Reducing the antenna size showed us that the results obtained are improved if we use smaller antennas (see figure 4.8). On the other hand, for the 3D reconstruction, where we need to use several arrays of antennas, it is important to create a uniform beam radiated by each antenna to cover the surface of the object. Therefore, from this point onward we will use dipoles with length of 12 mm as transmitter and receiver. With this new configuration of antennas also it is expectable that again a target with lower dielectric properties is easier to be detected as shown in figure 4.9.



$\epsilon_T = 8$



$\epsilon_T = 20$



$\epsilon_T = 55$

Figure 4.9: Losing the accuracy of the reconstructed image by increasing the dielectric properties of the tumor while using the mask (antenna size is 12 mm).

#### 4.3.3 Numerical analysis on a 3D anthropomorphic breast phantom

This section is dedicated to reconstruct the image of on cut of a 3D GeePs-L2S breast phantom whose cross-sectional size is of the same order as that of the cylinder considered above (about  $\lambda$  in free space). To do that the 3D phantom is simplified in a first step in order to optimize

the calculation time and memory space in the WIPL-D software. Moreover the simulations will take into account the results of the previous ones on the cylinder, by choosing an experimental configuration consisting of 8 dipoles of size 12mm ( $\lambda/10$ ).

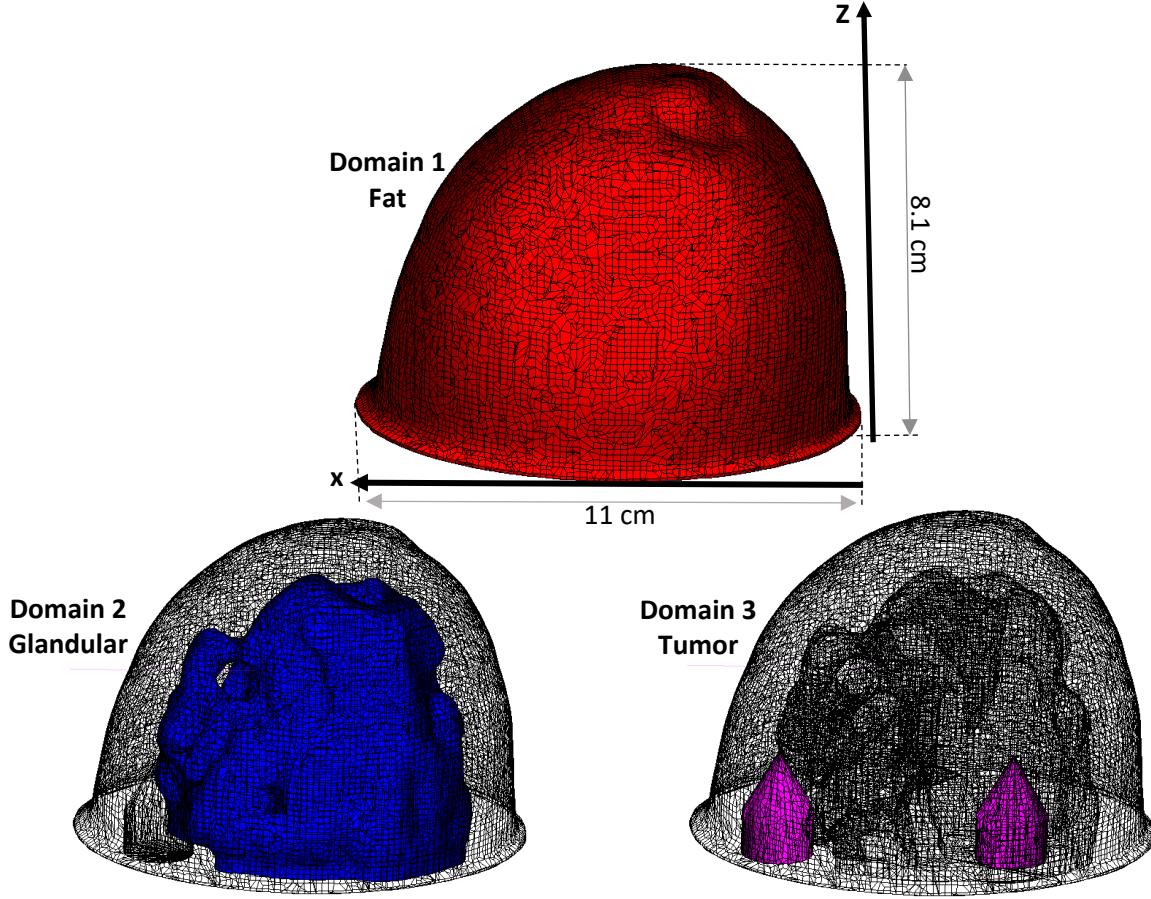


Figure 4.10: Three domains of the breast phantom

#### Simplification of the anthropomorphic model

The original STL file corresponding to the breast phantom comes from the University of Wisconsin–Madison [Burfeindt *et al.*, 2012]. This file has been modified by means of a computer-aided design software to separate two distinct cavities, fatty and glandular cavities [Joachimowicz *et al.*, 2018]. Moreover, two cylindrical tumors are added inside the phantom in such a way they can be filled by TMMs easily. One tumor is located in the fatty part and the other one in the Glandular part (see figure 4.10).

Due to the high contrast between the dielectric properties of tumor and fat, we expect that the algorithm will be able to find the location of this tumor easier than the one in the glandular part.

Table 4.1: Dielectric properties of different domains of the breast phantom

@2.45 GHz	Domain 1 Coupling medium	Domain 2 Fat	Domain 3 Glandular	Domain 4 Tumor
Relative Permittivity	1	5	47	53
Conductivity	0	0.1	1.4	1.8

As mentioned before WIPL-D is based on a Method of Moment (MoM) using high order basis functions. In this way, the number of meshes on the surface of the structure in the simulation has a direct relation with the number of unknowns and simulation time. The more dense the meshing is the longer the simulation time will be. As mentioned in chapter 2, after extracting the STL file of the organ from the MR image or CT scan, we will have a finely meshed phantom.

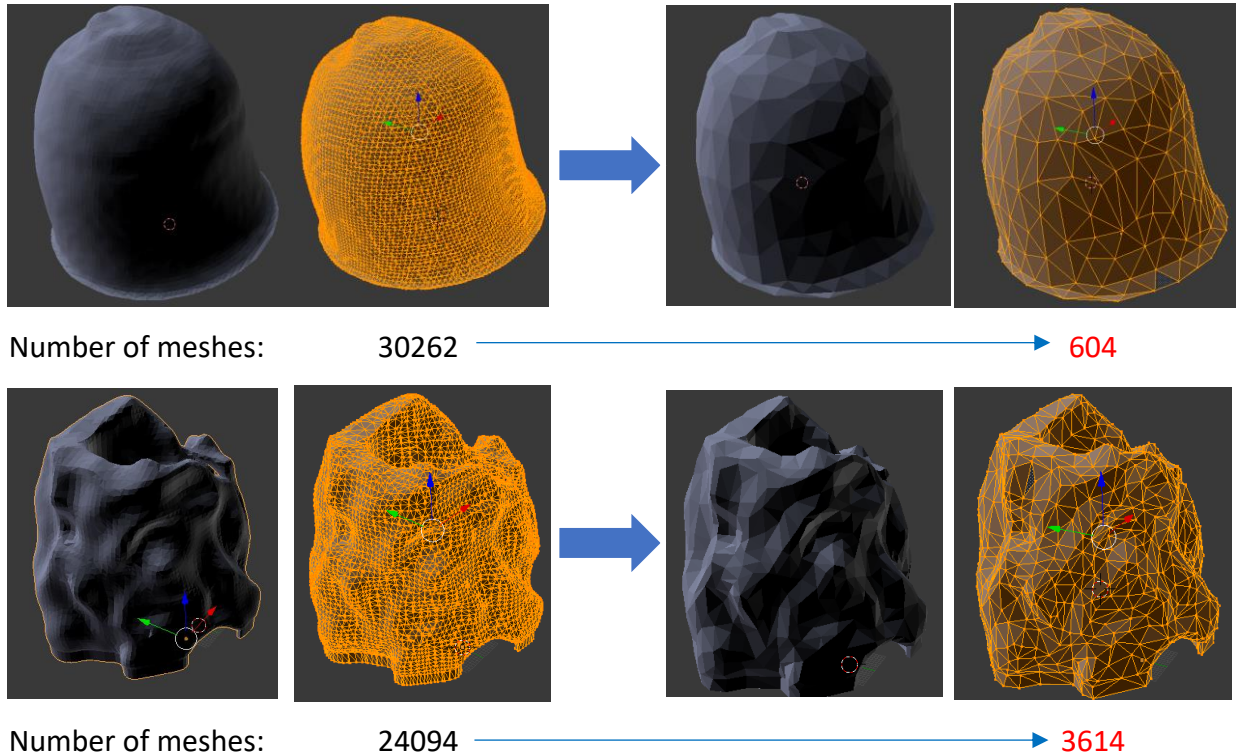


Figure 4.11: The result of the simplification of different cavities of the phantom breast.

In chapter 2, we showed that not all these small details on the phantom are necessary to obtain the exact field inside it and at the same time, we know that these unnecessary details lead to a big number of unknowns. The solution to this issue is the simplification of the phantom without a significant change in the phantom shape (see figure 4.11). Using Blender for this purpose, the number of meshes has been reduced, for instance from 30262 to 604 for the outer shell of the breast phantom, and from 24094 to 3614 for the inner shell that have a more complex shape.

Before starting using the simplified phantom in our simulation, we must check that using a simplified version of the phantom will not change significantly the E-field distribution inside the phantom. The process of simplification is small adjustment of the surface and merging meshes to keep the shape of old phantom with less number of meshes. These adjustments are so small compared with the wavelength so we do not expect a significant change in the field distribution. To prove this, we ran simulation in WIPL-D using the complex and simplified breast phantoms with and without tumors in fatty and glandular part. In this configuration a plane wave is illuminated to the phantom and the electric field distribution is calculated in the cross section at the height  $z=10$  mm (bottom of the breast and the middle of the two tumors).

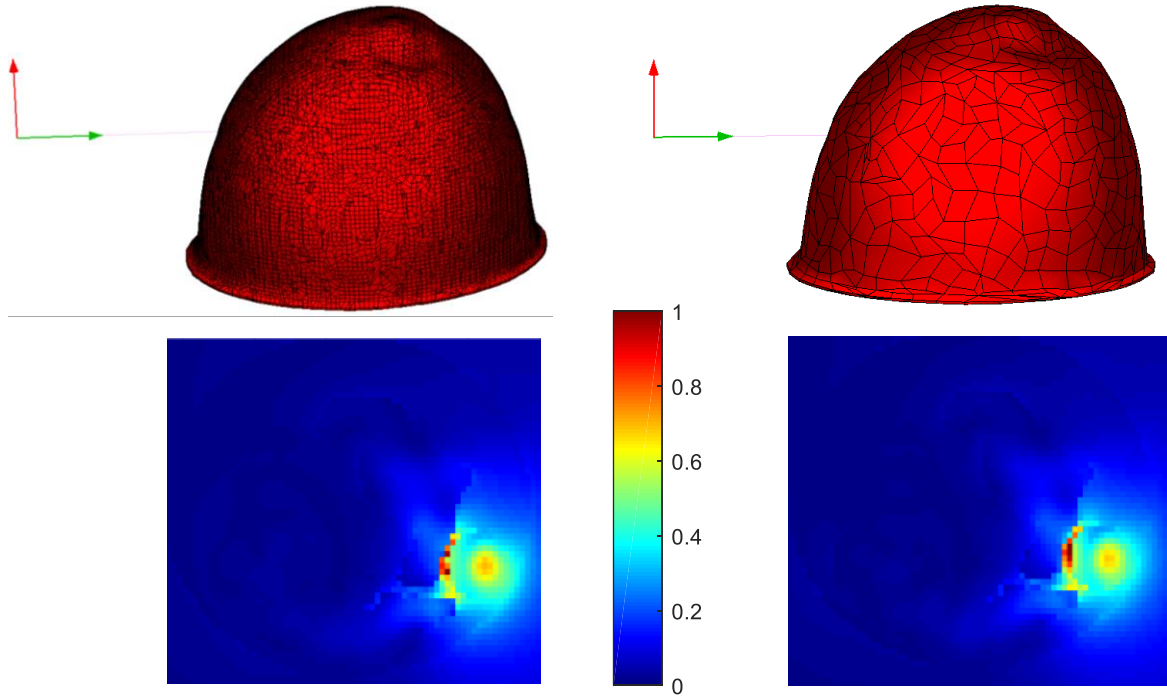


Figure 4.12: Differential total E-field for the breast phantom and simplified version of it for the case with and without tumor on the cross section  $z=10$  mm.

As indicated in figure 4.12, using the differential technique by subtracting the E-field with and without tumor, we localize the tumor in the fat easily while the electric distribution does not give any information about the tumor in glandular part. In addition, the results obtained from two phantoms are similar. Hence, the simplified phantom will be used in all the following simulations, and the computation time will be significantly reduced as shown on the table 4.2. Below the details of two simulations are reported.

Table 4.2: Information on simulation of the complex and simplified breast phantoms by illumination of a plane wave.

	Complex breast phantom	Simplified breast phantom
Number of faces	54800	5400
Resolution of figures	80*67 pixels	80*67 pixels
Simulation time	~ 2 h	~ 1 min

#### Extraction of the contour of the GeePS-L2S breast phantom



By running multiple simulation by WIPL-D, we obtained the contrast map of the breast phantom at  $z=10$  mm (figure 4.13). This map provides us a digital contour of different tissues with different dielectric properties. In this work, we are going to use only the outer contour of the fatty part to define the breast domain.

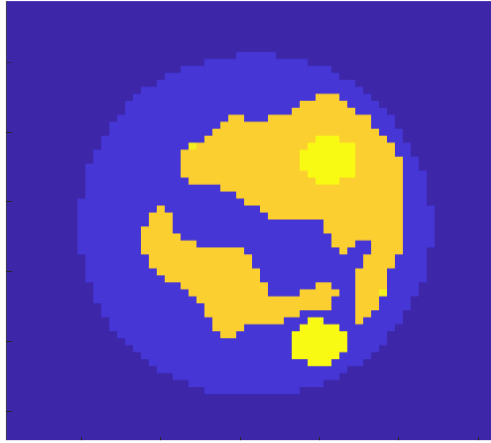


Figure 4.13: Contrast map of the breast phantom at the height  $z=10$ . Fatty, glandular part and tumors are recognizable by their contrast.

#### Use of the TSVD algorithm

Here we use the results of the previous study on the cylinder, to reconstruct the anthropomorphic phantom with and without a priori information with the bidimensional TSVD algorithm.

The phantom has three parts as shown in figure 4.9 and the dielectric properties of each part are mentioned in table 4.1. As it is shown in figure 4.12, detecting the dielectric perturbation corresponding to the tumor in the glandular part, is not possible through the differential electrical distribution due to low contrast between tumor and glandular tissue. This is why now we consider the tumor inside the fatty part. So in this section, differential scattering parameter ( $\Delta S$ ) used in the TSVD code is calculated for scenarios of with and without the fatty tumor while the glandular tumor presents and located as depicted in figure 4.10.

By considering free space as the coupling medium and 8 dipole antennas around the breast phantom, we run a couple of simulations with WIPL-D for each view to build the linear operator.

By collecting the S-parameter of antennas with in the configuration described above, we are able to reconstruct the image given in figure 4.14. We use three-dimensional phantom in our simulations but we are going to reconstruct only one cut of this setup. The considered plane goes through the middle of tumors.

The singular values obtained for this case show a rapid drop in their values (see figure 4.14 a). The main reason for this type of behavior can be the lack of information in the data that can lead to a bad reconstruction. Based on the obtained singular values, only the first few ones have information and the rest cannot help reconstructing an image. Figure 4.14 b shows the reconstructed image for T equal to 15. This reconstruction is a fail and we are not able to see the tumor in the reconstructed image.

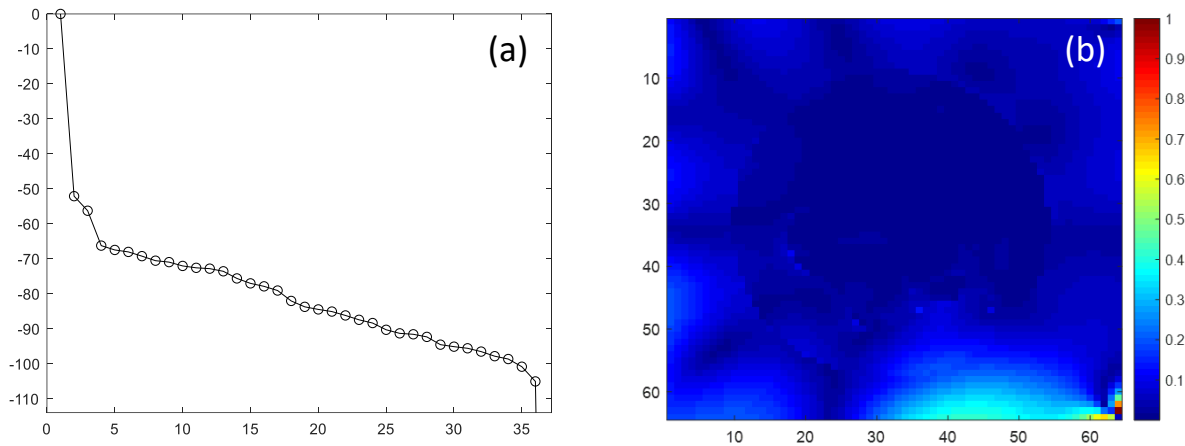


Figure 4.14: (a) Singular values curve (in dB). (b) Reconstructed image of breast phantom at height  $z=10$  mm.

Next, we are going to use coupling medium with dielectric properties of  $\epsilon = 18$  and  $\sigma = 0.01S/m$  as used in [Scapaticci *et al.*, 2012] to have a better matching and consequently more power penetration.

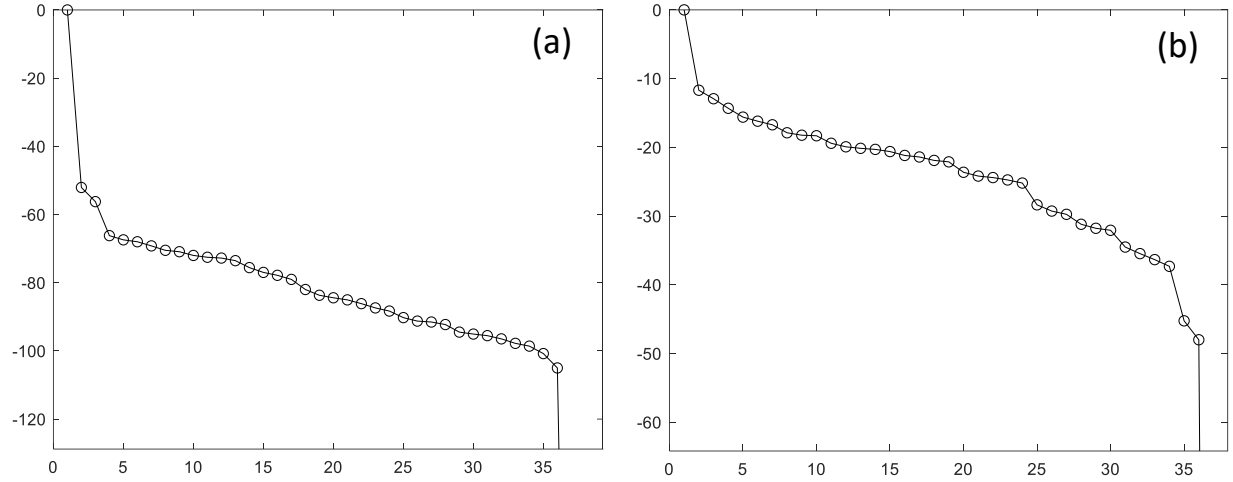


Figure 4.15: Singular value curves for scenarios with (a) free space and (b)  $\varepsilon = 18$  and  $\sigma = 0.01 \text{ S/m}$  as coupling medium.

Figure 4.15 gives a comparison of the singular values behavior between the scenario in free space and the one with the new coupling medium. The very first singular values drop fast to around -60 dB when the coupling medium is free space, while with the new coupling medium, the first singular values drop to -15 dB, allowing less singular values to be removed. Calculating the power penetration density for these two scenarios also validates our understanding of using the new coupling medium. As shown in figure 4.16 the range of power density for the breast in free space is much lower than the breast in a coupling medium with higher permittivity.

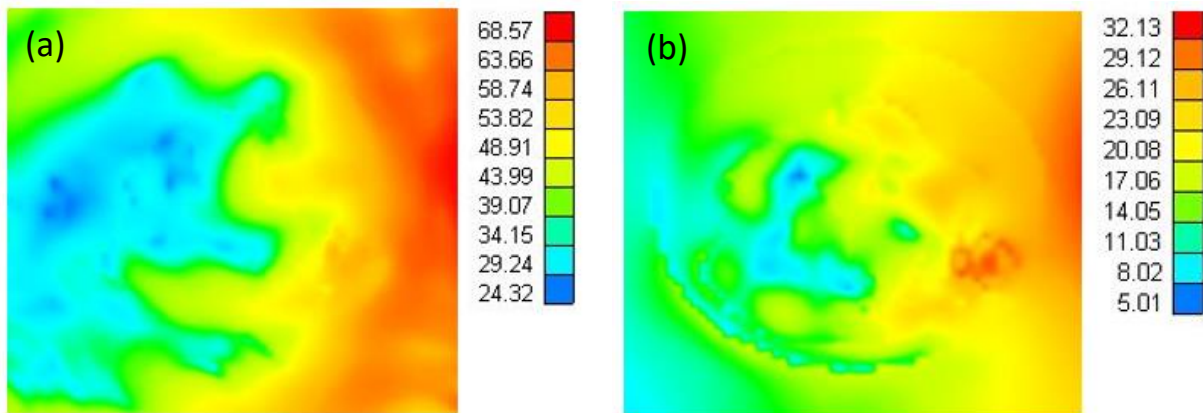


Figure 4.16: Power density distribution in  $\text{dB}\mu\text{W}/\text{m}^2$  for two scenarios: (a) with coupling medium and (b) in free space.

To have an efficient detection, the E-field has to penetrate inside the phantom and the perturbation of field should change the S parameters. This means the dielectric properties of the coupling medium has a critical impact on the reconstructed image and finding a proper coupling medium will help us on a better reconstruction. Therefore, the reconstruction with the new coupling medium provides more details (figure 4.17). Still it does not show the shape of the tumor, we observe contrast variation near the tumor location and outside the outer contour of the phantom. Therefore, we expect here that the a priori information, as introduced in the TSVD method, is effective.

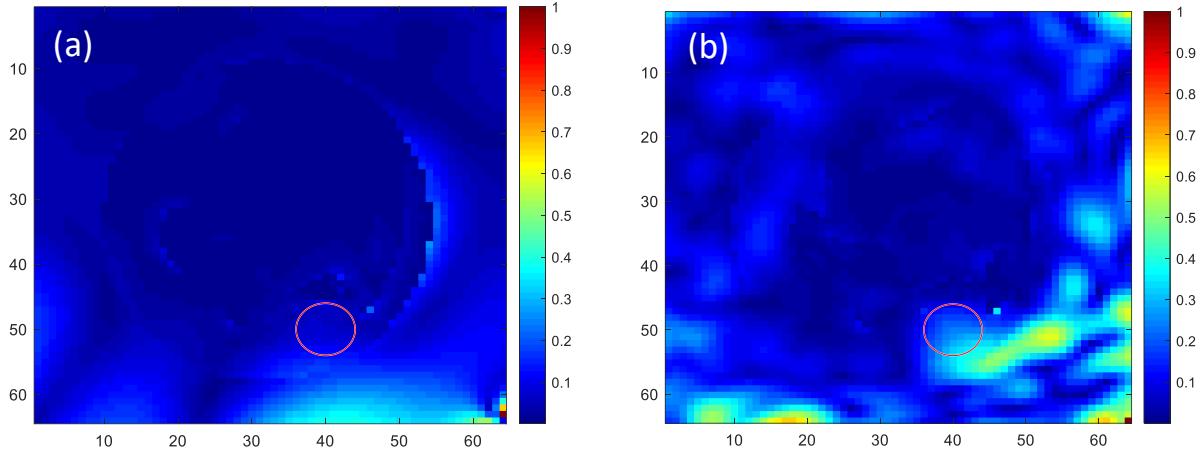


Figure 4.17: The effect of changing the coupling medium on reconstructed image. The reconstruction is done for (a) free space as coupling medium with  $T=18$  and (b) for coupling medium of  $\epsilon=18$  with  $T=30$ .

As before the outer contour of the breast phantom is going to be used to correct the linear operator and help the inverse algorithm. In figure 4.18, the reconstruction considering the masking technique for scenarios with the different coupling mediums is compared. By using the contour of the fatty part as a priori information, the quality of the reconstructed image is improved, allowing to determine the correct location and shape of the tumor.

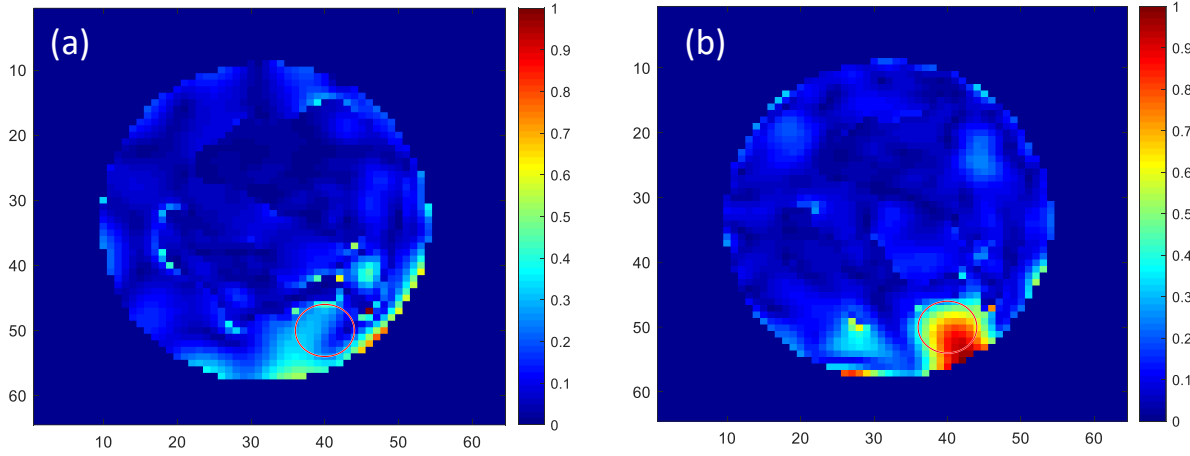


Figure 4.18: The effect of changing the coupling medium while applying a priori information on reconstructed image. The reconstruction is done for (a) free space as coupling medium with  $T=18$  and (b) for coupling medium of  $\epsilon=18$  with  $T=30$ .

Until now in this chapter, the differential  $S$  matrixes are obtained from two cases with and without tumor in fatty part. By considering the tumor in glandular part of breast, we do not expect to have a better view than the tumor in fat. This is due to the fact that the contrast between glandular part and tumor is much lower than the contrast between fat and tumor. To be able to detect the tumor in the glandular part it is necessary to have optimized antennas designed for medical applications with a proper coupling medium. Here we run some simulations with the same configuration as before to see if it is possible to see the location of the tumor in glandular part as well as in fatty part.

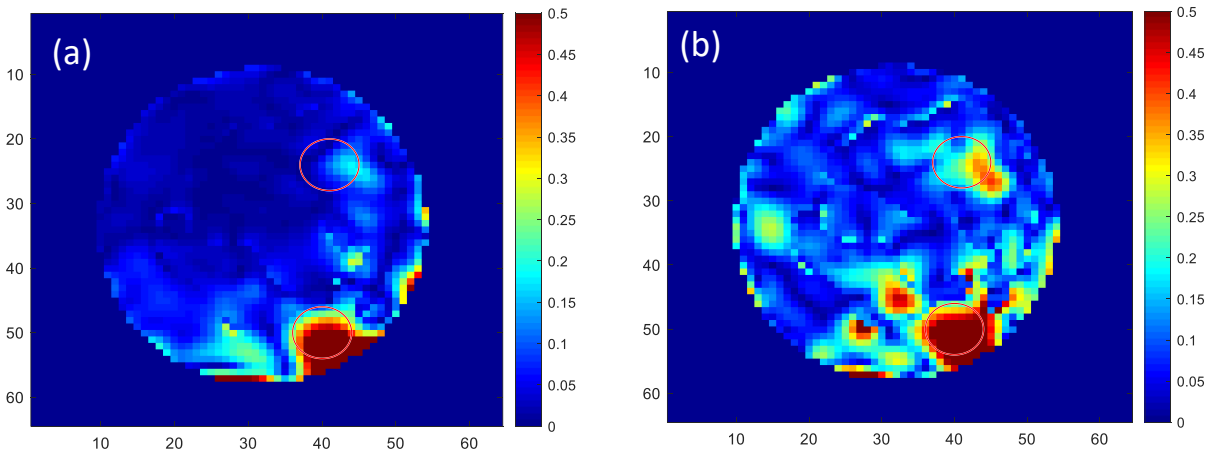


Figure 4.19: Reconstructed image of the breast phantom at the height  $z=10$  mm for two different truncation index (a)  $T=25$  and (b)  $T=35$ . In this configuration, both tumors in fat and glandular part are considered. The red circles show the location of the tumors.

As shown in Figure 4.19, the spatial resolution of the reconstructed image is not sufficient to detect the exact location of the tumor and recognize its shape in the glandular portion. The increase of  $T$  provides artifacts in the image.

#### 4.4 Conclusion

As the conclusion of this chapter, we showed that we are able to use 3D models to reconstruct images based on the results of 3D EM solver. We developed a simplified breast phantom including three parts with different dielectric properties. By using eight dipoles around this phantom in free space at the height  $z=10$ mm, we reconstructed an image by using TSVD algorithm. The results were showing neither the shape nor the location of the tumor in fat. Thus, we considered different ways to help the algorithm and obtain better results. By changing the coupling medium, we have shown that better penetration results in a better reconstruction quality. Using STL files of the human organs, which are obtained from MRI/CT scans of patients, can help the inverse algorithms to reconstruct images with more details. In the example showed in this study, this a priori information help in the detection of tumors with high dielectric contrast anomaly such as those existing in the fatty part and further research will be necessary for the detection of low dielectric contrast anomaly such as those existing in the glandular part. Among them are the use of different antennas to increase the power penetration density inside the breast, and a better knowledge of the right way to truncate. The joint use of TSVD and the diffraction tomography algorithms could be an interesting approach in this context.

## 5 Conclusion and future work

The work included in this dissertation was focused on standard phantoms for EM device testing in the context of EMERALD, the coherent action of leading European engineering groups for medical imaging. The study was made at Labo GeePs in collaboration with several partners from National university of Galway (NUIG) in Ireland, WIPL-D in Serbia, Faculdade de Ciências da Universidade de Lisboa (FCUL) in Portugal, and CNR-IREA and Politecnico di Torino (POLITO) in Italy.

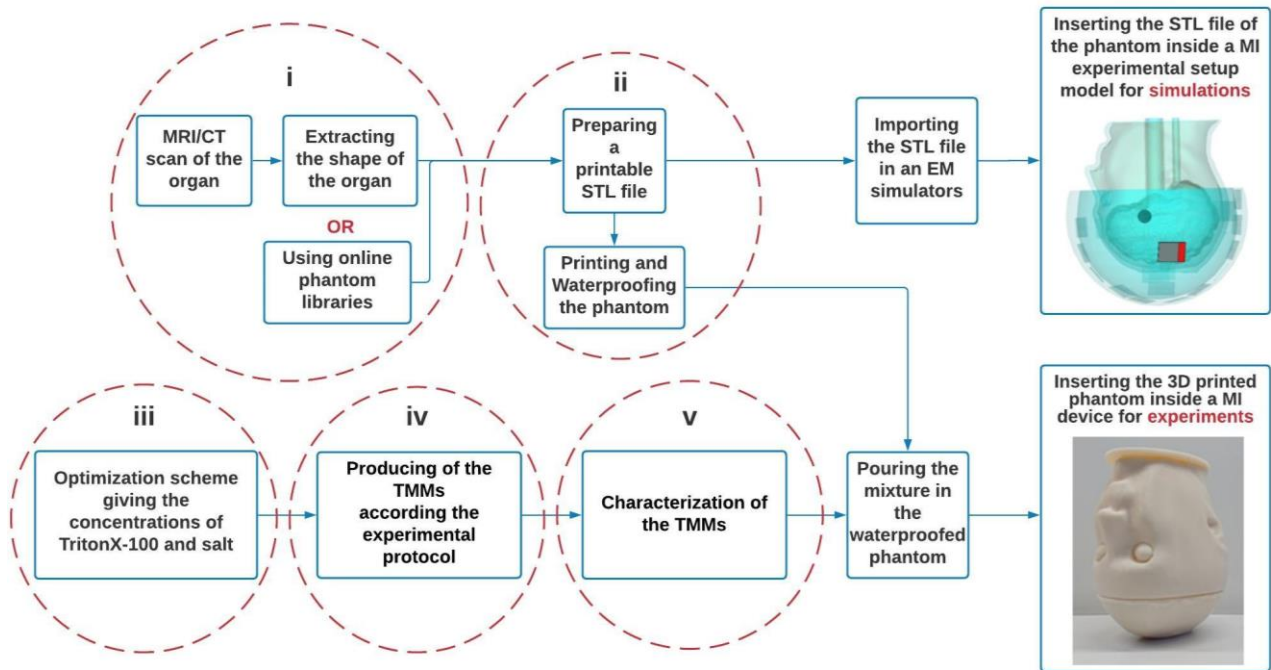


Figure 5.1: Benchmark Phantoms Flowchart for Microwave Imaging

Gaining skills to be able to prepare numerical version of a phantom for testing MWI systems was the key to accomplish the goals of this program. This happened by extracting the shape of the target tissue from MRI or CT scan of the organ and building a decent 3D model numerical file out of it. There are three main chapters covering three main goals of my PhD program, I dedicated

almost one year to get each of them done. As explained in the introduction chapter, each of these main chapters elaborates on one usage of numerical phantom files.

In a flowchart (see figure 5.1), the process of developing benchmark phantoms for the assessment of microwave devices is shown.

(i) The STL files of the organs are obtained from the segmentation of MRI/CT scan or a library phantoms.

(ii) The files are modified with a CAD software to develop printable cavities in such a way that the resulting phantom is fillable and compatible with the experimental system. Thus, the STL files should be readable by 3D printers.

(iii) TMMs are developed for each tissue according to the concentrations of TritonX-100 and salt determine from the optimization process.

(iv) The mixtures are prepared following the experimental process.

(v) Dielectrics properties of the mixture are measured. Note that at this step, an experimental adjustment may be necessary to obtain properties closer to the theoretical values or less viscous mixtures.

The numerical versions of anthropomorphic phantoms were designed and produced. Since these files are readable by 3D printers, they were printed successfully and will be filled by the produced TMMs. The 3D printed phantoms were prepared to assess the devices in the other groups. Particularly, head phantoms were developed for the MWI system in POLITO for the usage of David Rodriguez-Duarte (ESR 9) [Abedi *et al.*, 2019], Shoulder phantom was developed and designed in collaboration with Matteo Savazzi (ESR 10) from FCUL [Savazzi *et al.*, 2020] and liver phantom was designed and produced for the liver ablation study conducted by Mengchu Wang (ESR 13) from IREA-CNR [Wang *et al.*, 2022].



The STL files of the anthropomorphic phantoms were used for electromagnetic simulations, to investigate the MWI device as well as the phantom itself in the particular configurations investigated by POLITO [Abedi *et al.*, 2021] and FCUL [Joachimowicz *et al.*, 2021].

This work was enhanced by our interactions with several groups, during periods of secondment.

During my first secondment at NUIG in Galway, my knowledge of systematic measurements of biological tissues enhanced, several techniques of dielectric measurements were studied, and measurement campaigns on animals have been conducted. My collaboration with Niko Ištuk (ESR 2), led to a journal paper on the dielectric properties at different locations inside and outside of ovine heart over the 500 MHz to 20 GHz frequency range [Ištuk *et al.*, 2021].

In collaboration with WIPL-D, during 2 months of secondment in Belgrade, a simplification method was developed to reduce the problem complexity and the simulation time involved in using 3D anthropomorphic models [Singh *et al.*, 2021]. Training on WIPL-D allowed us to cross-validate with CST on the calculation of the electromagnetic field as well as to extract the contour of the phantom for use as a priori information in the TSVD algorithm.

The initial work on inversion, presented in chapter 4 is based on the training and the secondment held in CNR-IREA in Naples. During 4 months of research with the team there, I was introduced with a few inverse algorithms. This led to the use of TSVD to test the effect of introducing a priori information on the solutions of the inverse problem. STL files of the phantom gave us the opportunity to define the outer contour of the phantom and introduce it in the inverse algorithm. In this way, the algorithm reconstructs the location and shape of the high contrast target with more precision and higher quality.

As a result of this collaborative work, there are several anthropomorphic phantoms developed for applications like cerebrovascular diseases, hyperthermia, tumor and axillary lymph node

detection. As it is shown in the flowchart (figure 5.1) this work was not a stand-alone task of producing anthropomorphic phantoms but rather the sum of all blocks indicated in the flowchart i.e. segmentation, 3D design, using optimization code to obtain and etc.. There are three main goals to be achieved following this flowchart. For future work not only the structure of this flowchart can be changed by adding or removing some blocks, but also slight development of each part of the flowchart can result in more efficient, accurate and realistic results. Indeed aggregating these marginal developments makes a difference. Here are some suggestions regarding the future work:

- Extending the STL library of anthropomorphic phantoms. This can help to spend less time on segmentation part and directly starting with 3D modeling of the specific part of human body for the target MWI system.
- Finding alternative material for 3D printing. The effects of plastic as the printing material on field distribution inside the phantom have been studied and this can be improved by considering a new material, which is not too costly and has similar dielectric properties as skin.
- Böttcher law was used as the binary law to calculate the dielectric properties of different concentrations of TritonX-100 and saline water. This law was used in the optimization code as explained in chapter two. There are more binary laws in the literature, which can be checked. For instance, we found that Kraszewski law has a simpler equation for calculating the dielectric properties of the mixture, which can help the optimization code to calculate the concentrations more efficiently [Abedi *et al.*, 2021].
- There are different commercial simulators in the market and during this PhD program, WIPL-D was found as an efficient one regarding the need of the project in terms of accuracy and simulation time. Deep work on quantitative and qualitative investigation is required.

- Normally due to the high contrast between the abnormal tissue and the medium, Born approximation is not valid. This can lead to false image reconstruction. There are several inverse imaging algorithms developed in the literature, which can be studied and a priori information could be applied to them.

## **List of Publications**

### **Journal Articles**

- [J1] Savazzi, M., Abedi, S., Ištuk, N., Joachimowicz, N., Roussel, H., Porter, E., O'Halloran, M., Costa, J.R., Fernandes, C.A., Felício, J.M. and Conceição, R.C., 2020. Development of an anthropomorphic phantom of the axillary region for microwave imaging assessment. *Sensors*, 20(17), p.4968.
- [J2] Abedi, S., Joachimowicz, N., Phillips, N. and Roussel, H., 2021. A Simulation-Based Methodology of Developing 3D Printed Anthropomorphic Phantoms for Microwave Imaging Systems. *Diagnostics*, 11(2), p.376.
- [J3] Ištuk, N., Porter, E., O'loughlin, D., McDermott, B., Santorelli, A., Abedi, S., Joachimowicz, N., Roussel, H. and O'halloran, M., 2021. Dielectric Properties of Ovine Heart at Microwave Frequencies. *Diagnostics*, 11(3), p.531.

### **Conference Articles**

- [CA1] Abedi, S., Joachimowicz, N., Meyer, O., Picard, D. and Roussel, H., 2019, March. Phantoms for a novel generation of medical microwave imaging devices. In 2019 13th European Conference on Antennas and Propagation (EuCAP) (pp. 1-4). IEEE.
- [CA2] Abedi, S., Joachimowicz, N., Duchêne, B., Roussel, H., Tobon, J., Rodriguez-Duarte, D., Scapaticci, R., Vipiana, F. and Crocco, L., 2019, December. Benchmark Head phantoms for microwave imaging of brain strokes. In Conference PIERS 2019.
- [CA3] Ištuk, N., McDermott, B., Porter, E., Santorelli, A., Abedi, S., O'Halloran, M., Joachimowicz, N. and Roussel, H., 2020, March. Detailed Dielectric Characterisation of the Heart and Great Vessels. In 2020 14th European Conference on Antennas and Propagation (EuCAP) (pp. 1-5). IEEE.

- [CA4] Singh, T., Abedi, S., Ninkovic, B., Stevanovic, M., Joachimowicz, N., Roussel, H. and Kolundzija, B., 2021, March. Smart Simplification of Anthropomorphic Head Phantom Aimed for Microwave Imaging. In 2021 15th European Conference on Antennas and Propagation (EuCAP) (pp. 1-4). IEEE.
- [CA5] Joachimowicz, N., Abedi, S., Roussel, H., 2021. Numerical Wideband Anthropomorphic Phantom for Biomedical Microwave Imaging. CAMA 2021.
- [CA6] Wang, M., Cavagnaro, M., Abedi, S., Joachimowicz, N., Roussel, H., Costanzo, S., and Crocco, S., “Initial Experimental Validation of a Microwave Imaging System to Monitor Liver Microwave Thermal Ablation”, In 2022 16th European Conference on Antennas and Propagation (EuCAP).

## REFERENCES:

- 3D slicer, image-computing platform. [Online]. Available: <https://www.slicer.org/>
- Abedi, S., Joachimowicz, N., Duchêne, B., Roussel, H., Tobon, J., Rodriguez-Duarte, D., Scapaticci, R., Vipiana, F. and Crocco, L., 2019, December. Benchmark Head phantoms for microwave imaging of brain strokes. In Conference PIERS 2019.
- Abedi, S., Joachimowicz, N., Meyer, O., Picard, D. and Roussel, H., 2019, March. Phantoms for a novel generation of medical microwave imaging devices. In 2019 13th European Conference on Antennas and Propagation (EuCAP) (pp. 1-4). IEEE.
- Abedi, S., Joachimowicz, N., Phillips, N. and Roussel, H., 2021. A Simulation-Based Methodology of Developing 3D Printed Anthropomorphic Phantoms for Microwave Imaging Systems. *Diagnostics*, 11(2), p.376.
- Asfia, A., Novak, J.I., Mohammed, M.I., Rolfe, B. and Kron, T., 2020. A review of 3D printed patient specific immobilisation devices in radiotherapy. *Physics and imaging in radiation oncology*, 13, pp.30-35.
- Bertero, M., Boccacci, P. and De Mol, C., 2021. Introduction to inverse problems in imaging. CRC press.
- Bosch, F.X., Ribes, J. and Borràs, J., 1999. Epidemiology of primary liver cancer. In *Seminars in liver disease* (Vol. 19, No. 03, pp. 271-285). © 1999 by Thieme Medical Publishers, Inc..
- Böttcher, C.J.F. and Bordewijk, P., 1978. Theory of electric polarization (Vol. 2). Elsevier Science Limited.
- Brain anatomy. [Online]. Available: <https://www.princetonbrainandspine.com/resources/learning-center/brain-anatomy/>
- Bray, F., Ferlay, J., Soerjomataram, I., Siegel, R.L., Torre, L.A. and Jemal, A., 2018. Global cancer statistics 2018: GLOBOCAN estimates of incidence and mortality worldwide for 36 cancers in 185 countries. *CA: a cancer journal for clinicians*, 68(6), pp.394-424.
- Burfeindt, M.J., Colgan, T.J., Mays, R.O., Shea, J.D., Behdad, N., Van Veen, B.D. and Hagness, S.C., 2012. MRI-derived 3-D-printed breast phantom for microwave breast imaging validation. *IEEE antennas and wireless propagation letters*, 11, pp.1610-1613.
- Candefjord, S., Wings, J., Malik, A.A., Yu, Y., Rylander, T., McKelvey, T., Fhager, A., Elam, M. and Persson, M., 2017. Microwave technology for detecting traumatic intracranial bleedings: tests on phantom of subdural hematoma and numerical simulations. *Medical & biological engineering & computing*, 55(8), pp.1177-1188.
- Casu, M.R., Vacca, M., Tobon, J.A., Pulimeno, A., Sarwar, I., Solimene, R. and Vipiana, F., 2017. A COTS-based microwave imaging system for breast-cancer detection. *IEEE transactions on biomedical circuits and systems*, 11(4), pp.804-814.

- Chua, C.K., Leong, K.F. and Lim, C.S., 2010. Rapid prototyping: principles and applications (with companion CD-ROM). World Scientific Publishing Company.
- Cole, K.S. and Cole, R.H., 1941. Dispersion and absorption in dielectrics I. Alternating current characteristics. *The Journal of chemical physics*, 9(4), pp.341-351.
- CT scan vs MRI. [Online]. Available: <https://www.regencymedicalcentre.com/blog/ct-scan-vs-mri/>
- de Hoop, A.T., 1995. ``Handbook of Radiation and Scattering of Waves: Acoustic Waves in Fluids. Elastic Waves in Solids, Electromagnetic Waves."Academic Press, San Diego.
- Faenger, B., Ley, S., Helbig, M., Sachs, J. and Hilger, I., 2017, March. Breast phantom with a conductive skin layer and conductive 3D-printed anatomical structures for microwave imaging. In 2017 11th European Conference on Antennas and Propagation (EUCAP) (pp. 1065-1068). IEEE.
- Felício, J.M., Bioucas-Dias, J.M., Costa, J.R. and Fernandes, C.A., 2019. Microwave breast imaging using a dry setup. *IEEE Transactions on Computational Imaging*, 6, pp.167-180.
- Foster, K.R. and Schwan, H.P., 1986. Dielectric properties of tissues. *CRC handbook of biological effects of electromagnetic fields*, pp.27-96.
- Fundação Champalimaud (Lisbon, Portugal). Available online: <https://fchampalimaud.org/> (accessed on 2 September 2020).
- Gabriel, S., Lau, R.W. and Gabriel, C., 1996. The dielectric properties of biological tissues: III. Parametric models for the dielectric spectrum of tissues. *Physics in medicine & biology*, 41(11), p.2271.
- Garrett, J. and Fear, E., 2015. A new breast phantom with a durable skin layer for microwave breast imaging. *IEEE Transactions on Antennas and Propagation*, 63(4), pp.1693-1700.
- Godinho, D.M., Felicio, J., Fernandes, C.A. and Conceicao, R.C., 2021. Experimental evaluation of an axillary microwave imaging system to aid breast cancer staging. *IEEE Journal of Electromagnetics, RF and Microwaves in Medicine and Biology*.
- Gong, Z., Chen, Y., Lin, X., Wu, K. and Cree, M.J., 2021. Generic Wide-band Phantom Design Methodology for Microwave Medical Applications. *IEEE Antennas and Wireless Propagation Letters*.
- Grimm, T., 2004. User's guide to rapid prototyping. Society of Manufacturing Engineers.
- Haleem, A., Javaid, M. and Vaishya, R., 2020. 3D printing applications for the treatment of cancer. *Clinical Epidemiology and Global Health*, 8(4), pp.1072-1076.
- Hartsgrove, G., Kraszewski, A. and Surowiec, A., 1987. Simulated biological materials for electromagnetic radiation absorption studies. *Bioelectromagnetics: Journal of the Bioelectromagnetics Society, The Society for Physical Regulation in Biology and Medicine, The European Bioelectromagnetics Association*, 8(1), pp.29-36.

- Hasted, J.B., 1973. Aqueous dielectrics (Vol. 122). London: Chapman and Hall.
- Henriksson, T., Joachimowicz, N., Conessa, C. and Bolomey, J.C., 2010. Quantitative microwave imaging for breast cancer detection using a planar 2.45 GHz system. *IEEE Transactions on Instrumentation and Measurement*, 59(10), pp.2691-2699.
- IFAC, Calculation of the Dielectric Properties of Body Tissues in the frequency range 10 Hz - 100 GHz. [Online]. Available: <http://niremf.ifac.cnr.it/tissprop/htmlclie/htmlclie.php>
- Ištuk, N., Porter, E., O'loughlin, D., McDermott, B., Santorelli, A., Abedi, S., Joachimowicz, N., Roussel, H. and O'halloran, M., 2021. Dielectric Properties of Ovine Heart at Microwave Frequencies. *Diagnostics*, 11(3), p.531.
- Joachimowicz, N., Pichot, C. and Hugonin, J.P., 1991. Inverse scattering: An iterative numerical method for electromagnetic imaging. *IEEE Transactions on Antennas and Propagation*, 39(12), pp.1742-1753.
- Joachimowicz, N., Duchêne, B., Conessa, C. and Meyer, O., 2018. Anthropomorphic breast and head phantoms for microwave imaging. *Diagnostics*, 8(4), p.85.
- Joachimowicz, N., Abedi, S., Roussel, H., 2021. Numerical Wideband Anthropomorphic Phantom for Biomedical Microwave Imaging. *CAMA 2021*.
- Joisel, A., Mallorqui, J., Broquetas, A., Geffrin, J.M., Joachimowicz, N., Lossera, M.V., Joire, L. and Bolomey, J.C., 1999, May. Microwave imaging techniques for biomedical applications. In *IMTC/99. Proceedings of the 16th IEEE Instrumentation and Measurement Technology Conference (Cat. No. 99CH36309) (Vol. 3, pp. 1591-1596)*. IEEE.
- Karadima, O., Rahman, M., Sotiriou, I., Ghavami, N., Lu, P., Ahsan, S. and Kosmas, P., 2020. Experimental validation of microwave tomography with the DBIM-TwIST algorithm for brain stroke detection and classification. *Sensors*, 20(3), p.840.
- Khuda, I.E., 2017. A comprehensive review on design and development of human breast phantoms for ultra-wide band breast cancer imaging systems. *Engineering Journal*, 21(3), pp.183-206.
- Kidwell, C.S. and Hsia, A.W., 2006. Imaging of the brain and cerebral vasculature in patients with suspected stroke: advantages and disadvantages of CT and MRI. *Current neurology and neuroscience reports*, 6(1), pp.9-16.
- Kobayashi, T., Nojima, T., Yamada, K. and Uebayashi, S., 1993. Dry phantom composed of ceramics and its application to SAR estimation. *IEEE transactions on Microwave Theory and Techniques*, 41(1), pp.136-140.
- Koutsoupidou, M., Karanasiou, I.S., Kakoyiannis, C.G., Groumpas, E., Conessa, C., Joachimowicz, N. and Duchêne, B., 2017. Evaluation of a tumor detection microwave system with a realistic breast phantom. *Microwave and Optical Technology Letters*, 59(1), pp.6-10.
- Kraszewski, A. ed., 1996. Microwave aquametry: electromagnetic wave interaction with water-containing materials. IEEE.



- Kraszewski, A., 1977. Prediction of the dielectric properties of two-phase mixtures. *Journal of Microwave Power*, 12(3), pp.216-222.
- Larsen, L.E. and Jacobi, J.H., 1979. Microwave scattering parameter imagery of an isolated canine kidney. *Medical physics*, 6(5), pp.394-403.
- Lazebnik, M., Okoniewski, M., Booske, J.H. and Hagness, S.C., 2007. Highly accurate Debye models for normal and malignant breast tissue dielectric properties at microwave frequencies. *IEEE microwave and wireless components letters*, 17(12), pp.822-824.
- Li, X. and Hagness, S.C., 2001. A confocal microwave imaging algorithm for breast cancer detection. *IEEE Microwave and wireless components letters*, 11(3), pp.130-132.
- Lichtenecker, K.V., 1931. Die Herleitung des logarithmischen Mischungsgesetzes aus allgemeinen Prinzipien der stationären Stromung. *phys. Z*, 32, pp.255-260.
- Ljungqvist, J., Candefjord, S., Persson, M., Jönsson, L., Skoglund, T. and Elam, M., 2017. Clinical evaluation of a microwave-based device for detection of traumatic intracranial hemorrhage. *Journal of neurotrauma*, 34(13), pp.2176-2182.
- Looyenga, H., 1965. Dielectric constants of heterogeneous mixtures. *Physica*, 31(3), pp.401-406.
- Lopresto, V., Pinto, R., Lovisolo, G.A. and Cavagnaro, M., 2012. Changes in the dielectric properties of ex vivo bovine liver during microwave thermal ablation at 2.45 GHz. *Physics in Medicine & Biology*, 57(8), p.2309.
- Lopresto, V., Strigari, L., Farina, L., Minosse, S., Pinto, R., D'Alessio, D., Cassano, B. and Cavagnaro, M., 2018. CT-based investigation of the contraction of ex vivo tissue undergoing microwave thermal ablation. *Physics in Medicine & Biology*, 63(5), p.055019.
- Maundy, B. and Elwakil, A.S., 2012. Extracting single dispersion Cole–Cole impedance model parameters using an integrator setup. *Analog Integrated Circuits and Signal Processing*, 71(1), pp.107-110.
- Mazloumi, M., Van Gompel, G., Kersemans, V., de Mey, J. and Buls, N., 2021. The presence of contrast agent increases organ radiation dose in contrast-enhanced CT. *European Radiology*, pp.1-10.
- McDermott, B., Porter, E., Santorelli, A., Divilly, B., Morris, L., Jones, M., McGinley, B. and O'Halloran, M., 2017. Anatomically and dielectrically realistic microwave head phantom with circulation and reconfigurable lesions. *Progress In Electromagnetics Research B*, 78, pp.47-60.
- Meaney, P.M., Fanning, M.W., Li, D., Poplack, S.P. and Paulsen, K.D., 2000. A clinical prototype for active microwave imaging of the breast. *IEEE Transactions on Microwave Theory and Techniques*, 48(11), pp.1841-1853.
- Meaney, P.M., Fanning, M.W., Raynolds, T., Fox, C.J., Fang, Q., Kogel, C.A., Poplack, S.P. and Paulsen, K.D., 2007. Initial clinical experience with microwave breast imaging in women with normal mammography. *Academic radiology*, 14(2), pp.207-218.

- Meaney, P.M., Rydholm, T., Fhager, A., Persson, M., Joachimowicz, N., Conessa, C. and Duchêne, B., 2016, October. Conformal mesh and two-step tomographic imaging of the Supelec breast phantom. In 2016 IEEE Conference on Antenna Measurements & Applications (CAMA) (pp. 1-3). IEEE.
- Meaney, P.M., Fox, C.J., Geimer, S.D. and Paulsen, K.D., 2017. Electrical characterization of glycerin: Water mixtures: Implications for use as a coupling medium in microwave tomography. *IEEE transactions on microwave theory and techniques*, 65(5), pp.1471-1478.
- Mikhnev, V. and Vainikainen, P., 2002, September. Microwave imaging of layered structures in civil engineering. In 2002 32nd European Microwave Conference (pp. 1-4). IEEE.
- Mobashsher, A.T., Abbosh, A.M. and Wang, Y., 2014. Microwave system to detect traumatic brain injuries using compact unidirectional antenna and wideband transceiver with verification on realistic head phantom. *IEEE Transactions on Microwave Theory and Techniques*, 62(9), pp.1826-1836.
- Mobashsher, A.T. and Abbosh, A.M., 2015. Artificial human phantoms: Human proxy in testing microwave apparatuses that have electromagnetic interaction with the human body. *IEEE Microwave Magazine*, 16(6), pp.42-62.
- Mohammed, B.J., Abbosh, A.M., Mustafa, S. and Ireland, D., 2013. Microwave system for head imaging. *IEEE Transactions on Instrumentation and Measurement*, 63(1), pp.117-123.
- Mossotti, O.F., 1846. *Discussione analitica sull'influenza che l'azione di un mezzo dielettrico ha sulla distribuzione dell'elettricità alla superficie di più corpi elettrici disseminati in esso* (Vol. 22). Dai tipi della r. D. camera.
- Noghanian, S., Sabouni, A., Desell, T. and Ashtari, A., 2014. *Microwave Tomography*. New York, NY, USA:: Springer.
- Onsager, L., 1936. Electric moments of molecules in liquids. *Journal of the American Chemical Society*, 58(8), pp.1486-1493.
- Pamboukian, S., 2001. "Looking Radiant": Science, Photography and the X-ray Craze of 1896. *Victorian Review*, pp.56-74.
- Pastorino, M., 2010. *Microwave imaging* (Vol. 208). John Wiley & Sons.
- Persson, M., Fhager, A., Trefná, H.D., Yu, Y., McKelvey, T., Pegenius, G., Karlsson, J.E. and Elam, M., 2014. Microwave-based stroke diagnosis making global prehospital thrombolytic treatment possible. *IEEE Transactions on Biomedical Engineering*, 61(11), pp.2806-2817.
- Plasticboy, Blender Rigged V07 Anatomy 3D models store. [Online]. Available: <https://www.plasticboy.co.uk/store/index.html>
- Pokorny, T. and Tesarik, J., 2019, June. 3D Printed Multi-layer Molds of Human Head Tissue Phantoms for Microwave Stroke Detection. In 2019 Photonics & Electromagnetics Research Symposium-Spring (PIERS-Spring) (pp. 1424-1427). IEEE.

- Rayleigh, L., 1892. LVI. On the influence of obstacles arranged in rectangular order upon the properties of a medium. The London, Edinburgh, and Dublin Philosophical Magazine and Journal of Science, 34(211), pp.481-502.
- Rigden, J.S., 1999. Isidor Isaac Rabi: walking the path of God. Physics world, 12(11), p.27.
- Rodrigues, D.B., Maccarini, P.F., Salahi, S., Oliveira, T.R., Pereira, P.J., Limão-Vieira, P., Snow, B.W., Reudink, D. and Stauffer, P.R., 2014. Design and optimization of an ultra wideband and compact microwave antenna for radiometric monitoring of brain temperature. IEEE transactions on biomedical engineering, 61(7), pp.2154-2160.
- Rodriguez-Duarte, D.O., Vasquez, J.A.T., Scapaticci, R., Crocco, L. and Vipiana, F., 2020. Brick-Shaped Antenna Module for Microwave Brain Imaging Systems. IEEE Antennas and Wireless Propagation Letters, 19(12), pp.2057-2061.
- Rodriguez-Duarte, D.O., Tobon Vasquez, J.A., Scapaticci, R., Turvani, G., Cavagnaro, M., Casu, M.R., Crocco, L. and Vipiana, F., 2021. Experimental Validation of a Microwave System for Brain Stroke 3-D Imaging. Diagnostics, 11(7), p.1232.
- Roscoe, L., 1988. Stereolithography interface specification. America-3D Systems Inc, 27(2020), p.10.
- Rydholm, T., Fhager, A., Persson, M., Geimer, S.D. and Meaney, P.M., 2018. Effects of the plastic of the realistic GeePS-L2S-Breast phantom. Diagnostics, 8(3), p.61.
- Said, T. and Varadan, V.V., 2009, June. Variation of Cole-Cole model parameters with the complex permittivity of biological tissues. In 2009 IEEE MTT-S International Microwave Symposium Digest (pp. 1445-1448). IEEE.
- Savazzi, M., Abedi, S., Ištuk, N., Joachimowicz, N., Roussel, H., Porter, E., O'Halloran, M., Costa, J.R., Fernandes, C.A., Felício, J.M. and Conceição, R.C., 2020. Development of an anthropomorphic phantom of the axillary region for microwave imaging assessment. Sensors, 20(17), p.4968.
- Semenov, S.Y., Svenson, R.H., Boulyshev, A.E., Souvorov, A.E., Borisov, V.Y., Sizov, Y., Starostin, A.N., Dezern, K.R., Tatsis, G.P. and Baranov, V.Y., 1996. Microwave tomography: Two-dimensional system for biological imaging. IEEE Transactions on Biomedical Engineering, 43(9), pp.869-877.
- Semenov, S.Y. and Corfield, D.R., 2008. Microwave tomography for brain imaging: Feasibility assessment for stroke detection. International Journal of Antennas and Propagation, 2008.
- Scapaticci, R., Catapano, I. and Crocco, L., 2012. Wavelet-based adaptive multiresolution inversion for quantitative microwave imaging of breast tissues. IEEE transactions on antennas and propagation, 60(8), pp.3717-3726.
- Scapaticci, R., Di Donato, L., Catapano, I. and Crocco, L., 2012. A feasibility study on microwave imaging for brain stroke monitoring. Progress In Electromagnetics Research B, 40, pp.305-324.

- Scapaticci, R., Bellizzi, G.G., Cavagnaro, M., Lopresto, V. and Crocco, L., 2017. Exploiting microwave imaging methods for real-time monitoring of thermal ablation. *International Journal of Antennas and Propagation*, 2017.
- Scapaticci, R., Lopresto, V., Pinto, R., Cavagnaro, M. and Crocco, L., 2018. Monitoring thermal ablation via microwave tomography: An ex vivo experimental assessment. *Diagnostics*, 8(4), p.81.
- Scapaticci, R., Tobon, J., Bellizzi, G., Vipiana, F. and Crocco, L., 2018. Design and numerical characterization of a low-complexity microwave device for brain stroke monitoring. *IEEE Transactions on Antennas and Propagation*, 66(12), pp.7328-7338.
- Shea, J.D., Kosmas, P., Hagness, S.C. and Van Veen, B.D., 2010. Three-dimensional microwave imaging of realistic numerical breast phantoms via a multiple-frequency inverse scattering technique. *Medical physics*, 37(8), pp.4210-4226.
- Singh, T., Abedi, S., Ninkovic, B., Stevanovic, M., Joachimowicz, N., Roussel, H. and Kolundzija, B., 2021, March. Smart Simplification of Anthropomorphic Head Phantom Aimed for Microwave Imaging. In *2021 15th European Conference on Antennas and Propagation (EuCAP)* (pp. 1-4). IEEE.
- Smith, K.E., Bourqui, J., Garrett, D., Zarnke, S., Owjimehr, M., Deutscher, D., Fung, T.S. and Fear, E., 2021. Microwave Imaging of the Breast: Consistency of Measurements over Time. *IEEE Journal of Electromagnetics, RF and Microwaves in Medicine and Biology*.
- Stogryn, A., 1971. Equations for calculating the dielectric constant of saline water (correspondence). *IEEE transactions on microwave theory and Techniques*, 19(8), pp.733-736.
- Tabakov, S.D., 2021. Professor John Mallard, 1927–2021.
- Tabbara, W., Duchêne, B., Pichot, C., Lesselier, D., Chommeloux, L. and Joachimowicz, N., 1988. Diffraction tomography: contribution to the analysis of some applications in microwaves and ultrasonics. *Inverse Problems*, 4(2), p.305.
- Tan, S.Y. and Poole, P.S., 2020. Allan MacLeod Cormack (1924–1998): Discoverer of computerised axial tomography. *Singapore medical journal*, 61(1), p.4.
- Thakur, O.P. and Singh, A.K., 2008. Analysis of Dielectric Relaxation in Water at Microwave Frequency. *Adv. Studies Theor. Phys*, 2(13), pp.637-644.
- Tobon Vasquez, J.A., Scapaticci, R., Turvani, G., Bellizzi, G., Joachimowicz, N., Duchêne, B., Tedeschi, E., Casu, M.R., Crocco, L. and Vipiana, F., 2019. Design and experimental assessment of a 2D microwave imaging system for brain stroke monitoring. *International Journal of Antennas and Propagation*, 2019.
- Tobon Vasquez, J.A., Scapaticci, R., Turvani, G., Bellizzi, G., Rodriguez-Duarte, D.O., Joachimowicz, N., Duchêne, B., Tedeschi, E., Casu, M.R., Crocco, L. and Vipiana, F., 2020. A prototype microwave system for 3D brain stroke imaging. *Sensors*, 20(9), p.2607.

- Vasquez, J.A.T., Scapaticci, R., Turvani, G., Ricci, M., Farina, L., Litman, A., Casu, M.R., Crocco, L. and Vipiana, F., 2020. Noninvasive inline food inspection via microwave imaging technology: An application example in the food industry. *IEEE Antennas and Propagation Magazine*, 62(5), pp.18-32.
- Walter, É., 2014. Numerical methods and optimization. Cham: Springer.
- Wang, K., Ho, C.C., Zhang, C. and Wang, B., 2017. A review on the 3D printing of functional structures for medical phantoms and regenerated tissue and organ applications. *Engineering*, 3(5), pp.653-662.
- Wang, J., Lim, E.G., Leach, M.P., Wang, Z. and Man, K.L., 2020. Open-Ended Coaxial Cable Selection for Measurement of Liquid Dielectric Properties via the Reflection Method. *Mathematical Problems in Engineering*, 2020.
- Wang, M., Scapaticci, R., Cavagnaro, M. and Crocco, L., 2021. Towards a Microwave Imaging System for Continuous Monitoring of Liver Tumor Ablation: Design and In Silico Validation of an Experimental Setup. *Diagnostics*, 11(5), p.866.
- Wang, M., Cavagnaro, M., Abedi, S., Joachimowicz, N., Roussel, H., Costanzo, S., and Crocco, S., “Initial Experimental Validation of a Microwave Imaging System to Monitor Liver Microwave Thermal Ablation”, *EUCAP 2022* (submitted).
- Weiland, T., 1977. A discretization method for the solution of Maxwell's equations for six component fields: *Electronics and Communications AEÜ*.
- Wiener, O., 1912. Die Theorie des Mischkorpers für das Feld der stationären Stromung. *Abhandlungen der Sächsischen Gesellschaft der Akademischen Wissenschaften in Mathematik und Physik*, 32, pp.507-604.
- WIPL-D. [Online]. Available: <https://wipl-d.com/>
- World health report, the world health report 2002 - reducing risks, promoting healthy life. [Online]. Available: <http://www.who.int/whr/2002/en/>
- Zidane, F., Lanteri, J., Marot, J., Brochier, L., Joachimowicz, N., Roussel, H. and Migliaccio, C., 2020. Nondestructive control of fruit quality via millimeter waves and classification techniques: Investigations in the automated health monitoring of fruits. *IEEE Antennas and Propagation Magazine*, 62(5), pp.43-54.